



**Master thesis**

---

**Inner flow structures of turbidity currents  
based on applied ultrasonic techniques**

---

**Jumpei HITOMI**

**Laboratory for Flow Control,  
Division of Energy and Environmental Systems,  
Graduate School of Engineering,  
Hokkaido University.**

**1<sup>st</sup> February 2019**



## Abstract

The flow behavior of experimental turbidity currents is evaluated quantitatively in order to reveal their long-distance propagation mechanism. Turbidity currents occurring in nature have complicated and large-scale of flow structures, so it is difficult to obtain sufficient knowledge about their flow behaviors from currents with a limited occurrence observed by a field research. Our research group, therefore, thinks that it is important to obtain basic knowledge that can be extended to actual phenomena from experimental turbidity currents. The test section is an inclined rectangle flume with 4,548 mm in length, 210 mm in height and 143 mm in width. The gate, which separates a heavier fluid and an ambient fluid, is positioned at roughly half length of the flume. It is revealed that the gravity currents generated by the lock-exchange method in such a high-volume release propagate with almost constant values of front velocity  $U_f$ . As the heavier fluids, three kinds of fluids are examined; quartz-suspended fluid, opalin-suspended fluid, and saline-dissolved fluids. The center diameters  $d_{50}$  of quartz particles and opalin particles are 12.2 and 18.9  $\mu\text{m}$ , respectively. Such small particles have been not used for UVP measurement basically, because the intensity of reflected waves from the particle is too small to be detected by an ultrasonic transducer. In this study, however, a supplemental experiment reveals that the volume fraction ( $\alpha$ ) range of quartz particles  $0.1 \leq \alpha \leq 5\%$  shows reasonable velocity distributions obtained by UVP with 4 MHz transducer. Total twenty-five cases of experiments are carried out changing the kind and initial density of the heavier fluids  $\rho_H$ . In the seven cases of them, two-layer turbidity currents are generated, and the experimental results are discussed. The details about the experimental facility, sediment materials, and initial conditions are summarized in chapter 2.

In chapter 3, analysis method is mentioned. To evaluate the flow behaviors of the gravity currents quantitatively, it is essential to extend the use range of ultrasonic velocity profiler (UVP), which can be applied to opaque flows. In this study, the measurement by a pair of UVPs makes it possible to obtain horizontal and vertical velocity components ( $u$  and  $v$ ) along the whole measurement line of the ultrasonic beam using time correction method based on  $U_f$ . Additionally, the particle concentration is estimated by the calculation using the spatio-temporal echo distribution. In case of Rayleigh scattering, the echo values vary with the particle concentration existing in a unit volume. In this study, the boundary condition at the bottom is set to solve the non-linear integral equation between the echo amplitude and the particle concentration. Besides, the scattering intensity is varying depending on the diameter of particles. Applying this characteristic to echo intensity distributions, it makes possible to detect interfaces in the cases of two-layer turbidity currents.

In chapter 4.1., the flow structures between the quartz-suspended currents and the saline density currents are compared. The initial density of all heavier fluids mentioned in this chapter is  $\rho_H = 1008 \text{ kg/m}^3$ . Applying pattern matching method to sequential experimental images, it is revealed that the  $U_f$  values of the turbidity currents are greater on average 19.0% than the density currents. The

wall shear stress  $\tau_w$  is calculated by the least square fitting method for the time-averaged  $u$  distributions. The  $\tau_w$  of the turbidity current is larger than the density current. Therefore, it is revealed that the turbidity current propagates with larger values of  $U_f$  than the density current, although the turbidity currents have larger friction coefficient  $C_f$  about wall shear stress on the bed. In the body region of the two types of currents, the maximum velocity of horizontal component ( $u_{\max}$ ) is also larger in the turbidity current than the density current. On the other hand, both values of the height  $h_m$  that takes the maximum velocity  $u_{\max}$  and the thickness of the flows are smaller in case of the turbidity current. From these results, the existence of the suspended particles with heavier density than water suppresses the influence of the diffusion, which is predominant factor in the density currents, and helps the continuous supply of driving force due to the density difference.

In chapter 4.2., the turbulent flow structures of the quartz-suspended turbidity current as solid-liquid two-phase flow is discussed. The momentum conservation equation based on two-fluid model is applied to the distributions of the body region. The computed results indicate that the viscous stress and Reynolds shear stress among the five shear stress components are dominant like single-phase channel flows, but the distribution in the height direction of the shear stresses shows a different shape from that. The values of the viscous stress and Reynolds shear stress get canceled out in the outer region ( $h_m < y < h_t$ , where the  $u$  reaches zero), so it is revealed that the pressure gradient is working just in the inner region ( $0 < y < h_m$ ) of the current. Such a phenomenon shows a negative momentum transfer against the mean velocity gradient, which is working to keep a stable stratification.

In chapter 4.3., the flow behaviors of several kinds of currents are discussed. These experimental cases show that the turbidity currents containing quartz particles propagates 38.5% faster than turbidity currents containing opalin particles. The analysis results about two-layer turbidity currents show that the kind of the particles suspended in the lower layer determines the front velocity  $U_f$ , when the bulk density  $\rho_H$  in initial condition is equal. In the two-layer turbidity currents composed of different kinds of particle-suspended fluid, it is confirmed that the lower layer is rolled up in the head region and the upper layer is covered with the fluid forming the lower layer. According to such a flow structure of the lower layer, not only the friction with the bed but also the interaction with the ambient fluid in the vicinity of the head region are dominated by the kind of lower layer, which means that the value of  $U_f$  can be almost estimated by the friction at the bottom and the interaction at the head region regardless the influence of the shear flow at the upper boundary. In addition to the comparison about  $U_f$ , the friction velocity  $u^*$  is estimated from the distribution of the horizontal velocity component  $u$  in the body region. The relationship between the friction velocity  $u^*$  and the maximum velocity  $u_{\max}$  in the body region is confirmed as  $u^*/u_{\max} \approx 0.114$  in every experimental case. It is also confirmed that the friction coefficient  $C_f = 2(u^*/u_{\max})^2 \approx 0.0260$  is obtained using the relationship.



## Table of contents

1. Introduction.....	6
1.1. Turbidity currents.....	6
1.2. Ultrasonic measurement techniques and multi-phase flows .....	9
1.3. Final goal and objective of this study .....	12
1.4. Nomenclature.....	14
2. Experimental method.....	15
2.1. Experimental facility.....	15
2.2. Sediment particles.....	17
2.3. Experimental cases.....	19
3. Development of analysis method.....	21
3.1. Velocity measurement.....	21
3.1.1. Supplemental experiments by stirring flow .....	21
3.1.2. Velocity measurements for gravity currents.....	25
3.2. Concentration profiles.....	27
3.3. Pattern matching method and front velocity .....	31
4. Results and discussions.....	39
4.1. Comparison of flow structures between quartz-suspended currents and saline density currents .....	39
4.1.1. Inner velocity structures of the currents.....	39
4.1.2. Time variation of the height and velocity of the currents .....	40
4.1.3. Flow structures in the body region.....	42
4.1.4. Comparison of fluctuation components in the body region .....	45
4.1.5. Summary of the difference of flow structures between the turbidity currents and the density currents .....	46
4.2. Inner flow structures of turbidity currents as solid–liquid two–phase flow.....	49
4.2.1. Flow field of the current.....	50
4.2.2. Concentration profile .....	52
4.2.3. Momentum equation in the body region.....	55
4.3. Comparison of flow structures between quartz-suspended currents, and opalin-suspended currents, and two–layer turbidity currents .....	63
4.3.1. Experimental snapshots of the currents.....	64
4.3.2. Inner flow structures .....	67
4.3.3. Interfaces in two–layer turbidity currents .....	76
4.3.4. Summary of flow behaviors in the some kinds of turbidity currents .....	84



5. Conclusion .....	86
6. Bibliography .....	89

Acknowledgements

Appendix

# 1. Introduction

## 1.1. Turbidity currents

Gravity currents can be observed in many places, for instance in the seas, rivers, and so on. Turbidity currents, a kind of gravity currents driven by density difference between particle-suspended fluid and ambient fluid, are strongly related to the transportation or the deposition of fine particles. Consequently, they play important roles not only for a general understanding of global sediment transport process, but also for estimating the potential environmental hazards which they cause (reservoir sedimentation, trigger of *Tsunami*, cutting of submarine pipeline systems and cables, effluent dispersal and volcanic hazard (Middleton,1993)). Chamoun *et al.* (2016) suggested the problem about reservoir sedimentation and a solution for the efficient discharge by the venting. In order to settle the reservoir sedimentation problem, Oehy *et al.* (2010) evaluated the effect of inclined jet screen on turbidity currents. The result of their study indicates that in certain configurations turbidity currents can be partially stopped by the jet screen and the deposits downstream of the screen may be reduced up to a factor of two as compared with deposits of a free-flowing turbidity current. In addition, there is also the theory that the specific deposition formed by turbidity currents is related to the production or the melting process of fossil fuels such as methane hydrate. The reason why turbidity currents have been payed attention as an important subject is not limited in the field of civil engineering, and the interest for the long-distance propagation mechanism is attracting much attention with a view toward multi-phase fluid dynamics or Earth science.

Actually, turbidity currents have been reported to propagate several thousand or hundred kilometers in the seas or rivers by field researches. For example, Azpiroz-Zabala *et al.* (2017) reported the measurement results by acoustic Doppler current profiler (ADCP) of actual turbidity currents occurring in Congo Canyon (see Table 1-1). In that research, turbidity currents are reported to have occurred six times in the period of seven months, and their thicknesses are from 48 to 77 m and the duration time of the currents is from 5.2 to 10.1 days. Additionally, Symons *et al.* (2017) also reported the field measurement results in Monterey Bay obtained by ADCP. In the study, the evolution of flow structure and composition are discussed as shown in Fig. 1-1.

Contrary to such field researches, many laboratory experiments and numerical simulations have been conducted to collect detailed knowledge of the velocity and turbulent flow structures in the turbidity currents. Parker *et al.* (1986) suggested the self-acceleration mechanism of turbidity currents from numerical simulation. In the study, it is reported that the sediment entrainment from the bed resupplies potential energy, and it makes possible the acceleration and the long-distance propagation of turbidity currents. Cesare *et al.* (2001) established a novel numerical model for computational fluid dynamics of the turbidity current, which takes into account the interaction between the current and the deposited sediment. That three-dimensional (3D) numerical model can simulate the balance between deposition and erosion, and the currents provides good agreement with the turbidity currents in a

laboratory flume as well as field measurements at the Luzzone Reservoir in swiss Alps. In the study by Gladstone *et al.* (2004), the multi-layer saline density currents were examined in the lock-exchange flume. It was revealed that the flow behaviors of those currents depend on a dimensionless density ratio between the layers  $\rho^*$  and dimensionless difference in the driving buoyancy  $B^*$  (see Fig. 1-2);

$$\rho^* = \frac{\rho_U - \rho_W}{\rho_L - \rho_W} = \frac{g'_U}{g'_L}, \quad (1-1)$$

and

$$B^* = \frac{B_U}{B_U + B_W} = \frac{h_U g'_U}{(h_U g'_U + h_L g'_L)} \equiv \frac{M_U}{M_U + M_L}, \quad (1-2)$$

where  $\rho_U$ ,  $\rho_L$ , and  $\rho_W$  denote the density of the upper layer, lower layer, and water, respectively. In the study by Longo *et al.* (2016), the saline density currents produced in a circular cross-section channel were focused on, and then they established a theoretical model which coincides well with the experimental results.

**Table 1-1** Summary of flow properties of the turbidity currents observed in Congo Canyons (Azpiroz-Zabala *et al.*, 2017)

Flow	1	2	3	4	5	6	Mean
Duration (days)	10.1	5.5	5.2	6.6	6.3	6.3	6.7
Maximum thickness (m)	53	57	48	69	77	68	62
Maximum ADCP velocity (m/s)	1.2	1.2	1	2.4	1.9	1.4	1.5
Average ADCP velocity (m/s)	0.4	0.4	0.3	0.7	0.5	0.4	0.5
Front propagation velocity (m/s)	0.8	0.8	0.7	1.6	1.5	1.0	1.1
Average height of maximum velocity above the bed (m)	6.8	6.9	5.8	14.2	11.8	10.0	9.3
Time of maximum velocity after arrival of the flow front (min)	25	34	100	8	25	25	36
Average sediment concentration (% <sub>vol</sub> ) <sup>*</sup>	0.018	0.020	0.020	0.023	0.020	0.017	0.020
Peak sediment concentration (% <sub>vol</sub> ) <sup>*</sup>	0.076	0.047	0.086	0.163	0.168	0.155	0.116
Maximum flow discharge (10 <sup>3</sup> m <sup>3</sup> /s)	4.6	4.9	2.7	14.9	16.3	10.4	9.0
Average flow discharge (10 <sup>3</sup> m <sup>3</sup> /s)	2.4	2.8	1.6	6.9	6.0	3.7	3.9
Maximum sediment discharge (10 <sup>3</sup> kg/s) <sup>*</sup>	3.1	2.7	2.0	13.2	9.0	6.1	6.0
Average sediment discharge (10 <sup>3</sup> kg/s) <sup>*</sup>	1.2	1.5	8.8	4.3	3.2	1.7	2.1
Water volume displaced (km <sup>3</sup> )	2.1	1.4	0.7	4.0	3.3	2.1	2.3
Sediment volume displaced (Mt) <sup>*</sup>	1.0	0.7	0.4	2.5	1.7	0.9	1.2
Organic carbon displaced (Mt) <sup>†</sup>	0.04	0.03	0.02	0.10	0.07	0.04	0.05

<sup>\*</sup>Assuming a uniform grain size of 4.23  $\mu\text{m}$  for inverting ADCP backscatter to sediment concentration (see Materials and Methods). <sup>†</sup>Assuming an average carbon content of 3 to 5% weight, as measured within turbidity current deposits on the Congo Fan (see Materials and Methods) (37).

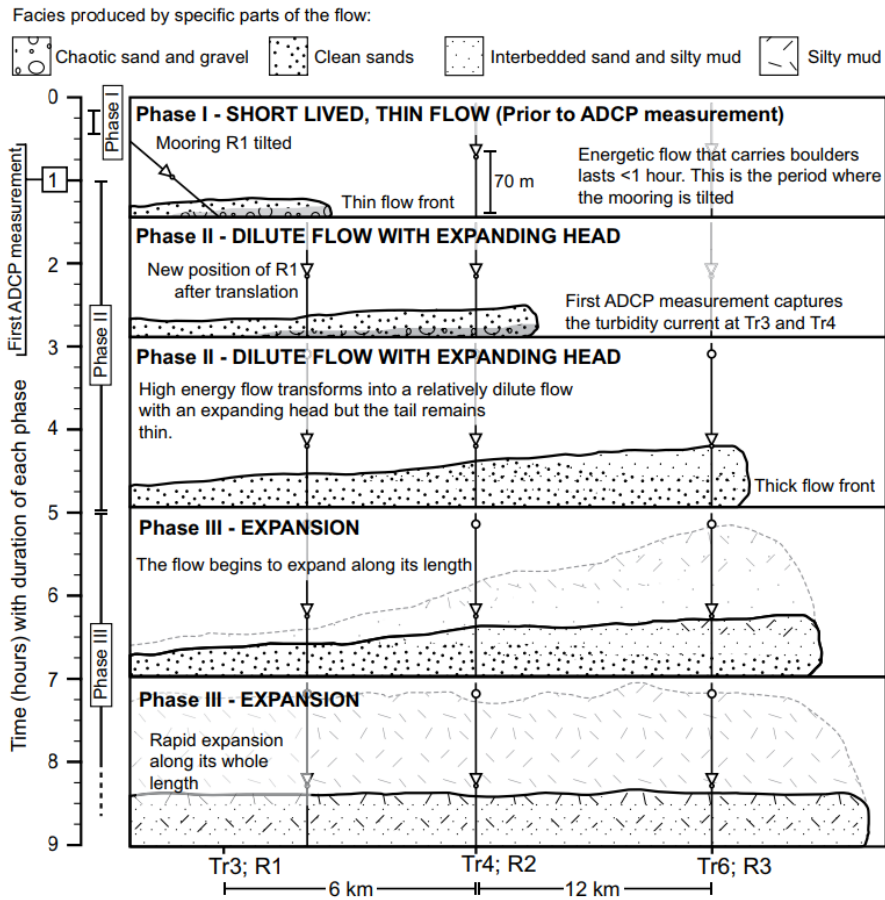


**Fig. 1-1** Schematic of evolution of flow structure and composition of the turbidity current observed in Monterey Bay (Symons *et al.*, 2017)

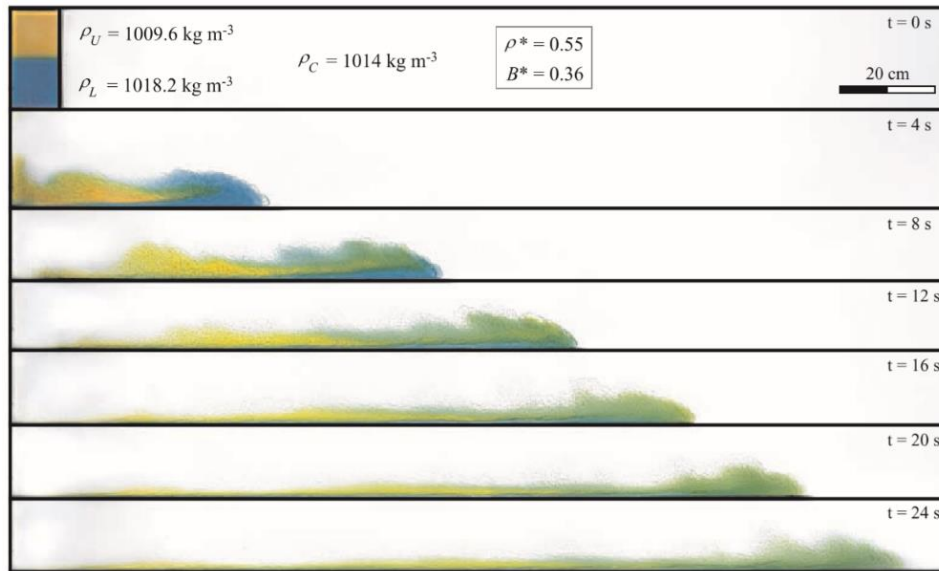


**Fig. 1-2** Experimental images of the developing two-layer saline density current in case of  $\rho^* = 0.55$  and  $B^* = 0.36$  (Gladstone *et al.*, 2004)

## 1.2. Ultrasonic measurement techniques and multi-phase flows

In some laboratory experiments and industries, acoustic measurement techniques have been widely used, because they have strong advantages of (i) utility to apply to opaque fluids and inside the opaque materials (e.g. metal pipeline), (ii) non-invasive measurement, and (iii) wide measurable velocity range. Ultrasonic velocity profiler (UVP) (Takeda, 2012) is one of the most used devices in the field of fluid measurement, and UVP made it possible to measure the spatio-temporal velocity distributions along the ultrasonic beam, using frequency veering based on Doppler effects of ultrasonic waves. Along with the advance in ultrasonic measurement technique, the needs for ultrasonic measurement have also diversified and become complicated. In order to obtain such complicated flow fields, some advanced techniques have been established. One example is ultrasonic imaging velocimetry (UIV) or echo-PIV using array transducers (e.g. Poelma, 2017). In this method, two-dimensional echo image is generated by converting echo amplitude values received by each transducer element to gray scale values. Then, the cross-correlation method used in particle imaging velocimetry (PIV) is applied for two consecutive echo images, and vector fields can be obtained. In the study by Zheng *et al.* (2006), the results measured by UIV provided good agreement with the vector fields measured by optical-PIV (see Fig. 1-3).

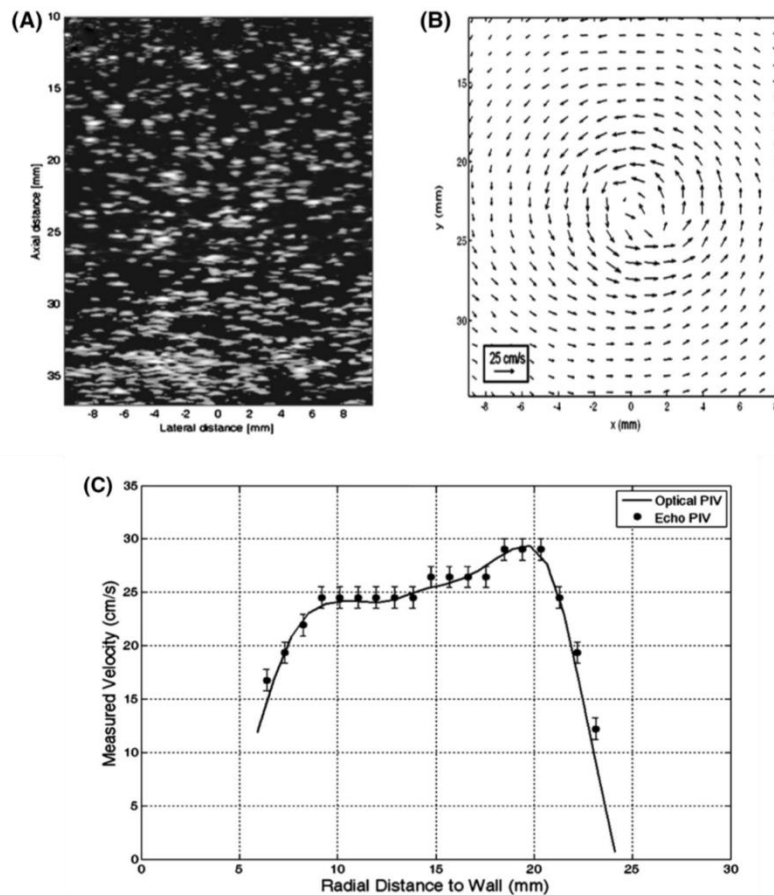


**Fig. 1-3** Validation of echo-PIV using a vertical flow: (a) B-mode particle image of the flow; (b) velocity field measured by echo-PIV; and (c) echo-PIV and optical PIV velocities along one radial line within the flow field (Zheng *et al.*, 2006)

Another one is phased-array transducer system (e.g. Kikura *et al.*, 2016; Kang *et al.*, 2016). In this method, adding a phase difference to the emitted ultrasonic waves from each element, spatial two- or three-dimensional echo images as well as measurement line can be generated. Murakawa *et al.* (2008) established unique ultrasonic measurement device using a dual-frequency Doppler transducer for bubbly flows, which makes it possible to measure both velocity distributions of tracer particles (liquid phase) and bubbles (gas phase) (see Fig. 1-4).

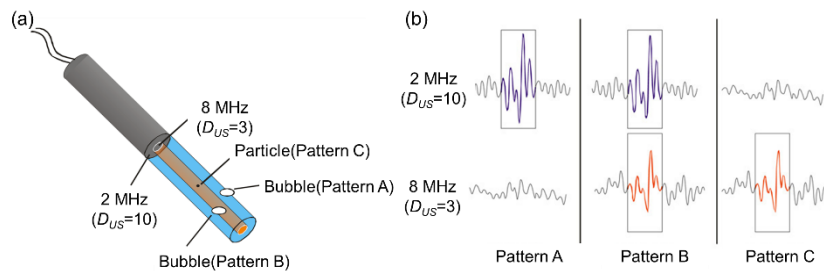


**Fig. 1-4 Schematic image of measurement principle using ultrasonic multi-wave method (Murakawa *et al.*, 2008)**

In addition to the contraption for the arrangement of ultrasonic transducers, another approach has been conducted, which is utilizing echo intensities information termed echo intensity method. Echo intensity, which is the strength of reflected ultrasonic waves scattered on interfaces between two media having different acoustic impedance, gives us beneficial information. In past studies, echo intensity obtained from UVP could be used to detect moving interfaces of air-water bubbly channel flow by Murai *et al.* (2010). Hitomi *et al.* (2017) used echo intensity of pulse repetition method to detect and monitor the air-oil-water three-layer pipe flows (see Fig. 1-5). Su *et al.* (2017) revealed the relationship between the attenuation coefficient and the phase fraction in oil-water two-phase pipe flows. Shi *et al.* (2019) established the method to characterize oil-gas-water three-phase flow using time-frequency decomposition. Dong *et al.* (2015) measured velocity distributions of oil-water two-phase flows using continuous ultrasonic waves. Additionally, echo intensity method was applied to obtain the profiles of suspended sediment concentration mentioned below and to measure the profiles of void fraction in bubbly flows (Murai *et al.*, 2009).

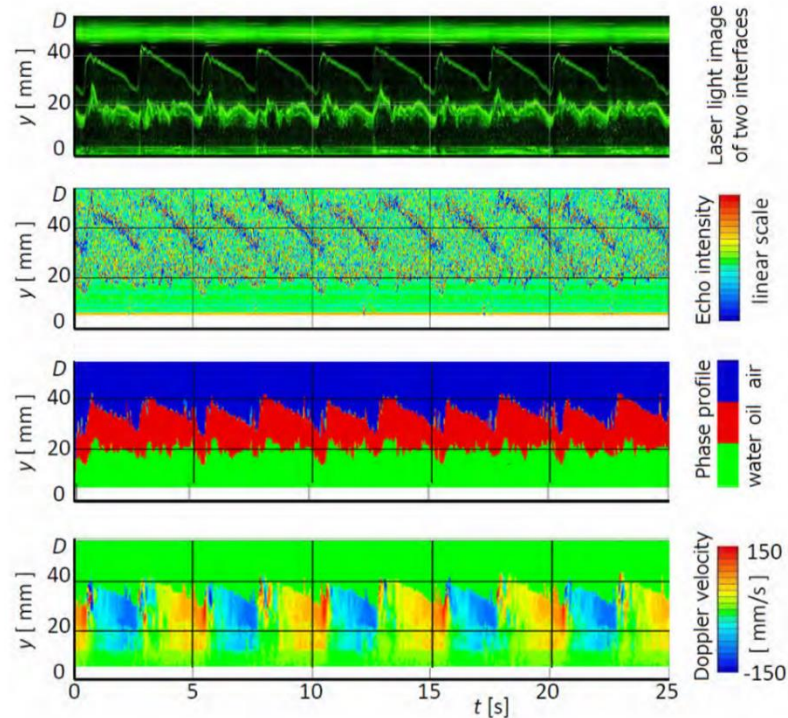


**Fig. 1-5** Samples of interface detection: (a) optical visualization, (b) echo intensity distribution, (c) phase distribution, and (d) Doppler velocity distribution (Hitomi *et al.*, 2017)

### 1.3. Final goal and objective of this study

As mentioned above, the final goal of this study is to elucidate the long-distance propagation mechanism of turbidity currents occurring in nature under rivers, seas, and so on. In order to achieve this purpose, it is required to reveal the inner flow structures and the condition determining the flow behaviors of turbidity currents. The turbidity currents in nature, however, have huge flow structures, so it seems difficult to obtain sufficient and quantitative detailed data from field researches. Additionally, these have complicated flow structures due to turbulence and complex interaction caused between each particle. The turbidity currents show local mixture density fluctuation accompanying clusters and clouds of particles, which is hardly investigated by optical approaches and numerical simulations. Our research group, therefore, has ascribe experimental studies as a suitable option to take not only basic but also advanced knowledge to estimate the behavior of turbidity currents.

To evaluate the flow behaviors of such experimental turbidity currents quantitatively, the measurement techniques, which can be applied to opaque flows with high resolutions, is required. Therefore, it is necessary to expand the utility of ultrasonic measurement techniques for solid–liquid two–phase flows. Based on the above discussions, the objective of this study is written below.

- To elucidate the long-distance propagation mechanism of turbidity currents from



experimental results by the lock-exchange technique

- To expand the utility of ultrasonic measurement techniques, which can be applied to solid–liquid two–phase flows

Experiments, analysis and discussions along the above objectives are described from the next chapter.

## 1.4. Nomenclature

$\rho_W$	Density of water	[kg/m <sup>3</sup> ]
$\rho_H$	Density of heavier fluids	[kg/m <sup>3</sup> ]
$\mu_W$	Viscosity of water	[Pa · s]
$\mu_H$	Viscosity of heavier fluids	[Pa · s]
$d_{50}$	Center diameter of particles	[m]
$v_s$	Settling velocity	[m/s]
$Re_p$	Particle Reynolds number	[-]
$\rho_P$	Density particles	[kg/m <sup>3</sup> ]
$\alpha$	Volume fraction of particles	[%]
$x_I, y_I$	Intersection point of two ultrasonic beams	[m]
$U_f$	Front velocity	[m/s]
$U_f^*$	Dimensionless front velocity	[-]
$g$	Gravitational acceleration	[m/s <sup>2</sup> ]
$g'$	Reduced gravitational acceleration	[m/s <sup>2</sup> ]
$t^*$	Estimated arrival time	[s]
$h$	Flow layer thickness	[m]
$U$	Layer-averaged velocity	[m/s]
$h_t$	Height where horizontal velocity takes zero	[m/s]
$h_m$	Height where horizontal velocity takes maximum	[m/s]
$u_{\max}$	Maximum horizontal velocity	[m/s]
$u^*$	Friction velocity	[m/s]
$y_0$	Zero-velocity roughness height	[m]
$\tau_W$	Wall shear stress	[Pa]
$\kappa$	von Karman constant	[-]
$C_f$	Friction coefficient	[-]
$\Delta t_{UVP}$	Temporal resolution of UVP	[s]
$St$	Stokes number	[-]
$Re$	Reynolds number	[-]
$Fr'$	Densimetric Froude number	[-]
$Ri$	Richardson number	[-]
$u_{\text{mean}}$	Mean velocity	[m/s]

## 2. Experimental method

### 2.1. Experimental facility

Several types of gravity currents were generated in a flume by means of the lock-exchange technique, which has been widely used to investigate unsteady currents in laboratory experiments (e.g. [Theiler and Franca, 2016](#)). Schematic diagram of the experimental facility is shown in [Fig. 2-1](#) and the picture of the facility is shown in [Fig. 2-2](#). The test section is an inclined rectangle flume with 4,548 mm in length, 210 mm in height and 143 mm in width. Surface on side and bottom walls of the flume walls is lubricated, and top boundary of the fluid layer is free surface. One of the walls is transparent whereas the other is coated with a non-reflective black film, producing a dark uniform and contrasting background for flow visualization. The region surrounded by a dotted square in [Fig. 2-1](#) indicates the area for optical visualizations. A lock gate 1 made of plastic plate is positioned at roughly half length of the flume. As an initial condition, the left-side region of the flume separated by the gate 1 is occupied by a heavier fluid with bulk density  $\rho_H$  while the right-side region is filled with tap water with density  $\rho_W$  as the ambient fluid. As experimental conditions of ambient fluid summarized in [Table 2-1](#), temperature and density of tap water were almost constant, 8.0°C and 999.9 kg/m<sup>3</sup>, respectively. When the gate 1 is released, the heavier fluid invades under the ambient fluid with front velocity  $U_f$  according to the density difference between both fluids. The horizontal displacement from the gate in the right region is defined as  $x$  axis and  $y$  axis denotes the height from the bed. For one-layer turbidity currents, which are examined in laboratory experiments normally, one separation gate (gate 1 only) is enough as shown in [Fig. 2-1\(a\)](#). In this study, in addition to the one-layer currents, two-layer currents were examined using two separation gates (gate 1 and gate 2) as shown in [Fig. 2-1\(b\)](#) to observe the difference of flow behaviors depending on the initial conditions or variation of sediment particles. In cases of two-layer currents, the gate 2 was firstly released to generate density difference between heavier particle-suspended fluid in the tank A and lighter particle-suspended fluid in the tank B. Then, the gate 1 was barely released before the head of heavier particle-suspended fluid reached the gate 1, and two-layer currents propagated in the right-side region.

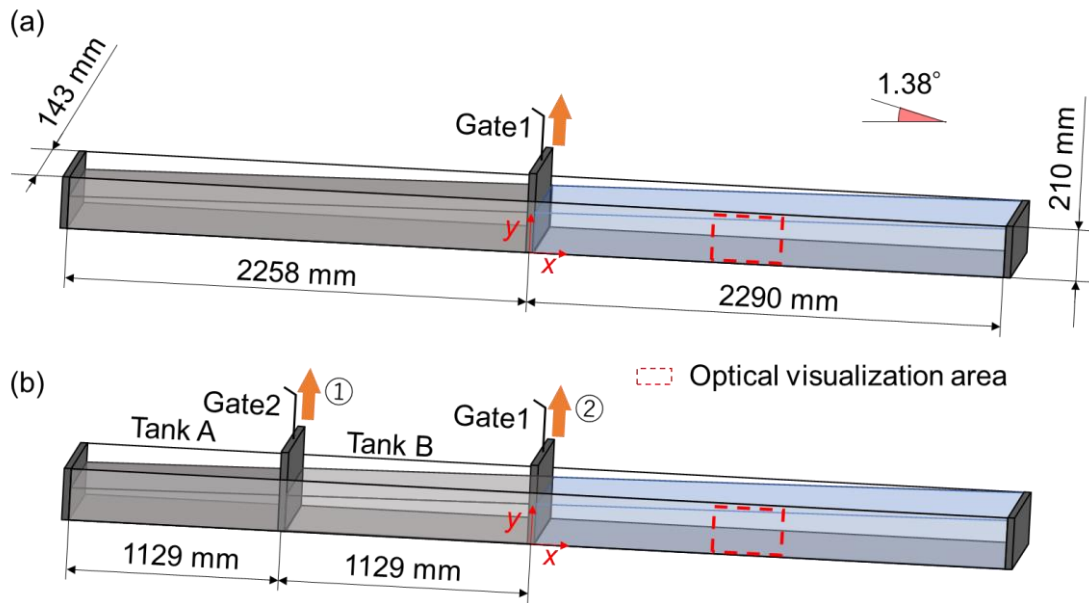


**Fig. 2-1** Experimental facility of lock-exchange technique

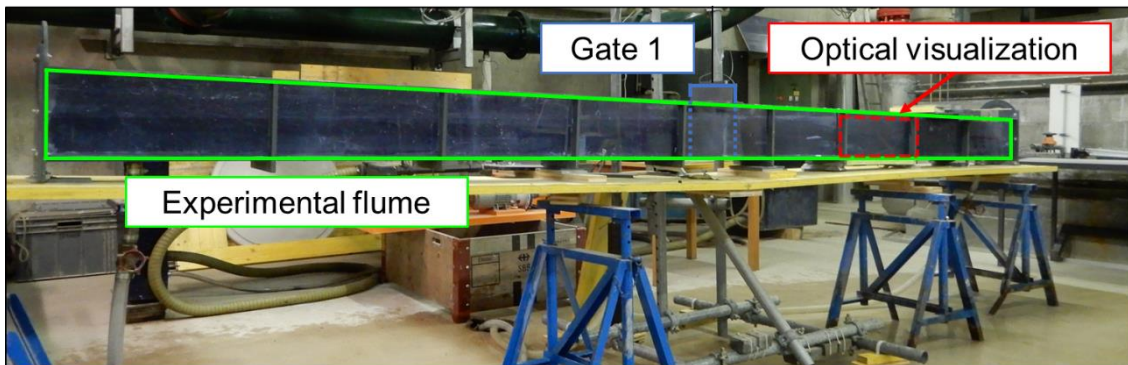


**Fig. 2-2** Picture of the experimental facility

**Table 2-1** Experimental conditions of the ambient fluids

Temperature of water	8.0 °C
Density of water, $\rho_w$	999.9 kg/m <sup>3</sup>
Viscosity of water, $\mu_w$	1.385 mPa·s

## 2.2. Sediment particles



**Fig. 2-3** Pictures of sediment particles, left-side is the quartz particles and right-side is the opalin particles

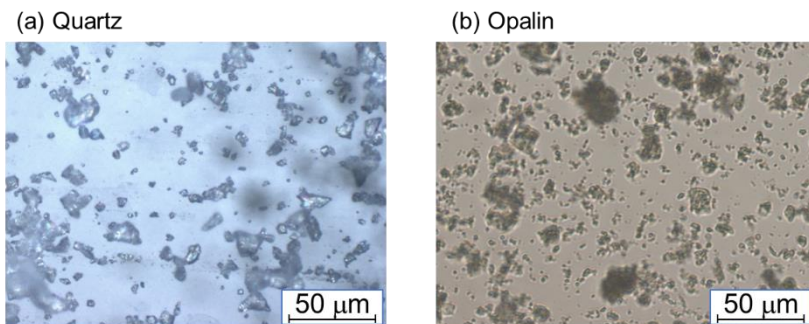


**Fig. 2-4** Particle images taken by electron microscope

As suspended materials, two kinds of particles, quartz (Cario Bernasconi S.A., K-13) and opalin (Opalit AG Holderbank, Opalit), were examined (see Fig. 2-3), and their microscope photographs are shown in Fig. 2-4. Particle size distributions of them measured by MasterSizer 3.0 (Malvern S. A., 2013) are shown in Fig. 2-5. In these distributions, a dispersion of the particle size distribution in case of the quartz particles is smaller than case of the opalin particles. The calculated center diameter and other physical properties mentioned in their specifications are summarized in Table 2-2. The calculated center diameters of quartz and opalin are 12.2 and 18.9  $\mu\text{m}$ , respectively. The quartz particles are almost composed of  $\text{SiO}_2$ , while the opalin are composed of not only  $\text{SiO}_2$  but also  $\text{Al}_2\text{O}_3$ ,  $\text{Fe}_2\text{O}_3$ , and so on. From these results, each particle-suspended fluid is expected to have different rheological characteristic and it would cause the change of their flow structures.

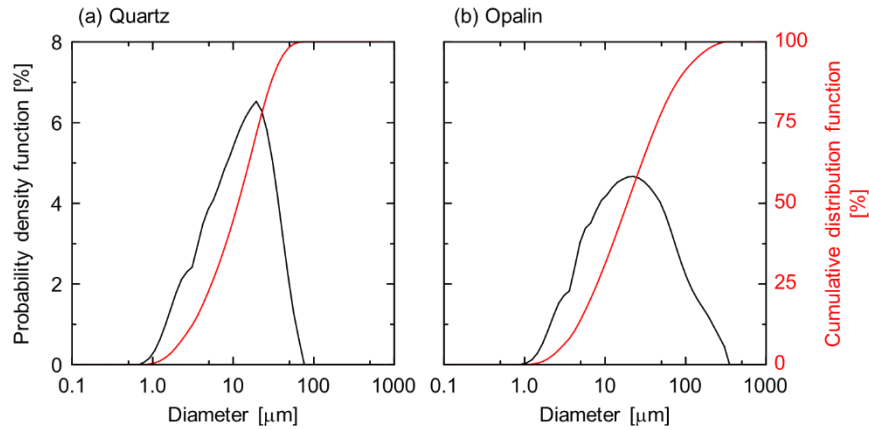


**Fig. 2-5** Particle size distributions of (a) quartz particle and (b) opalin particles

**Table 2-2** Basic information about suspended particles

	Quartz		Opalin	
Center diameter, $d_{50}$ [mm]		12.2		18.9
Density, $\rho_p$ [kg/m <sup>3</sup> ]		2650		2740
Contained materials	SiO <sub>2</sub>	98.30%	SiO <sub>2</sub>	50%
	Al <sub>2</sub> O <sub>3</sub>	0.08%	Al <sub>2</sub> O <sub>3</sub>	19%
	K <sub>2</sub> O	0.40%	Fe <sub>2</sub> O <sub>3</sub>	8.0%

As mentioned above, the specific weights of quartz and opalin particles are larger than 1.0, so the settling of the particles occurs in a still-water. Such a settling velocity  $v_s$  is estimated by Stokes' law written as

$$v_s = \frac{d_p^2 (\rho_p - \rho_w) g}{18\mu_w}, \quad (2-1)$$

where  $d_p$  and  $g$  indicate the diameter of the particle and gravitational acceleration, respectively. The values of  $v_s$  in case of quartz and opalin calculated based on each center diameter  $d_{50}$  are 0.0965 and 0.244 mm/s, respectively. This law can be applied only for the particle Reynolds number  $Re_p$  shown below is smaller than 2,

$$Re_p = \frac{d_p v_s \rho_w}{\mu_w}. \quad (2-2)$$

As the result of the calculation, the values of  $Re_p$  for each particle were confirmed to be much smaller than 2, so the Stokes' law works.

### 2.3. Experimental cases

Totally, twenty-five series of experiments using some kinds of different heavier fluids and initial conditions were performed, and experimental conditions about heavier fluids are summarized in [Table 2-3](#). In the table, capitalized alphabet denotes the kind of heavier fluids, that is Q, S, and O show quartz-suspended fluid, saline-dissolved fluid, and opalin-suspended fluid, respectively. In Case 1–8, quartz-suspended turbidity currents, which are water containing quartz particles with 0.5% in volume fraction, were performed, and bulk density of heavier fluids  $\rho_H$  in those cases is 1008 kg/m<sup>3</sup>. In case 9 and Case 10–12, heavier fluid contains quartz particles with 1.0% in volume fraction ( $\rho_H = 1016$  kg/m<sup>3</sup>) and 2.0% ( $\rho_H = 1032$  kg/m<sup>3</sup>), respectively. In case 13–15, saline density currents colored with white ink were examined for  $\rho_H$  fixed at 1008 kg/m<sup>3</sup> in these three cases. In Case 16–18, opalin-suspended turbidity currents, which are water containing opalin particles, and  $\rho_H$  is different from each other between 1008 to 1032 kg/m<sup>3</sup>. In Case 19–25, two-layer turbidity currents were performed. In Case 19–22, the density in the lower layer is 1032 kg/m<sup>3</sup> and that in the upper layer is 1016 kg/m<sup>3</sup>. In Case 23–25 the density in the upper layer is 1032 kg/m<sup>3</sup>. The densities of each lower layer are 1016 kg/m<sup>3</sup> in the Case 22 and 25, and 1032 kg/m<sup>3</sup> in the Case 24.

In this study, there are two types of the ultrasonic transducers arrangements as shown as I or II in [Table 2-3](#), then the details of the arrangement and principle of velocity measurement by UVP are explained in next section.

**Table 2-3** Experimental conditions of heavier fluids

Exp. case	Density [kg/m <sup>3</sup> ]		Arrangement of transducers
	Tank A	Tank B	
1		Q: 1008	I
2		Q: 1008	I
3		Q: 1008	II
4		Q: 1008	II
5		Q: 1008	II
6		Q: 1008	II
7		Q: 1008	II
8		Q: 1008	I
9		Q: 1016	I
10		Q: 1032	I
11		Q: 1032	I
12		Q: 1032	I
13		S: 1008	I
14		S: 1008	I
15		S: 1008	I
16		O: 1008	I
17		O: 1016	I
18		O: 1032	I
19	Q: 1032	Q: 1016	I
20	Q: 1032	O: 1016	I
21	O: 1032	Q: 1016	I
22	Q: 1032	Q: 1016	I
23	Q: 1016	O: 1008	I
24	Q: 1032	O: 1008	I
25	O: 1016	Q: 1008	I

### 3. Development of analysis method

#### 3.1. Velocity measurement

Ultrasonic velocity profiler (UVP) (Takeda, 2012), which measures instantaneous profiles of velocity component along the propagation line of ultrasonic wave and is applicable to opaque fluids was adopted for the measurement of velocity profiles in the currents. In this method, using the frequency veering according to Doppler effect, spatio-temporal velocity distributions can be measured.

##### 3.1.1. Supplemental experiments by stirring flow

As mentioned above, quartz and opalin particles with order of 10  $\mu\text{m}$  in the central diameter are examined. This range of particle diameter is less than one-tenth the ultrasonic wavelength of central frequency 4 MHz in water, so Rayleigh scattering, which is almost isotropic scattering, occurs. Such small particles are not used for UVP measurement basically, because the intensity of reflected waves from a quartz particle is too small to be detected by ultrasonic transducers. In ordinary UVP measurements, it is considered that the adequate diameter of the tracer particles as reflector is appropriately quarter to half of the ultrasonic wave length. Fig. 3-1 shows the schematic diagram of those scattering patterns. In this part, therefore, a series of supplemental experiments was conducted by the stirring flows shown in Fig. 3-3 to elucidate the flow conditions and the volume fractions of the quartz particles that UVP can measure reasonable velocity distributions of particle-laden flows. The experiments were conducted in a cylindrical container with 100 mm in outer diameter, and 3 mm in thickness of lateral wall and 120 mm in height. The cylinder is made of acrylic resin and filled with test fluids containing the fine particles. The cylinder does not have a lid and thus top of fluid layer is free surface. The cylinder was mounted inside the water jacket to keep uniform temperature and allow transmission of ultrasonic wave from the outside of the cylinder. The flow was driven by a stirrer with 60 r.p.m. in the rotational speed, and a stirring bar dipped into the bottom of the cylinder. An ultrasonic transducer was fixed in the jacket with a horizontal displacement 10 mm from the center line. This off-axis measurement makes it possible to obtain the velocity component including not only radial but also azimuthal velocity component. The transducer was set at 25 mm from the bottom of the cylinder to avoid the blind of ultrasonic propagation due to the free surface. In Table 3-1, the setting parameters of UVP measurement for supplemental experiments are summarized. Each value of spatial resolution, number of cycles, and number of repetitions is same value in the measurements for the gravity currents in this study. The velocity range of the stirring flows is larger than that of the gravity currents, so temporal resolution is higher. The cylinder was filled with 500 mL of tap water and the quartz particles were added based on each volume fraction  $\alpha$ . Total seven cases with different volume fractions,  $\alpha = 0, 0.01, 0.1, 1.0, 5.0, 10, \text{ and } 15\%$ , were conducted, and the sample images of the fluids for  $\alpha = 0.01, 1.0, \text{ and } 10\%$  are shown in Fig. 3-2. As you can see, in cases of  $\alpha > 1\%$ , the test fluid becomes completely opaque, so the inner flow structures cannot be observed by optical approaches.

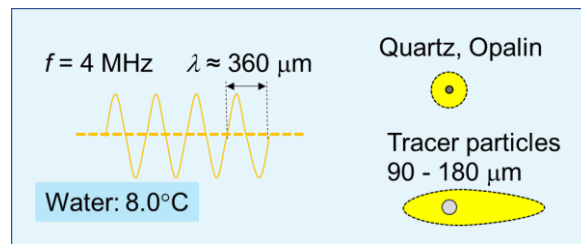


**Fig. 3-1** Schematic diagram of scattering patterns reflected by each particle

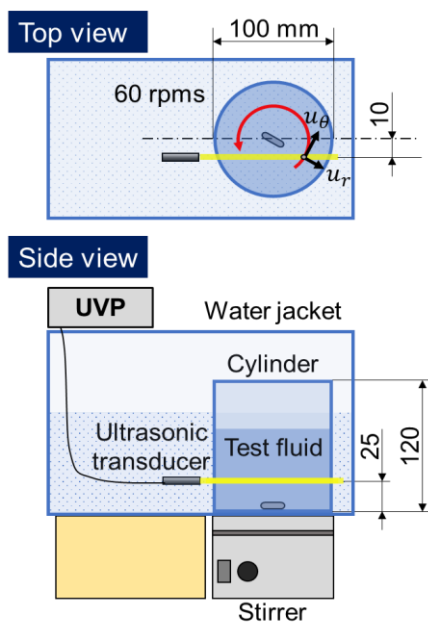


**Fig. 3-3** Schematic diagram of experimental setup for stirring flow

**Table 3-1** Setting parameters for supplemental experiments

Central frequency	4	MHz
Temporal resolution	10	ms
Spatial resolution	0.74	mm
Number of cycles	4	-
Number of repetitions	32	-
Amplification (gain)	6 - 6	-

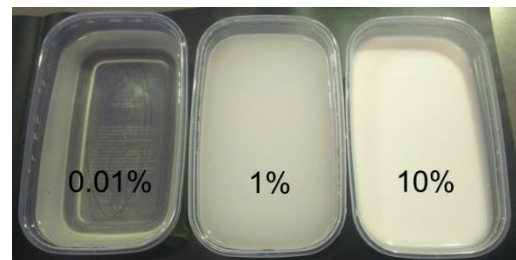


**Fig. 3-2** Sample images of test fluids

From these experiments, we tried to comprehend the trends of velocity profiles measured in this setup. Fig. 3-4 shows velocity distributions obtained from UVP in each experimental case. These velocities show the components of the measurement direction, that contain the azimuthal and radial velocity components. The measurements and the time-averaging were conducted for 40 s after the flows reached adequate developed states, so the corresponding number of the velocity profiles for time-averaging is 4000. In this figure,  $x$  axis donates the distance from the center of the cylinder and the ultrasonic measurement direction is from left to right side. In the cases of  $0.1 \leq \alpha \leq 5\%$ , reasonable velocity distributions can be observed. In this study, the velocity profiles measured with usual tracer particles (Mitsubishi Chemical, DIAION HP20SS, diameter 60–150  $\mu\text{m}$ , density 1020  $\text{kg}/\text{m}^3$ ),

which are indicated as orange dotted line in Fig. 3-4, is assumed as correct distribution, and “reasonable velocity distribution” means having good agreement with the correct distribution. The velocity profiles of  $0.1 \leq \alpha \leq 5\%$  have an accuracy that has a high cross-correlation value exceeding 0.95 for the correct distribution. The cases of  $\alpha = 10$  and 15%, however, do not show the reasonable velocity distributions. It seems that the influence of the scattering attenuation of ultrasonic waves occurring in cases of Rayleigh scattering becomes large and that prevents the ultrasonic transducer from detecting the echo signals. In addition, the case of  $\alpha = 0.01\%$  shows a notable result. The velocity values of this case drop irregularly near the center of the cylinder. This phenomenon implies that the amount of quartz particles is much fewer than wall side due to the centrifugal force. As known from the velocity distribution, high velocity values can be observed near the center. As the distance from the center becomes longer, the velocity values are getting smaller. From these distributions, the existence of a free vortex seems to be confirmed. The density of the quartz particles is about 2.65 times higher than that of water, so it is possible that the particles are blown from the center to near the wall sides by the centrifugal force.

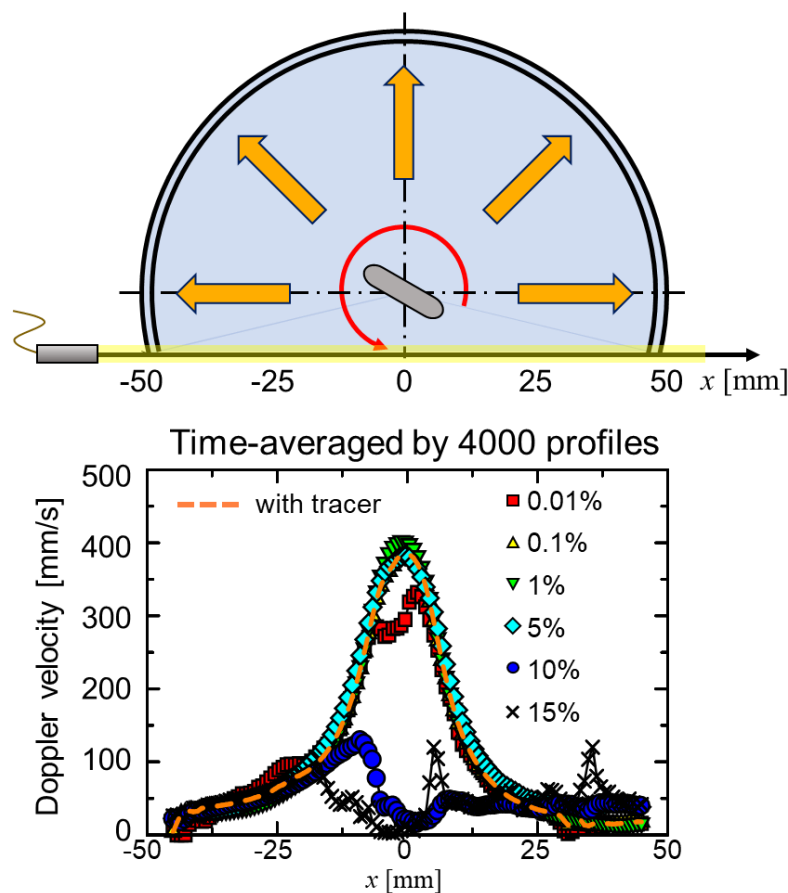


**Fig. 3-4** Profiles of time-averaged value of Doppler velocity

In addition to the velocity distributions, time-averaged echo amplitude profiles are also shown in Fig. 3-5. These echo amplitudes were calculated as the absolute values of difference from UVP echo intensity in case of background ( $\alpha = 0\%$ ). As the volume fraction becomes larger in the cases of  $\alpha = 0.01, 0.1, \text{ and } 1\%$ , echo amplitude values are also getting larger. In the case of  $0.01 < \alpha < 1\%$ , on the opposite side from the ultrasonic transducer, an extremely large value of echo amplitude is observed because of the reflection from the wall. In contrast, the reflected waves from the opposite wall disappears under the conditions  $\alpha \geq 5\%$  due to the attenuation of ultrasonic waves, and the attenuation is getting larger depending on their volume fractions.

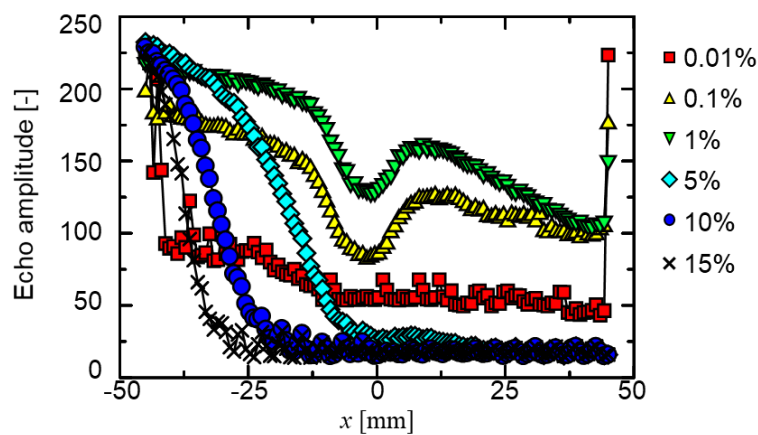


**Fig. 3-5** Profiles of time-averaged value of echo amplitude

Basically, UVP measurements are applied to flows containing tracer particles with adequate size, density, and concentration to reflect ultrasonic waves. However, the concentrations of particles in these experiments are relatively larger in comparison with the flows which UVP measurements are applied to normally. The experimental results for  $0.1 \leq \alpha \leq 5\%$  show reasonable velocity distributions. This range of particle concentration, therefore, might be useful to detect integral echo signals obeying Rayleigh scattering. That is why UVP can obtain velocity distribution, although quartz diameter is much smaller than tracer particles (Hitomi *et al.*, 2018).

### 3.1.2. Velocity measurements for gravity currents

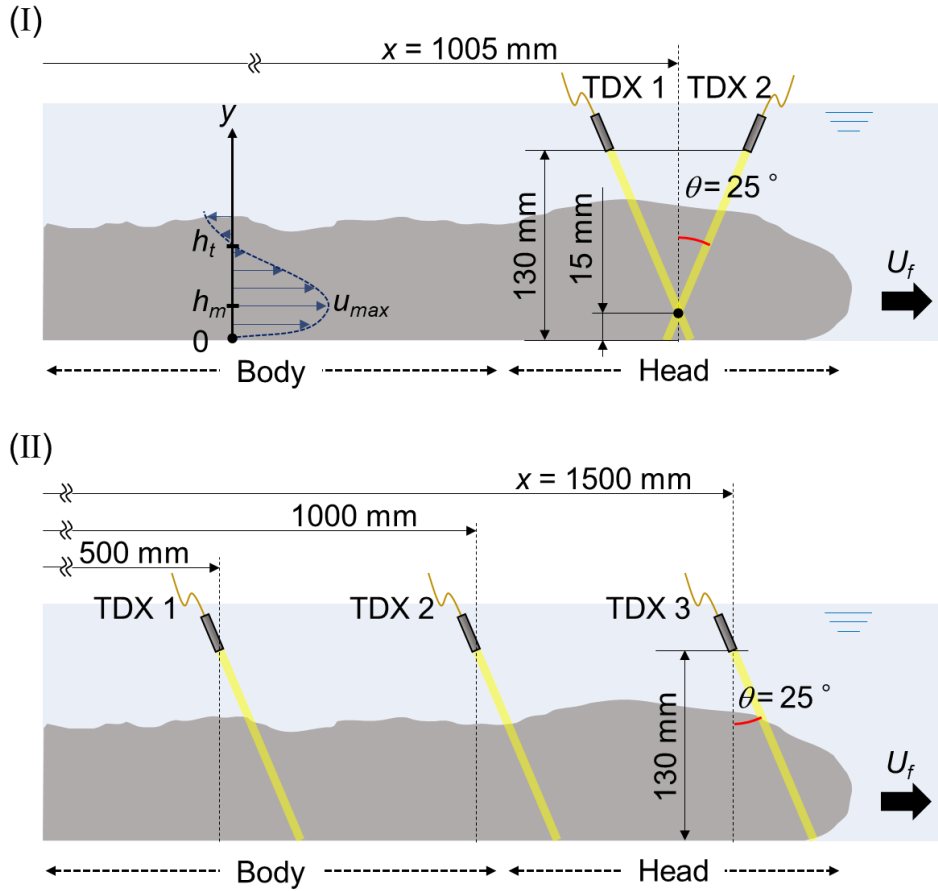


**Fig. 3-6** Schematic image of arrangement of ultrasonic transducers

As mentioned above, there are two types of the ultrasonic transducer arrangements in this study. In more than half of the experiments, as shown in Fig. 3-6(I), a pair of ultrasonic transducers was used for the measurement. Such a symmetric arrangement of two measurement lines has been used in some studies, because that makes it possible to obtain instantaneous profiles of both horizontal and vertical velocity components ( $u$  and  $v$ ) at their crossing point using following equations (Jamshidnia and Takeda, 2010; Kitaura *et al.*, 2010 (in Japanese)),

$$u(y, t) = \frac{u_1(y, t) - u_2(y, t)}{2 \sin \theta}, \quad (3-1)$$

$$v(y, t) = -\frac{u_1(y, t) + u_2(y, t)}{2 \cos \theta}. \quad (3-2)$$

In many cases of the previous studies, the relationship shown by these equations has been extended in the entire height direction to estimate multi-component or multidimensional flow field assuming that the tilted angle  $\theta$  is sufficiently small. In this study, two ultrasonic transducers with 4 MHz in basic

frequency connected to each equipment of UVP model Duo (Met-Flow S.A., Switzerland) were installed with tilt angle of  $25^\circ$  from the  $y$  axis. Those two measurement lines of the transducers intersect at  $(x_l, y_l) = (1005 \text{ mm}, 15 \text{ mm})$ , where  $y_l$  is the height expected roughly that the horizontal velocity takes the maximum value  $u_{\max}$  according to previous researches. For instance, in the study by Keller *et al.*, (1999), the height  $h_m$  taking velocity maximum within the body region of the saline density currents is reported to occur at  $h_m/d \approx 0.2$  in the rectangular lock-exchange flume using Laser-Doppler anemometry, where  $d$  is the flow thickness of the currents. The start time of the two-UVP measurement was synchronized with the release of the gate 1, continuing sufficiently long measurement time to analyze flow structures from head to body of the currents.

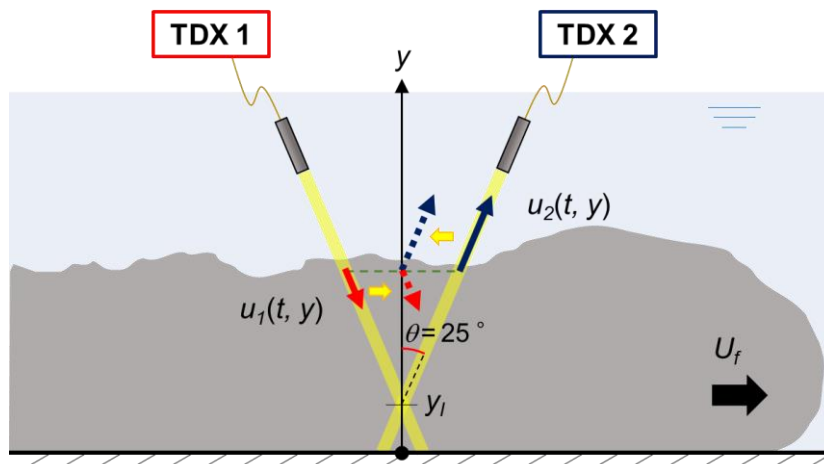


**Fig. 3-7 Schematic diagram of concept of the time correction method <sup>0</sup>**

In addition, since the positions of two ultrasonic transducers in this arrangement have a certain displacement outside the intersection point, our research group suggests the time correction method of velocity distributions using front velocity  $U_f$  (Nomua *et al.*, 2018a; Nomua *et al.*, 2018b). Although the details about  $U_f$  will be described in another section, the currents in experimental cases of high-volume release like this study propagate with almost constant front velocity. The high-volume release means that the initial volume of the heavier fluids is relatively similar to that of ambient fluid in this study. The schematic diagram of this method is described in Fig. 3-7. Using this concept, Eq.( 3-1 ) and Eq.( 3-2 ) are modified as follows,

$$u(y, t) = \frac{u_1(y, t - \Delta t) - u_2(y, t + \Delta t)}{2 \sin \theta}, \quad (3-3)$$

$$v(y, t) = -\frac{u_1(y, t - \Delta t) + u_2(y, t + \Delta t)}{2 \cos \theta}, \quad (3-4)$$

$$\text{where } \Delta t = \frac{(y - y_I) \tan \theta}{U_f}. \quad (3-5)$$

In the remaining several experiments, in order to observe the temporal and spatial development of the currents, three ultrasonic transducers connected to one UVP equipment were arranged in parallel as shown in Fig. 3-6(II), and the measurement by the multiplexer mode was performed. The positions of each transducer were  $x = 500, 1000, 1500$  mm, respectively. The setting parameters for UVP measurement are specified in Table 3-2.

**Table 3-2 Setting parameters for UVP measurement**

Basic frequency	4 MHz
Spatial resolution	0.74 mm
Number of cycles	4
Repetition	32
Temporal resolution	(I) 50 ms (II) 190 ms $\times$ 3

### 3.2. Concentration profiles

In addition to the velocity profiles using frequency veering based on Doppler effects, echo amplitude distributions reflecting waves scattered by suspended particles give us beneficial information on particle concentrations. The size of sediment material used in this study is much smaller than ultrasonic wave length  $\lambda$  ( $\sim 100 \mu\text{m}$ ) with 4 MHz frequency in water, that causes Rayleigh scattering. For such conditions, Thone and Hanes (2002) suggested the relationship between the mean-square amplitude of echo signal  $\langle V^2 \rangle$  received by the ultrasonic transducer and mass concentration  $M$  in  $\text{kg/m}^3$  as following.

$$M = \frac{4}{3} \pi a_s^3 \rho_p N, \quad (3-6)$$

where,  $a_s$  denotes the equivalent radius of suspended particles ( $\approx d_{50}/2$ ) and  $N$  is the number of particles per unit volume.

$$M(r) = \langle V^2 \rangle \left( \frac{\psi r}{K_s K_t} \right)^2 e^{4\alpha r} = \langle V^2 \rangle \left( \frac{\psi r}{K_s K_t} \right)^2 e^{4 \left( \alpha_w r + \int_0^r \xi M(r) dr \right)}, \quad (3-7)$$

where,  $\alpha_w$  is the clear water attenuation which is a function of the temperature only expressed as (Fisher and Simmons, 1977)



$$\alpha_w = 10^{-15} (55.9 - 2.37T + 4.477 \times 10^{-2} T^2 - 3.48 \times 10^{-4} T^3) F^2, \quad (3-8)$$

with  $T$  in Celsius degrees and  $F$  is the sound frequency in 1/s. Then  $\xi$  is sediment attenuation constant.

$$\xi = \frac{3}{4a_s \rho_p} \chi, \quad (3-9)$$

where,  $\chi$  is the normalized total scattering cross-section, and it is described as (Thone and Hanes, 2002)

$$\chi = \frac{1.1 \cdot \frac{4}{3} \cdot 0.18 (ka_s)^4}{1 + 1.3 (ka_s)^2 + \frac{4}{3} \cdot 0.18 (ka_s)^4}, \quad (3-10)$$

where  $k$  is the wave number of the sound in water ( $k = 2\pi/\lambda$ ,  $\lambda$  are the wavelength of ultrasonic wave, respectively).

Additionally,  $K_s$  is a function of the scattering properties of the suspended sediment,  $K_t$  is a constant for the ultrasound system, and  $\psi(r)$  accounts for the effect of the oscillating backscattered signal from the spherical spreading in the near field. Furthermore, Pedocchi and Garicía (2012) applied this relationship to the echo distributions obtained from UVP. Their study indicated that the echo signal displayed by the UVP software is result of the passing signal through AD converter. That divides echo signals into voltage variation with 14 bits, and the measurable range is in  $\pm 2.5$  V ( $2.5$  V = 8191;  $-2.5$  V = -8191). The echo signals are amplified by the “gain factors” (as “gain start” and “gain end” in the software). To amplify the echo values, it is reported that time variable gain (TVG) is used and unamplified echo signal can be obtained following this equation using absolute gain values of start  $G_s$  and end  $G_e$ . The details of amplification by UVP software are written in Table 3-3 and Fig. 3-8.

$$V = \frac{V_{amp}}{G_s} \left( \frac{G_s}{G_e} \right)^{\frac{r-r_s}{r_e-r_s}}, \quad (3-11)$$

where,  $V_{amp}$  is amplified echo signal, and  $r_s$  and  $r_e$  are the minimum and maximum measurable distance from the transducer.

**Table 3-3** Gain factors to amplify UVP echo signals (Oliver Mariette from Met-Flow, personal communication 2018)

Gain factor $G_s / G_e$	Basic frequency of ultrasonic transducer [MHz]		
	0.5 / 1	2 / 4	8
3	2.17	0.91	0.65
4	4.41	1.76	1.36
5	8.82	3.41	2.80
6	16.67	6.67	5.26
7	33.33	15.00	11.11
8	60.00	25.00	23.08
9	150.00	60.00	42.86

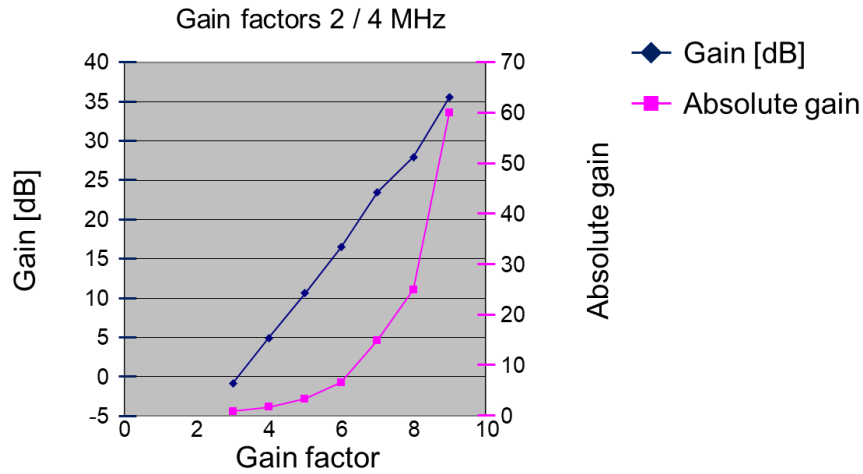


**Fig. 3-8** Gain factors for UVP echo signals monitored by the ultrasonic transducers with 2 or 4 MHz in basic frequency (Oliver Mariette from Met-Flow, personal communication 2018)

Here, a non-linearly is contained in the Eq.( 3-7 ), because the  $\alpha_s$  is also a function of  $M$ . To overcome this problem, Lee and Hanes (1995) established an explicit method to invert the equation by substituting the concentration at an initial point  $M_l$ . The procedure for the deformation of the formula is described below. Firstly, on the both sides of Eq.( 3-7 ) are taken by logarithm.

$$\ln M(r) = \ln \left( V^2 \right) \left( \frac{\psi r}{K_s K_t} \right)^2 e^{4\alpha r} = 2 \ln \left( r \sqrt{\langle V^2 \rangle} \right) + 2 \ln \left( \frac{\psi}{K_s K_t} \right) + 4 \ln \left( \alpha_w r + \int_0^r \xi M(r) dr \right). \quad (3-12)$$

Next, it takes the derivative with respect to  $r$  on both sides of the equation,

$$\frac{dM(r)}{dr} = 2 \left( \frac{r \frac{d\sqrt{\langle V^2 \rangle}}{dr} + \sqrt{\langle V^2 \rangle}}{r\sqrt{\langle V^2 \rangle}} \right) + 4(\alpha_w + \xi M(r)), \quad (3-13)$$

where  $\psi(r)$  can be treated as constant in case of the measurement for far field from the ultrasonic transducer not a near field (Downing *et al.*, 1995). Therefore, the second term on the right side of Eq.( 3-12 ) is handled as a constant, and it became zero by differentiating with respect to  $r$ .

$$\frac{dM(r)}{dr} - \left( 2 \frac{r \frac{d\sqrt{\langle V^2 \rangle}}{dr} + \sqrt{\langle V^2 \rangle}}{r\sqrt{\langle V^2 \rangle}} + 4\alpha_w \right) M(r) = 4\xi M(r)^2. \quad (3-14)$$

using the general solution of Bernoulli differential equations, the flowing equation can be obtained.

$$M(r) = \frac{\langle V^2 \rangle r^2 e^{4\alpha_w r}}{C - 4\xi \int \langle V^2 \rangle r^2 e^{4\alpha_w r} dr}, \quad (3-15)$$

where  $C$  denotes the integral constant. To set the boundary condition  $M(r = r_I) = M_I$ , finally it becomes

$$M(r) = \frac{r^2 \langle V^2 \rangle e^{4\alpha_w r}}{\frac{1}{M_I} r_I^2 \langle V^2 \rangle_I e^{4\alpha_w r_I} - 4\xi \int_{r_I}^r r^2 \langle V^2 \rangle e^{4\alpha_w r} dr}. \quad (3-16)$$

When the ideal condition on lock-exchange technique, the  $M_I$  is counted as zero, which means that the Eq.( 3-16 ) will diverge. It is required to set other boundary condition to overcome this problem. On the initial condition like this study, where the initial volume of heavier fluid is relatively similar to that of ambient fluid, the flow near the bed keeps containing the initial concentration as reported in (Theiler and France, 2016). That study shows the concentration profiles of colored density currents obtained by the image processing based on grayscale values, which was established by Nogueira *et al.* (2013). Applying this flow characteristic in case of turbidity currents where the high-volume release to this study, we rearranged Eq.( 3-15 ) by setting the boundary condition, where the concentration at the bottom is  $M_B$ . In that case, the equation becomes

$$M_B(r = r_B) = \frac{r_B^2 \langle V^2 \rangle_B e^{4\alpha_w r_B}}{C - 4\xi \int_{r_I}^{r_B} r^2 \langle V^2 \rangle e^{4\alpha_w r} dr}. \quad (3-17)$$

Therefore, the integral constant  $C$  is determined as

$$C = \frac{r_B^2 \langle V^2 \rangle_B e^{4\alpha_w r_B}}{M_B} + 4\xi \int_{r_I}^{r_B} r^2 \langle V^2 \rangle e^{4\alpha_w r} dr. \quad (3-18)$$

Substituting Eq.( 3-18 ) into Eq.( 3-15 ), the following equation is obtained,

$$M(r) = \frac{\langle V^2 \rangle r^2 e^{4\alpha_w r}}{\frac{r_B^2 \langle V^2 \rangle_B e^{4\alpha_w r_B}}{M_B} + 4\xi \int_{r_i}^{r_B} r^2 \langle V^2 \rangle e^{4\alpha_w r} dr - 4\xi \int_{r_i}^r \langle V^2 \rangle r^2 e^{4\alpha_w r} dr}. \quad (3-19)$$

Then, the equation is modified as,

$$M(r) = \frac{r^2 \langle V^2 \rangle e^{4\alpha_w r}}{\frac{1}{M_B} r_B^2 \langle V^2 \rangle_B e^{4\alpha_w r_B} + 4\xi \int_r^{r_B} r^2 \langle V^2 \rangle e^{4\alpha_w r} dr}. \quad (3-20)$$

It takes finally the discrete form,

$$M_n = \frac{r_n^2 \langle V^2 \rangle_n e^{4\alpha_w r_n}}{\frac{1}{M_B} r_B^2 \langle V^2 \rangle_B e^{4\alpha_w r_B} + 4\Delta r \xi \sum_{i=n+1}^N \left( r_i^2 \langle V^2 \rangle_i e^{4\alpha_w r_i} + r_{i-1}^2 \langle V^2 \rangle_{i-1} e^{4\alpha_w r_{i-1}} \right)}, \quad (3-21)$$

where  $n$  represents the position number of a certain measurement point when discretized.

### 3.3. Pattern matching method and front velocity

Outline motions of the fluids with the particles invading into the ambient fluid are monitored as successive images from  $t = t_0$  (Fig. 3-9), where  $t_0$  is an arbitrary elapsed time from the gate 1 release and the details about  $t_0$  will be mentioned later. The images were taken by the digital camera (Nikon, D5300) installed in front of the flume with 20 f.p.s. in frame rate for Case 1 and the shooting area is around  $x_l$  as shown in Fig. 2-1. The frame rate was set to the same value as the sampling rate of the UVP measurements in cases of arrangement I. In those images, some complicated flow structures can be observed near the upper boundary and the front part, which is caused by turbulent flow structure or interactions between the current and ambient fluid. In the study by Simpson and Britter (1979), tracing the shape of the vortices at the upper boundary, it was confirmed that the ratio of vortex structure to wavelength was the same as for Kelvin-Helmholtz vortices. In the image at  $t = t_0 + 7.5$  s of this experiment too, some transverse vortices can be seen clearly.

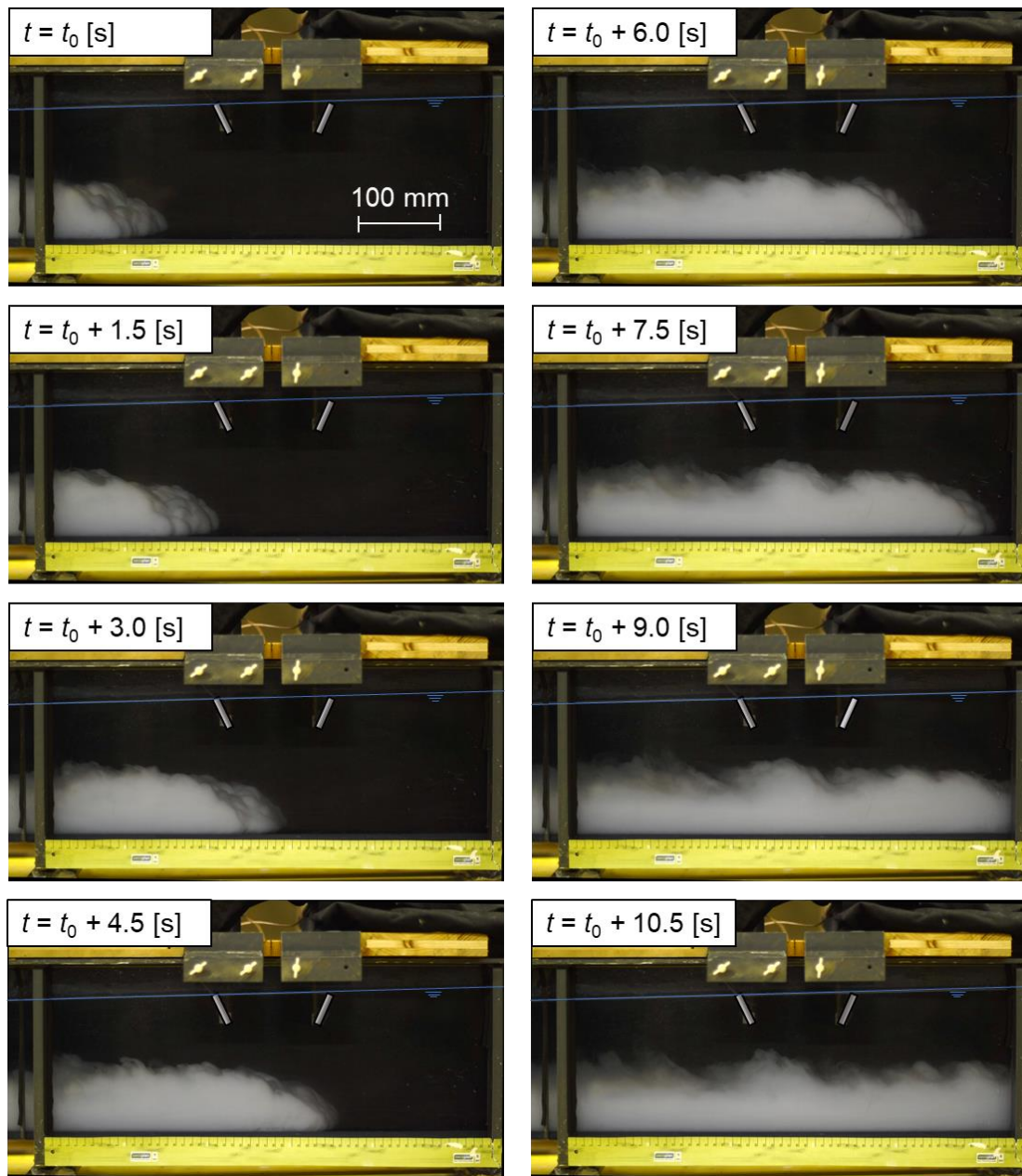


**Fig. 3-9** Snapshots of quartz-suspended turbidity currents of Case 1 from  $t = t_0$  to  $t_0 + 10.5$  s

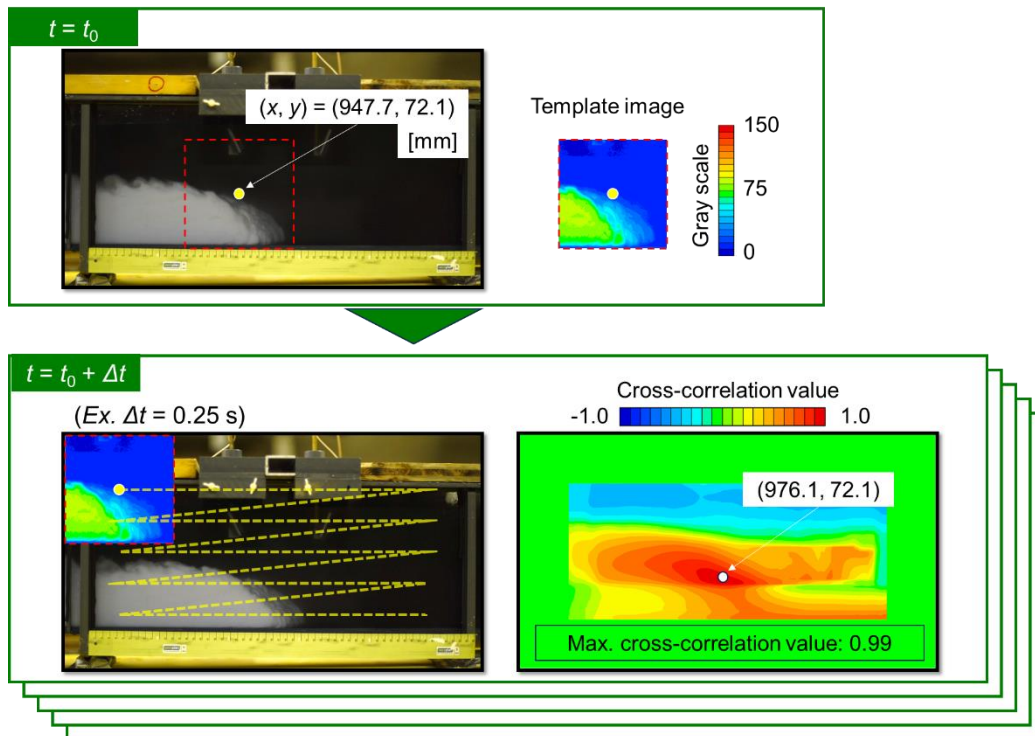


**Fig. 3-10** Schematic diagram of pattern matching method

In order to measure the front velocity  $U_f$  which is the advection speed of the head region of gravity currents, pattern matching method is applied to the successive experimental images. The schematic diagram of the pattern matching method is shown in Fig. 3-10. Firstly, a template image with  $451 \times 451$  pixels was prepared from the image at  $t = t_0$ , where  $t_0$  is a variable arbitrary elapsed time for each experimental case. Because the values of  $U_f$  are different from each experiment depending on the initial conditions, it is difficult to use a constant value as  $t_0$ . In addition, it was also confirmed that the obtained result of  $U_f$  hardly depended on how to choose  $t_0$ . In this study, therefore, the smallest value among the elapsed times of the image showing sufficient flow structures of the head region to make the template image with more than  $451 \times 451$  pixels was used as  $t_0$  in each experiment. For every five images (every 250 ms), the cross-correlation value at each pixel was calculated, and just one pixel with the maximum cross-correlation value was defined as the head position of the current at that time. This operation was applied to the results of the experiments from Case 1–25. The results are shown in Fig. 3-11. In this graph, horizontal axis indicates the elapsed time ( $\Delta t$ ) from  $t = t_0$  and vertical axis indicates the displacement of the computed head position from the initial position at  $t = t_0$ . The results of quartz-suspended turbidity currents with  $1008 \text{ kg/m}^3$  in bulk density are summarized in Fig. 3-11(a). As you can see, a similar trend is confirmed in all experimental Cases 1–8, because the initial conditions are the same in these cases. Those results roughly ensure the reproducibility of the currents in this experimental facility. In Fig. 3-11(b), the symbols of square, diamond, and triangle



indicate the results of quartz-suspended currents, saline density currents, and opalin-suspended currents, respectively. Additionally, the results of the two-layer turbidity currents in the Case 19–25 are shown in Fig. 3-11(c) by cross marks. As you can guess, in the two-layer turbidity currents, the variation of the gray scale values is larger than that of the one-layer turbidity currents, because two kinds layers showing different color from each other are mixed. Hence, in the cases of two-layer currents, it is confirmed that the variations in the head position detected by the pattern matching are slightly larger than in the cases of one-layer currents.

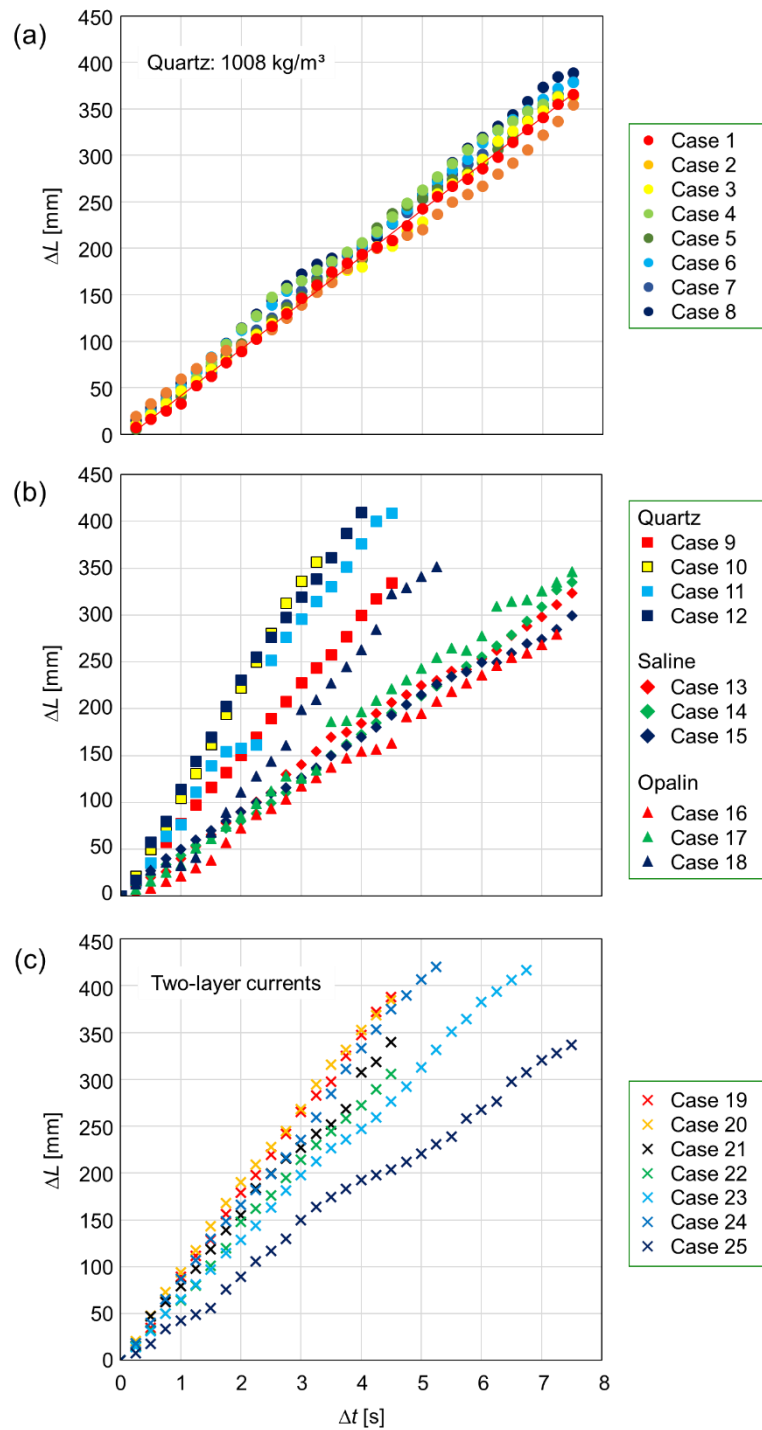


**Fig. 3-11** Time variation of the head position of the gravity currents, (a) quartz-laden currents with  $\rho_H = 1008 \text{ kg/m}^3$ , (b) the remaining cases of the one-layer currents (quartz, saline, and opalin currents), and (c) two-layer currents

In all cases, the displacement of the head is increasing in almost direct proportion to the  $\Delta t$

due to the lock-exchange experiments with high-volume release, that means the sufficient driving force keeps supplied by the density difference between the heavier fluids and the ambient fluid. Therefore, the currents propagate with almost constant front velocity  $U_f$  without decay in these experimental time ranges. Using this characteristic, the front velocity of each experimental case was calculated from the slope of a regression line estimated by the least-squared method, and the result is shown in Fig. 3-12. In this graph, the vertical axis denotes the calculated front velocity  $U_f$  and the horizontal axis denotes the initial bulk density of heavier fluids ( $\rho_H$ ). In case of two-layer currents, the density is calculated with considering the volume difference between the tank A and the tank B. The corresponding values are 1023 kg/m<sup>3</sup> in Case 19–22, 1012 kg/m<sup>3</sup> in Case 23 and 24, and 1019 kg/m<sup>3</sup> in Case 24. The symbol indicating each case is the same to that used in Fig. 3-11. In the past studies about saline density currents, the dimensionless velocity ( $U_f^*$ ) for lock-exchange method have been used to summarize the values of  $U_f$ , and it is defined as

$$U_f^* = \frac{U_f}{\sqrt{g'H}}, \quad (3-22)$$

where  $H$  is total fluid depth and  $g'$  is reduced gravitational acceleration defined as

$$g' = \frac{\rho_H - \rho_W}{\rho_W} g. \quad (3-23)$$

In this study, however, the flume was inclined at 1.38° and the fluid depth varies with the distance from the gate. Here, the calculation was carried out using the fluid depth of  $H = 179$  mm at  $x = x_l$  as the representative depth. Some values of  $U_f^*$  are reported in the previous studies about lock-exchange density currents, as 0.44 (Middlen, 1966), 0.46 (Keulegan, 1957; Barr, 1967), and 0.41 (Kneller *et al.*, 1999). Therefore, the front velocity can be estimated using Eq.( 3-22 ) from each initial density of heavier fluids. In Fig. 3-12, the estimated front velocity is plotted by solid lines, the upper one is the estimated velocity in case of  $U_f^* = 0.46$  and the lower is in case of  $U_f^* = 0.41$ . The values of experimental  $U_f$  and estimated by  $U_f^*$  have good agreement just in cases of quartz-suspended currents and some two-layer currents of experimental Cases 19, 20, 23, and 24, where the lower fluids contain the quartz particles. Contrary to that, the saline density currents show a little bit lower values of  $U_f$ , that may be affected by the inclined experimental flume as a result of the balance between downward force of heavier fluid and upward force of counter flow by ambient fluid. Notable points are shown in the remaining experimental cases of opalin-suspended currents and two-layer currents whose lower layer contains opalin particles of the experimental Cases 21, 22, and 25. In those cases, the values of  $U_f$  are obviously lower than estimated values. These results suggest that the value of  $U_f$  cannot be estimated only by initial density of heavier fluids and depth, that seems to be attributed to the difference of rheological property between opalin-suspended fluids and quartz-suspended fluids. The details about it will be discussed later.

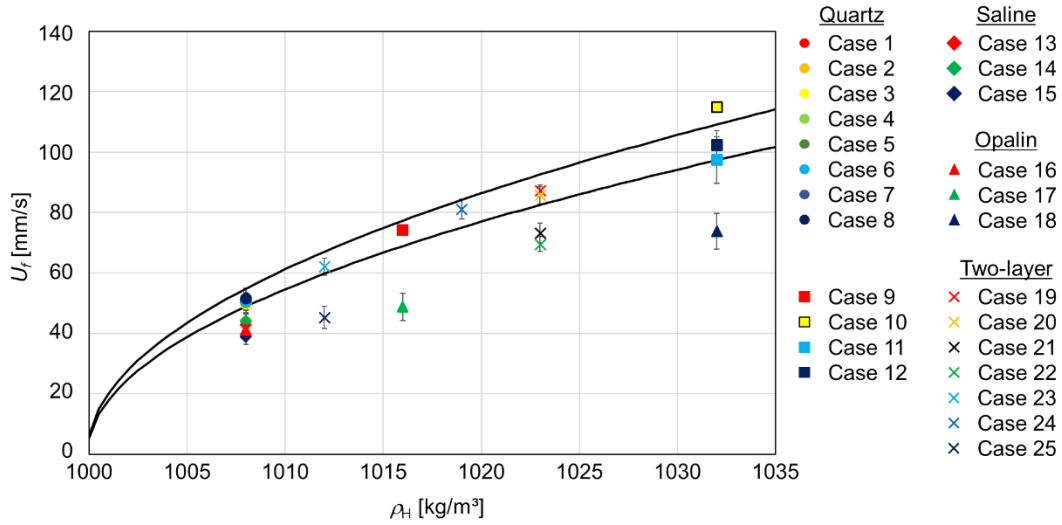


**Fig. 3-12 Measured front velocity in experimental Case 1–25**

The spatio-temporal velocity distributions of the experimental Case 3 obtained from UVP are shown in Fig. 3-13, those distributions were measured at (a)  $x = 500$ , (b) 1000, and (c) 1500 mm, respectively. The axes denote the height from the bed ( $y$ ) and the elapsed time from the release of the gate 1 ( $t$ ). In the arrangement of transducers II, the velocity components along the propagation line of ultrasonic wave ( $u_\xi$ ) are obtained. The magnitude of  $u_\xi$  is shown as color contour. Comparing these three distributions, the head of the current can be observed clearly at the measurement line  $x = 1000$  (b) and 1500 mm (c), but it cannot be done at  $x = 500$  mm (a). Therefore, it is assumed that the current was developing between  $x = 500$  to 1000 mm and reached stationary state before  $x = 1000$  mm in this case. Here, in order to confirm the characteristic of  $U_f$ , the estimated arrival time  $t^*$  is defined as

$$t_{x=l}^* = \frac{l}{U_f}, \quad (3-24)$$

where,  $l$  is an arbitrary distance from the gate 1. The value of  $t_{x=l}^*$  represents the expected time of arrival at each measurement line, assuming that the front velocity  $U_f$  calculated above will be constant even if it reaches each measurement point. Each value of  $t_{x=l}^*$  at  $x = 500$ , 1000, and 1500 mm is shown in Fig. 3-13 as dotted line. From those results, it is confirmed that the turbidity current roughly reaches each measurement line at the estimated arrival time calculated from  $U_f$ . In this study, therefore, the calculated front velocity  $U_f$  in each experimental case can be treated as constant value below.

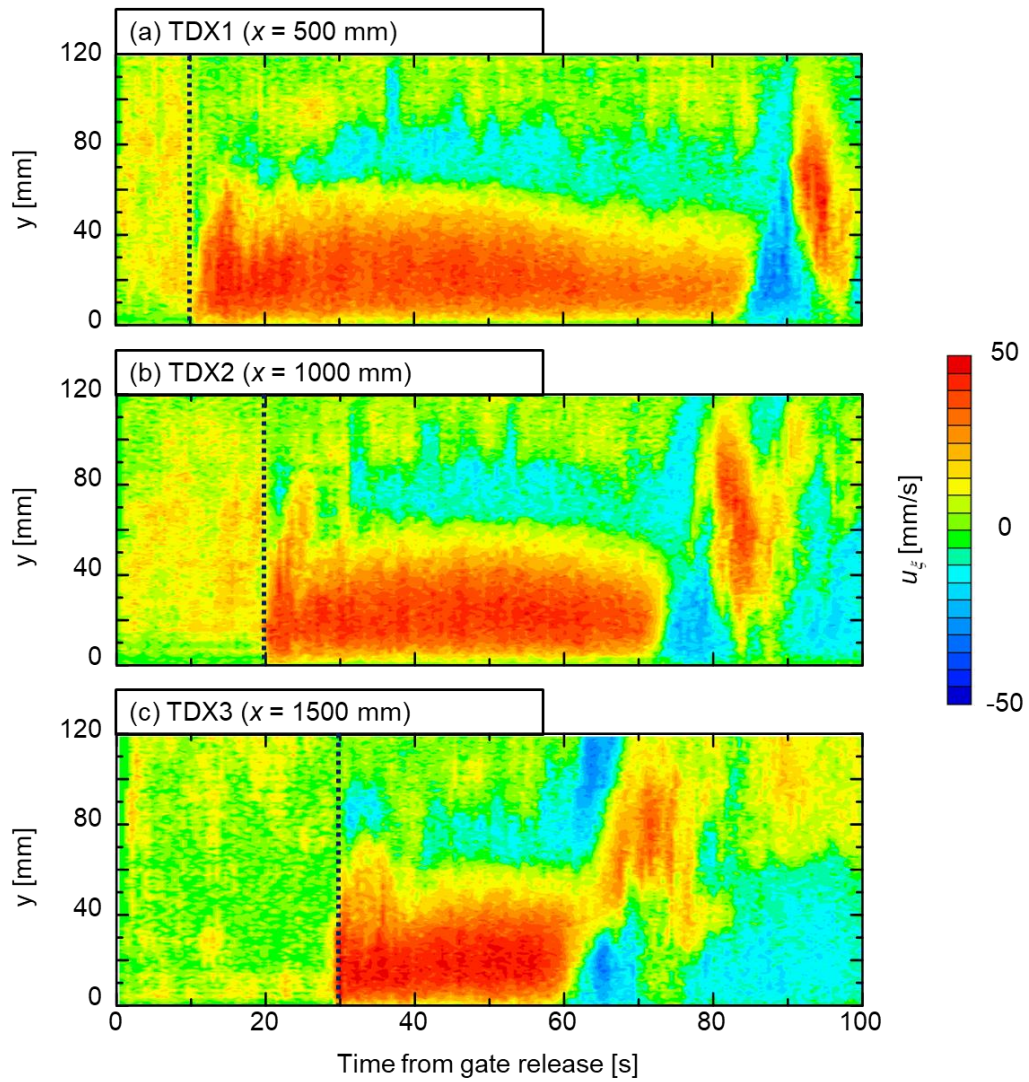


**Fig. 3-13** Spatio-temporal velocity distributions measured at (a)  $x = 500$ , (b)  $x = 1000$ , and (c)  $x = 1500$  mm of experimental Case 3

## 4. Results and discussions

### 4.1. Comparison of flow structures between quartz-suspended currents and saline density currents

In this section, the differences of flow characteristics between quartz-suspended turbidity currents of Case 1–8 and saline density currents of Case 13–15 are discussed. The main driving force of the currents of this experimental facility is density difference between heavier fluids and ambient fluid, and all of the initial densities of heavier fluids discussed in this section are the same value of  $\rho_H = 1008 \text{ kg/m}^3$ . In other words, it is the main target of this section to investigate how the flow behavior of gravity currents vary with the presence or absence of quartz particles and to compare flow structures for the elucidation of the long-range propagation mechanism of the turbidity currents.

#### 4.1.1. Inner velocity structures of the currents

Spatio-temporal distributions of horizontal and vertical velocity components ( $u$  and  $v$ ) obtained by two-UVP measurement are shown in Fig. 4-1, where (a) left and (b) right panels are from Case 1 (turbidity current) and Case 13 (density current). The axes denote the height from the bed ( $y$ ) and the elapsed time from the release of the gate 1 ( $t$ ). The V-shaped distributions seen in these graphs are the ultrasonic interference noise caused by the simultaneous measurement of the two UVPs. As the color scale corresponding to the velocity magnitude, horizontal velocity component  $u$  is dominant in the flow. Because lock-exchange flume is a closed system, counter flows of ambient fluid occur at the upper boundary of the currents. In the distributions of  $u$ , the increase and decrease of velocity due to the propagation of the currents are confirmed. Regarding the distribution of  $v$ , in spite of small velocity magnitude, strong rolling-up structure is observed near the head position in the turbidity current ( $20 < t < 25 \text{ s}$ ). Some pair of positive and negative values in  $v$  distributions near the upper boundary can indicate the existence of vortices attributed to Kelvin-Helmholtz (K-H) instability.

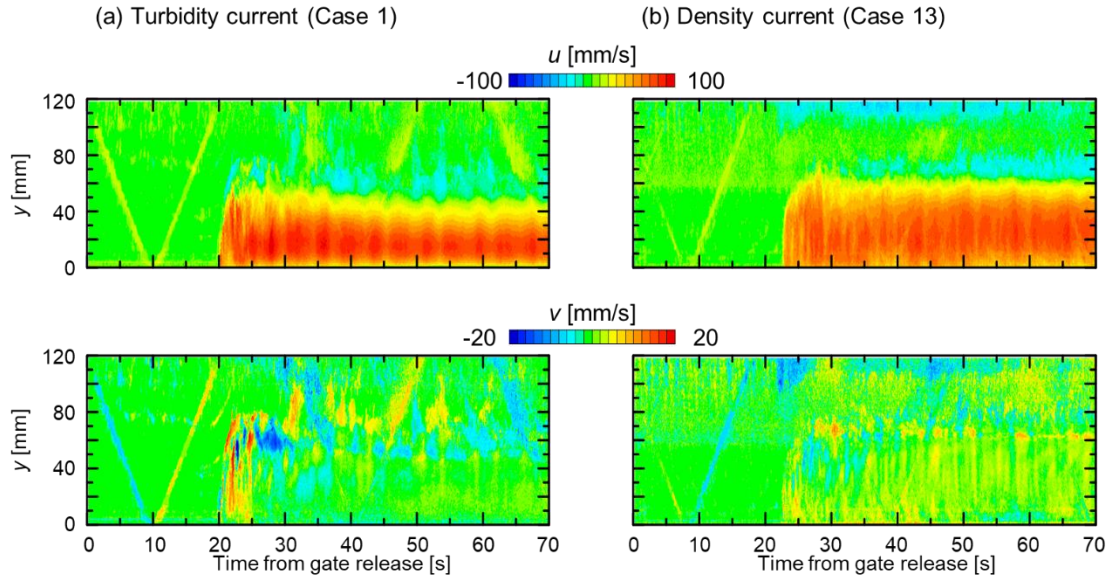


**Fig. 4-1** Spatio-temporal distributions of horizontal (above) and vertical velocity component (below): (a) Case 1 (turbidity current) and (b) Case 13 (density current)

#### 4.1.2. Time variation of the height and velocity of the currents

The timeline images made from snapshots are shown in Fig. 4-2, where (a) left and (b) right panels are from Case 1 (turbidity current) and Case 13 (density current) extracted at  $x_l = 1005$  mm (corresponding to the cross point of two ultrasonic measurement lines). In the front region of the turbidity current at the time about  $20 \text{ s} < t < 30 \text{ s}$ , the edge of the head region can be observed clearly and the height of the current is larger than that in the body. Comparing with the image of turbidity current, the rolling-up structure at the head and shear waves observed in the body region seem to be smaller in case of the density current. In order to quantify the height of the two currents mentioned above, integral scale method (Ellison and Turner, 1959) is applied. Combining this method with  $u$  distributions obtained by UVP, the representative flow layer thickness  $h$  and layer-averaged velocity  $U$  can be calculated at each time, every 50 ms along the equations,

$$Uh = \int_0^{h_t} u(y) dy, \quad (4-1)$$

$$U^2 h = \int_0^{h_t} u(y)^2 dy, \quad (4-2)$$

where,  $h_t$  is the height at which  $u(h_t) = 0$  near the upper boundary. Here, the spatio-temporal velocity distributions obtained by UVP contain measurement noises. To reduce the influence of the noises, median filter with  $9 \times 9$  measurement points was performed for the spatio-temporal distributions. The time variations of  $h$  and  $U$  for case 1 and case 13 are shown in Fig. 4-3, where top panels show profiles

of the  $h_t$  (black square) and  $h$  (green dot). In the case 1, the obvious edge of the head cannot be observed in comparison with the timeline image, which means that both values of  $h_t$  and  $h$  take the values of around  $y = 60$  mm, although the height of the head region seems to reach  $y \approx 90$  mm in the timeline image. This result suggests that the complicated flow structure in the head region containing not only  $u$  but also relatively large magnitude of  $v$  component causes the underestimation of the flow thickness. From these two distributions of the flow layer thicknesses, it is confirmed that the turbidity current is thinner than the density current in whole region including the heads. The bottom panels in Fig. 4-3 show profiles of the layer-averaged velocity  $U$  (black diamond) and front velocity  $U_f$  (green dot line) as the reference value. In the vicinity of the front position, the magnitudes of  $U$  almost agree with  $U_f$ . On the other hand, the profiles of  $U$  always have larger values than  $U_f$  in the body region. These results suggest that in the two kinds of gravity currents the momentum is supplied from the wake flows, namely, the momentum is transported from the body region to the head region.

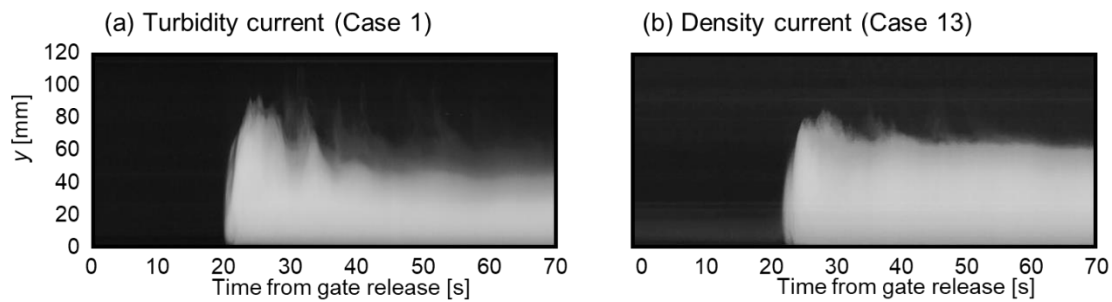


**Fig. 4-2** Timeline image at the cross-point of two ultrasonic beams emitted from the transducers: (a) Case 1 (turbidity current) and (b) Case 8 (density current).

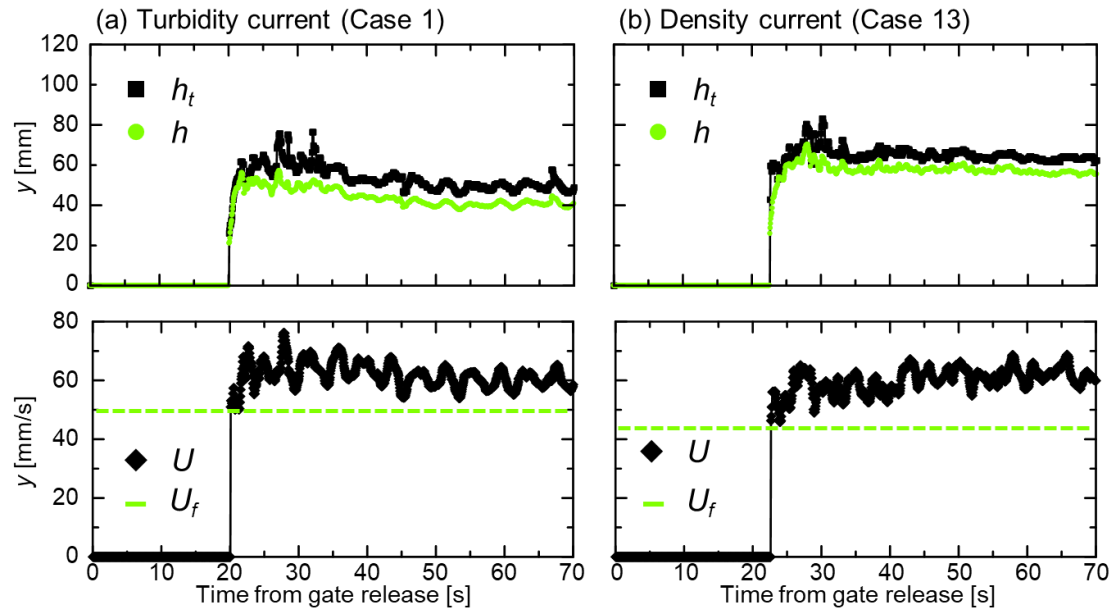


**Fig. 4.3** Time variation of  $h$  and  $U$  calculated by the integral scale method of (a) Case 1 and (b) Case 13

#### 4.1.3. Flow structures in the body region

In this section, the flow structures of the body, which can be treated as quasi-steady flow (Kneller and Buckee, 2000), is focused on.

The profiles of the time-averaged  $u$  of Case 1 and Case 13 are shown in Fig. 4-4, with the averaging window of  $t = 35$  to  $70$  s. There is no clear definition to separate the head and the body in the gravity currents. With judging from the  $h$  distributions from the integral scale method,  $t = 35$  s was used as a separation point in this study, which means the height becomes lower than the head region after  $t \approx 35$  s. As mentioned in the discussion about integral scale, these two graphs indicate that the first zero-crossing point on  $y$  ( $h_t$ ), corresponding to the thickness of the currents, is smaller in the turbidity current than in the density current (in some previous studies, there are other definition of the thickness). Several time-averaged properties to describe the rough flow structures are shown in Table 4-1, where the overline ( $\bar{\quad}$ ) means the time-averaged value from  $t = 35$  to  $70$  s. In the Case 1, the velocity  $u$  reaches the maximum at  $y = h_m = 14.6$  mm and the corresponding velocity is  $u_{\max} = 79.2$  mm/s, and  $h_m = 25.4$  mm and  $u_{\max} = 73.2$  mm/s in the Case 13. In case of particle-laden flows like turbidity currents, the density of suspended particles is larger than that of water normally, so the force direction works downward. Contrary to that, in the saline density currents, diffusion caused by the density difference is predominant, so the force direction is upward, that is opposite direction against the case of turbidity currents.

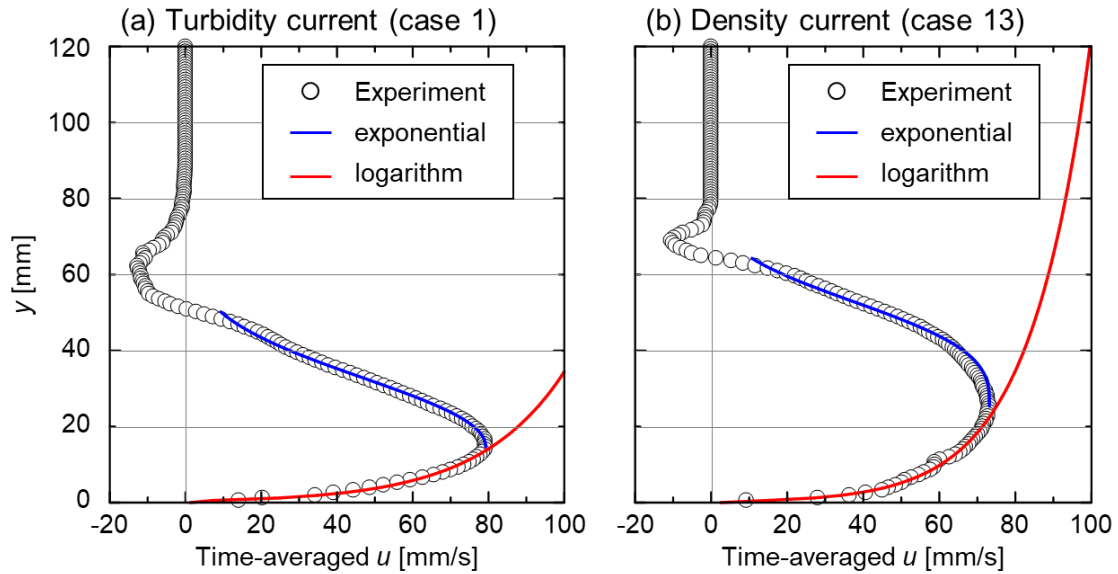


**Fig. 4-4** Distributions of time-averaged horizontal velocity component  $u$  in the body region from  $t = 35$  to  $70$  s for (a) Case 1 (turbidity current) and (b) Case 13 (density current), where red lines are the result of logarithmic fitting at  $0 < y < h_m$  and blue lines are the result of exponential fitting at  $h_m < y < h_t$

Previous researches reported that the  $u$  distributions of turbidity currents have a shape similar to a wall jet, where two regions are distinguished, namely, a wall region ( $y < h_m$ ) and a jet region ( $h_m < y < h_t$ ). [Altınakar et al. \(1996\)](#) suggested the fitting method to the  $u$  distributions in the body for two regions. The fitting procedures are shown below.

- i) In the wall region,  $y < h_m$ , by a logarithmic relation,

$$u(y) = \frac{u^*}{\kappa} \ln \frac{y}{y_0}, \quad (4-3)$$

This equation is “law of the wall (e.g. [Kida and Yanase, 1999 \(in Japanese\)](#))” that predicts a logarithmic velocity profile in inner layer ( $y < h_m$ ), and the variables are  $u^*$  and  $y_0$  which are friction velocity and zero-velocity roughness height, respectively. In this study, assuming a smooth bed, the value of 0.41 is substituted into the von Karman constant  $\kappa$  (e.g. [Zordan et al., 2018](#)). The calculated  $u^*$  and  $y_0$  are shown in [Table 4-1](#). The fitting result based on this method is shown in [Fig. 4-5](#), where the  $y$  axis denotes the semilogarithmic axis. The profiles of time-averaged horizontal velocity component  $u$  in the body region show a roughly linear distribution in a semilogarithmic graph at  $y < h_m$  and the fitting result closely matches that. Besides, it is the big advantage of UVP that the measurement with high spatial resolution of  $\Delta y = 0.67$  mm can be performed in this case.

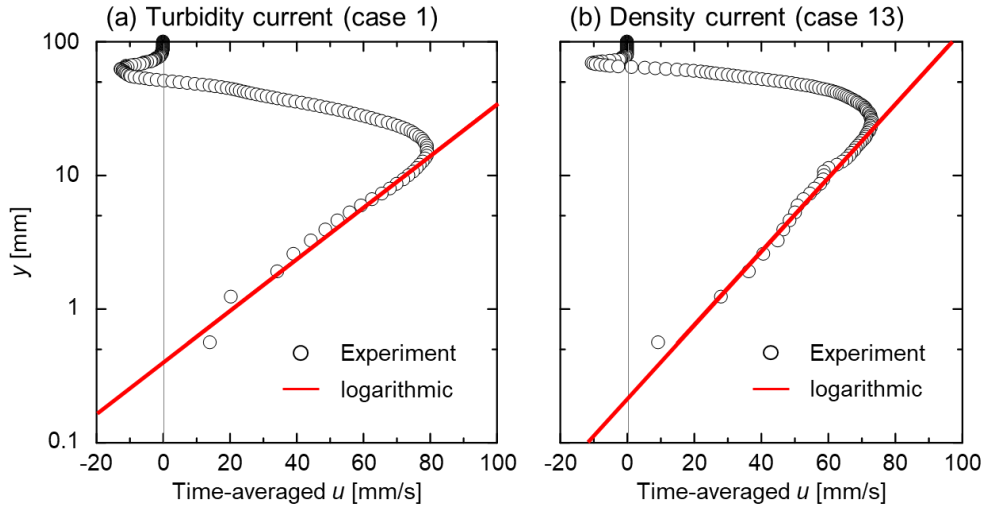


**Fig. 4-5** Fitting results of the wall region at  $y < h_m$  for (a) Case 1 (turbidity current) and (b) Case 13 (density current)

ii) In the jet region,  $y > h_m$ , by a near-Gaussian relation,

$$u(y) = u_{\max} \exp \left[ -\alpha_c \left( \frac{y - h_m}{h - h_m} \right)^m \right]. \quad (4.4)$$

This relation is fitted to the velocity profiles measured in the jet region namely outer region of the currents. The variables are  $m$  and  $\alpha_c$ , and fitting results are shown in Table 4-2. The values of fitting variables in the Case 1 show good agreement with the values in the previous study (Altinakar *et al.*, 1996). The fitting curve obtained from the variables are also shown in Fig. 4-4 by blue solid line. The values of  $m$  and  $\alpha_c$  in the present study of the Case 1 coincide with the results of their research which used the same quartz particles.

Using calculated  $u^*$  in the wall region, the shear stress working near the bed  $\tau_W$  can be estimated based on the definition of friction velocity as,

$$u^* = \sqrt{\frac{\tau_W}{\rho_H}}. \quad (4.5)$$

As the result of the estimation assuming logarithmic profiles, the wall shear stresses near the bed are 0.086 Pa in Case 1 and 0.042 Pa in Case 13. It means that the turbidity current can propagate faster than the density current, in spite of the larger wall shear stress acting near the bed.

**Table 4-1** Time-averaged representative values to dictate the flow patterns in body of gravity current

	Turbidity currents (Case 1)	Density currents (Case 13)
Zero-velocity height, $\bar{h}_i$ [mm]	50.7	64.4
Flow layer thickness, $\bar{h}$ [mm]	41.6	57.2
Layer-averaged velocity, $\bar{U}$ [mm/s]	61.2	61.0
Maximum horizontal velocity, $u_{\max}$ [mm/s]	79.2	73.2
Velocity maximum height, $h_m$ [mm]	14.6	25.4
Friction velocity, $u^*$ [mm/s]	9.23	6.48
Wall friction length, $y_0$ [mm]	0.404	0.220

**Table 4-2** Fitting variable for the jet region

	Turbidity currents (Case 1)	Density currents (Case 13)
$\alpha_c$	1.20	1.05
m	2.10	3.03

#### 4.1.4. Comparison of fluctuation components in the body region

In this section, the fluctuation components of the velocity as turbulent flows in the body region of the currents are focused on. Taishi *et al.* (2002) suggested the method to obtain fluctuation components and Reynolds stress using two measurement lines (like the arrangement of I in this study). Using that concept, the root mean square values of the fluctuation components are calculated along following equation,

$$u'_{\text{RMS}} = \sqrt{u'^2} = \sqrt{\frac{u_1'^2 - 2u_1'u_2' + u_2'^2}{4\sin^2\theta}}, \quad (4-6)$$

$$v'_{\text{RMS}} = \sqrt{v'^2} = \sqrt{\frac{u_1'^2 + 2u_1'u_2' + u_2'^2}{4\cos^2\theta}}, \quad (4-7)$$

where, the averaging window of  $t = 35$  to  $70$  s in this case too. The vertical distributions of the calculated those values are shown in Fig. 4-6. The distributions have notable characteristics. Firstly,  $u'_{\text{RMS}}$  value is larger than  $v'_{\text{RMS}}$  globally in both cases, and they take local maximum value at  $y = h_i$ . Besides, in the upper region  $y \gtrsim h_i$ , both values of  $u'_{\text{RMS}}$  and  $v'_{\text{RMS}}$  become larger than the lower region, because the interactions with ambient fluid, which include K-H instability mentioned above, attributed to the density or flow velocity differences occurs in the upper boundary. Such the interactions vary with space and time even in the body region treated as quasi-steady flow, which works to amplify the

$u'_{\text{RMS}}$  and  $v'_{\text{RMS}}$ . The outstanding point is vicinity of the bed (in the inner region:  $y < h_m$ ). In this region, the tendencies of  $u'_{\text{RMS}}$  and  $v'_{\text{RMS}}$  distributions are obviously different each other case, that is to say, both values in the turbidity current are smaller than in the density current. From these results, it is predicted that the existence of quartz particles suppresses the flow fluctuations in the inner region of the turbidity current  $y < h_m$ . In the distribution of the turbidity current, moreover, the values of  $u'_{\text{RMS}}$  are getting larger dramatically from  $y \gtrsim h_m$ . In fact, this positive peak in the  $u'_{\text{RMS}}$  distribution is also confirmed in the distribution of the density current at  $y \approx 50$  mm, but the spatial size and the magnitude are much smaller than in the case of the turbidity current.

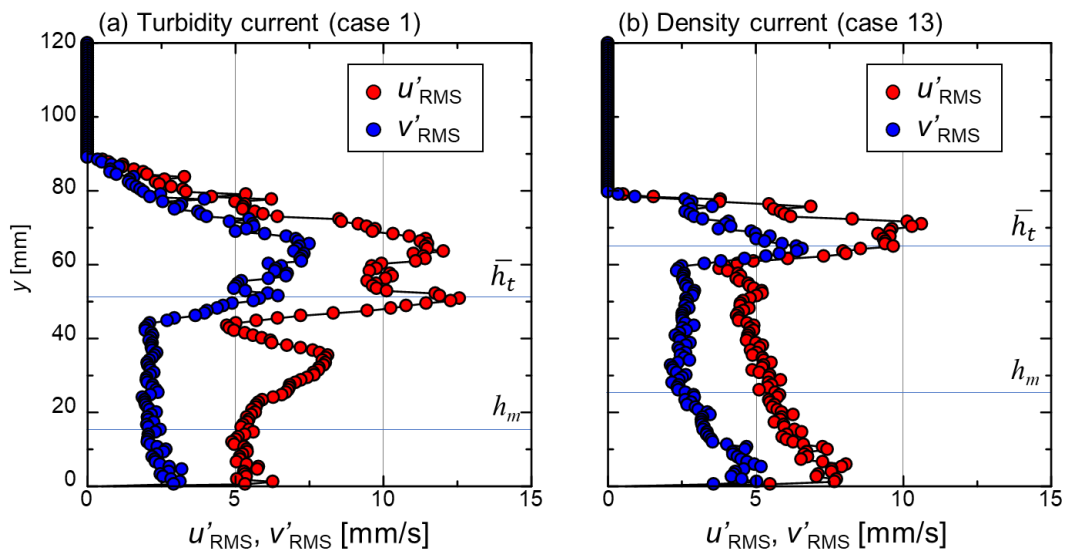


**Fig. 4-6** Vertical profiles of the root mean square values of fluctuation components for (a) Case 1 (turbidity current) and (b) Case 13 (density current)

#### 4.1.5. Summary of the difference of flow structures between the turbidity currents and the density currents

This part summarizes the comparison results of the flow behaviors between the quartz-suspended turbidity current and the saline density currents. A simple comparison table of some physical properties that determine flow structures of represent both currents is shown in Table 4-3, where only the magnitude relation of the respective values is represented by the size of circles  $\circ$ . As shown in the table, the most essential difference of both currents occurs at the front velocity  $U_f$ . Using image processing, it was revealed that the  $U_f$  values of the turbidity currents in eight cases are greater on average 19.0% than the density currents in three cases. Therefore, the comparison of inner flow structures of those currents was conducted using ultrasonic techniques.

**Table 4-3 Measured physical properties determining the flow behaviors**

	Turbidity currents (Case 1)		Density currents (Case 13)
Front velocity, $U_f$ [mm/s]	○	>	○
Max. velocity, $u_{\max}$ [mm/s]	○	>	○
Height taking $u_{\max}$ , $h_m$ [mm]	○	<	○
Height of the current, $h$ [mm]	○	<	○
Friction coefficient, $C_f$ [-]	○	>	○

The time-averaged profiles of horizontal velocity component  $u$  in the body region show that in the case of the turbidity current, not only the  $U_f$ , but also the maximum velocity  $u_{\max}$  in that region is greater than the density current. On the other hand, the height  $h_m$  that takes the maximum velocity is smaller in case of the turbidity current than the density current. Using these profiles, the shear stress  $\tau_w = \rho u^{*2}$  working near the bed can be estimated based on a definition of the friction velocity  $u^*$  obtained from the low of the wall, and the friction coefficient  $C_f$  is defined as

$$C_f = \frac{\tau_w}{\frac{1}{2}\rho u^2}, \quad (4-8)$$

where,  $\rho$  shows the bulk density of the fluid, so  $\rho_H$  should be used in the present case. Here, considering the definition of  $\tau_w$ , the term of  $\rho$  is canceled out, and finally it is written as

$$C_f = 2\left(\frac{u^*}{u}\right)^2. \quad (4-9)$$

The horizontal velocity component should be substituted for  $u$  in the equation, but there is room for discussion as to which value is actually used such as  $U_f$ ,  $u_{\max}$ , and time-averaged  $U$ . The calculated  $C_f$  values using each horizontal velocity value are summarized in Table 4-4. In all cases, the  $C_f$  values in case of the turbidity current is larger than the density current.

**Table 4-4 Friction coefficient using each  $u$  value**

	Turbidity current (Case 1)	Density current (Case 13)
$C_f$ based on $U_f$ [-]	0.068	0.046
$C_f$ based on $u_{\max}$ [-]	0.027	0.016
$C_f$ based on time-averaged $U$ [-]	0.045	0.023

The UVP measurement made it possible to obtain the representative flow layer thickness  $h$  and layer-averaged flow velocity  $U$  at each measurement time (every 50 ms in this study) using the integral scale method (Ellison and Turner, 1959), which can show the time variation of the  $h$  and  $U$ . In the body region of the currents, the  $h$  value, which roughly corresponds the height of the current, is smaller in the turbidity current than the density current.

Considering those results, the estimated flow structures of both the currents are described in Fig. 4-7. In case of the density current, the diffusion of the saline heavier fluids may be dominant factor to form the shape of the currents due to the density difference with ambient fluid. Such a diffusion working upward direction in the body region may cause the enlargement of the density currents. As a result, the height, where the horizontal velocity takes maximum value, seems to become larger than the turbidity currents. Contrary to the case of density currents, the suspended particles within the turbidity currents have a heavier density than water as the ambient fluid in many cases, here the specific density of quartz particles used in this study is 2.65. Therefore, in the turbidity currents, not only diffusion of the particle-suspended fluids but also the settling of that particles occurs. It is considered that the height of the turbidity currents may be suppressed due to such the settling effect of the particles. From the vertical distributions of the root mean square values of velocity fluctuation components shown in Fig. 4-6, it was confirmed that the magnitude and the position of the positive peak of the  $u'_{\text{RMS}}$  values are different from each case. Comparing the  $u'_{\text{RMS}}$  distributions, the peak near the upper boundary can be observed in the both cases, but there are clear differences in the way the distribution at  $y < h_t$ . In case of the density current,  $u'_{\text{RMS}}$  distribution takes larger values as going downward in this region. On the other hand, in case on the turbidity current, the magnitude of the  $u'_{\text{RMS}}$  shows large values in the range of  $h_m < y < h_t$  (outer region). From these results, it is predicted that the existence of the suspended particles would suppress the fluctuation effect near the bed. In addition, the interactions of particle–particle and particle–fluid are also caused, and it would work as a mixing effect for suspended particles, which suppress the settling of the particles. In the results of such a mixing effect, suspended particles can be re-supplied to near upper boundary, which generates the additional driving force, because the risen heavier particles get the potential energy again. Such a series of the processes may become a key factor to explain the reason why the turbidity currents can propagate faster than the density currents in spite of that the friction coefficient  $C_f$  of the turbidity current is larger than the density current.

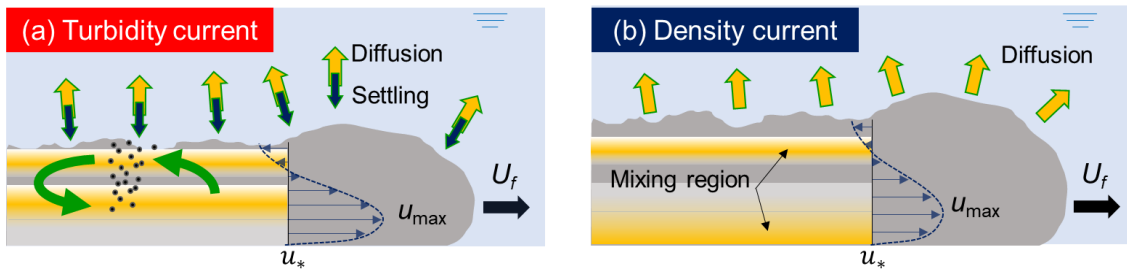


**Fig. 4-7** Estimated flow structures in (a) turbidity currents and (b) density currents

#### 4.2. Inner flow structures of turbidity currents as solid–liquid two–phase flow

Firstly, the experimental images of the front motion at each elapsed time from the gate 1 release are shown in Fig. 4-8, where the current of the Case 1, which was composed of the water containing quartz particles with 0.5% in volume fraction, is focused on. These images were taken from the front of the current by a digital camera (GoPro, Hero4), which was mounted on the right edge of the flume and completely submerged in the fluid. In the figures, the complicated flow structure can be observed in the head region. In particular, it is characteristic that some large flow structures are wound up from near the bed, and the structures gradually becomes smaller as they gradually wrap upward. Such a change in the flow structure resembles the theory of the turbulent energy cascade in which it sequentially propagates from large-scale vortices to small-scale vortices (Kida and Yanase, 1999 (in Japanese)). As you can see, however, the information obtained from the optical images cannot enough explain the long-distance propagation mechanism on turbidity currents due to their opacity.

In this section, therefore, the inner flow structures of the turbidity current as a solid–liquid two–phase flow are discussed using velocity and echo profiles obtained by UVP. The analysis was carried out using the experimental results of the quartz-laden turbidity current of Case 1 discussed in the last section.

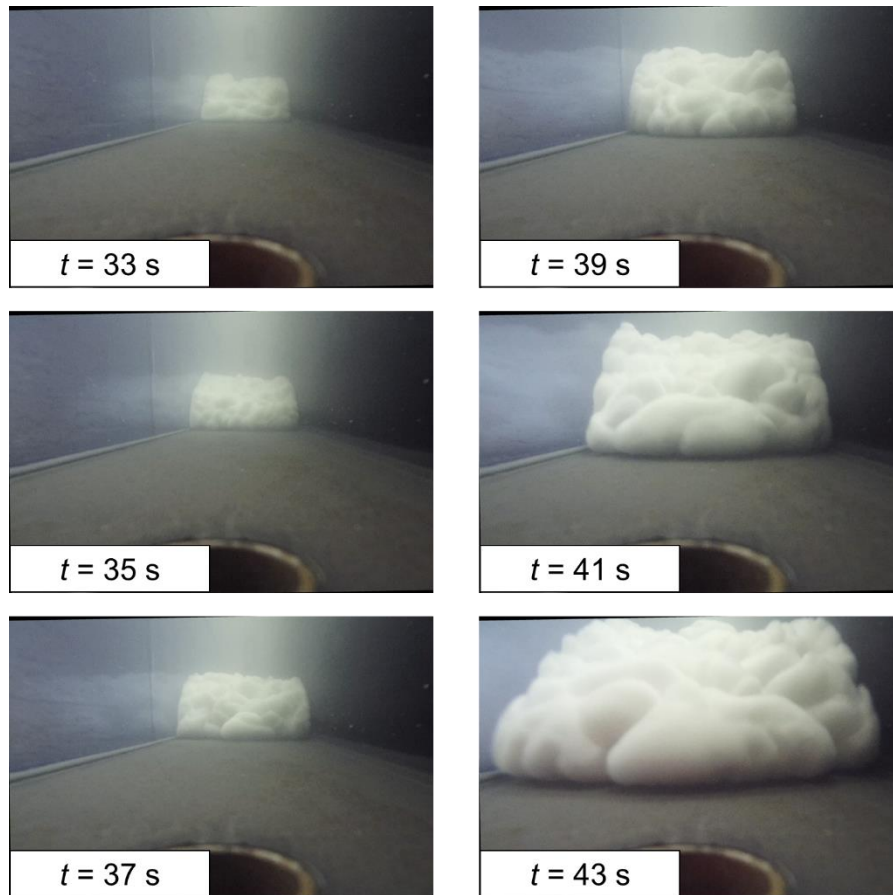


**Fig. 4-8** Snapshots of front motion at each elapsed time from the release of the gate 1 (turbidity current in the Case 1 containing quartz particles with 0.5% in volume fraction)

#### 4.2.1. Flow field of the current

The use of a pair of UVPs makes it possible to obtain both velocity components of horizontal ( $u$ ) and vertical  $v$ . Additionally, it was revealed that the currents propagate with almost constant front velocity  $U_f$  under the condition of high-volume release, which means that the amounts of the heavier fluid and the ambient fluid are almost same on the initial condition like this study. Therefore, although UVP measures velocity profiles at fixed line, it seems possible to reconstruct a flow field with space-space using Taylor's frozen fluid hypothesis. The concrete procedure is as follows.

Firstly, the front velocity  $U_f$  is calculated and the value is 49.9 mm/s in the Case 1. As shown in Fig. 4-1, the UVP measurement was continued for 70 s. Assuming that the turbidity current propagated at a constant front velocity  $U_f$  from the release of the gate 1, the head reaches about 3500 mm at  $t = 70$  s. Utilizing such a property, the converted travel distance  $X$  at  $t = 70$  s was calculated using the following definition,

$$X = U_f \left[ 70 - (t - t_{x=x_l}^*) \right], \quad (4-10)$$

where  $t^*$  indicates the estimated arrival time at  $x = x_l$  defined in the previous section. Because the velocity components could not be measured by a pair of UVP in the region  $t < t^*$ , it was modified in the elapsed time  $t$  in advance. Using the converted travel distance  $X$ , the spatio-temporal velocity distribution obtained by UVP can be treated as a spatio-spatio distribution. The obtained vector field combining the distributions of  $u$  and  $v$  component are shown in Fig. 4-9. In the figures, the height from the bed  $y$  and the converted travel distance  $X$  are used for the axis, and the flow structures obtained from the optical timeline image and the velocity distributions are shown in Fig. 4-9(a) and (b), respectively. Regarding the vector field, from the aspect of visibility, the decimated result using the averaged value of 10 profiles in the  $X$  direction and 5 profiles in the  $y$  direction is shown. Comparing these two figures, the head region showing higher interface between the current and the ambient fluid can be observed around  $300 < X < 3500$  mm. In addition, a large rotating structure can be observed around  $y = 60$  mm, which is expected to be caused by the shear with the ambient fluid. Paying attention to the body region, in the vector field, the fluctuating interfaces are also observed around  $y = 50$  mm, and the height roughly corresponds to the zero-velocity height  $h_t$  (as discussed in the last section, the time-averaged value in  $35 \text{ s} < t < 70 \text{ s}$  is 50.7 mm). The distributions of vorticity calculated from the vector field are shown in Fig. 4-9(c). Normally, the vorticity is represented by the spatial differential of the velocity components shown as

$$\omega_z = \frac{\partial v}{\partial x} - \frac{\partial u}{\partial y}. \quad (4-11)$$

It takes the discrete form

$$\omega_z = \frac{\Delta v}{\Delta x} - \frac{\Delta u}{\Delta y}. \quad (4-12)$$

In this study, for the discrete width  $\Delta x$  in the  $x$  direction, the following value  $\Delta X$  was used with  $U_f$

$$\Delta X = U_f \cdot \Delta t_{\text{UVP}}, \quad (4-13)$$

where  $\Delta t_{\text{UVP}}$  is the temporal resolution of UVP measurement and the value in this case was 50 ms, so the  $\Delta X$  denotes the value of 2.50 mm. As same to the discussion on vector distributions, in the vorticity distribution, relatively large positive values are observed near the interface. In the head region, the negative values also appear and that is caused by the complicated flow structures containing not only horizontal velocity  $u$  but also vertical velocity  $v$ . Contrary to that, in the body region, when viewed from the bottom, three layers are confirmed in the order of negative, positive, and positive. As mentioned above, the positive value near the upper boundary of the current appears as the result of the shear flow caused by the interaction with the ambient fluid. Besides, a pair of positive and negative values is estimated to be derived from distribution of the horizontal velocity  $u$ . That is, the second term in definition formula of vorticity  $\Delta u / \Delta y$  is dominant, because the vertical velocity  $v$  is almost

zero in a fully developed region like the body region. As evidenced by the comparison of the vorticity and horizontal velocity distributions, the height  $h_m$ , where  $u$  takes maximum value, corresponds closely to the height where the vorticity value takes zero.

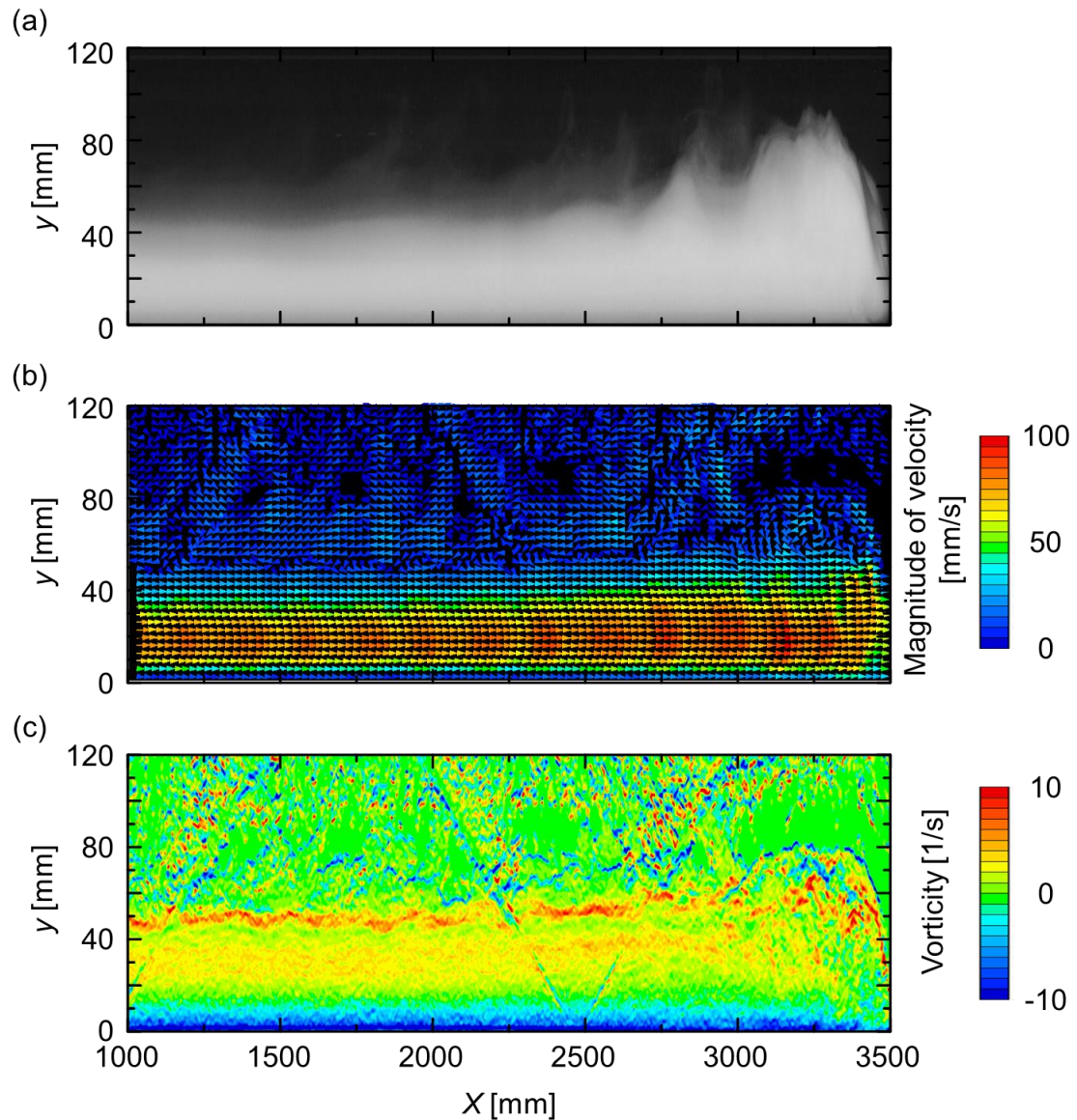


**Fig. 4-9** Flow structures assuming constant front velocity  $U_f$  obtained from (a) optical timeline image and (b) spatio-temporal velocity distributions, and (c) shows the vorticity distribution

#### 4.2.2. Concentration profile

As discussed above, concentration profiles of the quartz particles can be obtained using echo information. The spatio-temporal echo distribution obtained from UVP is shown Fig. 4-10. As you can

see in the figure, the echo intensity is a specific output value depending on the UVP devices and it fluctuates dramatically around a certain value. The distribution was obtained by subtracting the overall average value from each echo intensity. The head region shows relatively larger fluctuations in comparison with the body region. The mean-square amplitude of echo signal  $\langle V^2 \rangle$  is required to obtain the concentration profiles, the schematic image of the procedure is shown in Fig. 4-11.

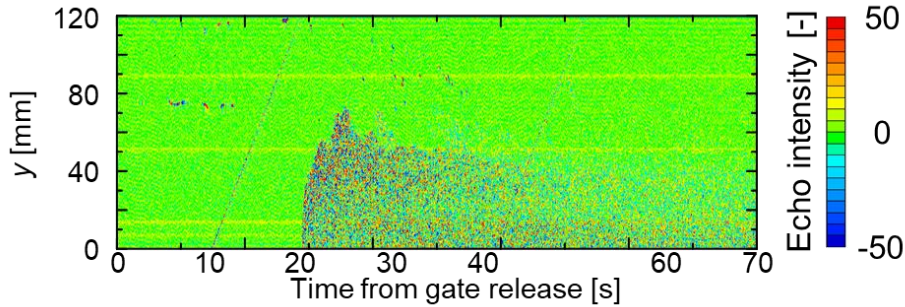


**Fig. 4-10** Spatio-temporal echo distribution obtained by UVP

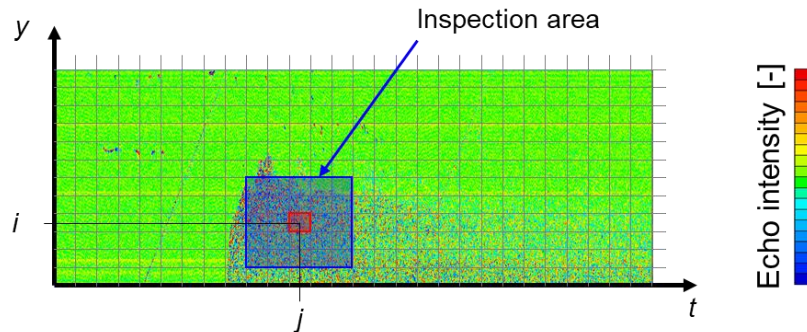


**Fig. 4-11** Schematic image of the procedure to obtain average amplitude values  $\langle V^2 \rangle$

Since the pixel noise is contained in the echo distribution, in this study, the averaged amplitude values by means of  $5 \times 5$  measurement points were used for the calculation of  $\langle V^2 \rangle$ , and the expression is as follows

$$\langle V^2 \rangle_{i,j} = \frac{1}{25} \sum_{\Delta i=-2}^2 \sum_{\Delta j=-2}^2 [ |V(i+\Delta i, j+\Delta j)| ]. \quad (4-14)$$

where  $i$  and  $j$  represent the coordinates in the time direction and the spatial direction of the measurement points, respectively. Using the value of  $\langle V^2 \rangle$ , the spatio-temporal distribution of bulk density  $\rho_H$  calculated from the volume fraction from Eq.( 4-14 ) is shown in Fig. 4-12. As you can see, this method is under development and it is not yet possible to output high resolution and high accuracy distributions. Even now, many researches have been done to determine each variable as mentioned in

the previous section (e.g. Guerrero and Vittorio, 2018; Povey, 1997). However, the obtained distribution also gives us helpful information for understanding the flow structures of the turbidity current. In the density distribution, it is confirmed that the head region and bottom region near the bed contains high density corresponding to almost  $1008 \text{ kg/m}^3$  of initial density. Because the density of the quartz particles is  $2650 \text{ kg/m}^3$ , they are heavier than water. Therefore, it is a reasonable result that the density of the particle-suspended layer becomes larger as the height  $y$  is lower. In addition to that, as estimated from the vector field, in the head region, a bottom layer is raised from near the bed to near the upper boundary by the rolling-up structure.

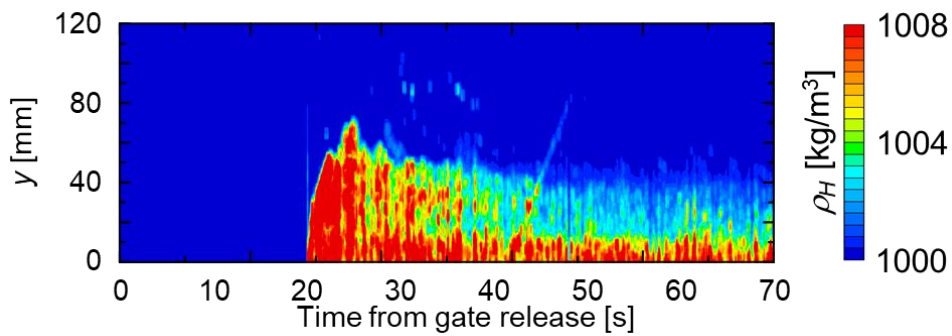


**Fig. 4-12 Spato-temporal density distribution calculated from echo values**

The time-averaged volume fraction  $\alpha$  and the root mean square value of the fluctuation component  $\alpha'_{\text{RMS}}$  in the body region of  $35 < t < 70$  s are shown in Fig. 4-13. Since this analysis does not contain an algorithm that returns a value of 0 or 1 at each measurement point, there is no influence of the Heaviside formula,

$$\sqrt{\alpha} = \alpha'_{\text{RMS}}, \quad (4-15)$$

Paying attention to the  $\alpha$  profiles, the value approaches the maximum value of 0.5% near the bottom. Also, the increase in the values is observed especially below the height of  $h_m$ , where  $u$  takes the maximum value. In the profiles of fluctuation component  $\alpha'_{\text{RMS}}$ , that takes local minimum value at  $y \approx 20$  mm. At that height, the  $\alpha$  profiles have an inflection point. In addition, at around  $y = 30$  mm, the  $\alpha'_{\text{RMS}}$  profiles show a positive peak like the shape observed in  $u'_{\text{RMS}}$  profiles shown in Fig. 4-6. From these results, it is expected that the fluctuation of the volume fraction is closely related to the fluctuation of the horizontal velocity component. That is to say, it seems that the specific flow structure of the turbidity current as a turbulent flow contributes to such profiles of the volume fraction.

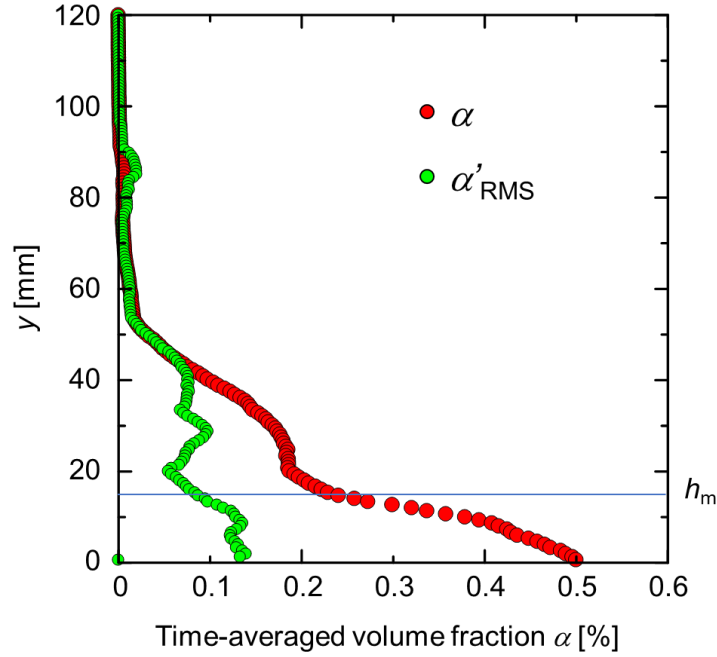


**Fig. 4-13** Time-averaged volume fraction in the body region of  $35 < t < 70$  s

### 4.2.3. Momentum equation in the body region

In this section, the body region of the current, which can be treated as a quasi-steady flow, is discussed using a momentum conservation equation. For two-phase flows, two-fluid model has been used to reveal flow structures in wide fields. Especially in the case of dispersed bubbly flow, a momentum conservation equation based on two-fluid model has been used (e.g. [Murai and Matsumoto, 2000](#); [Kitagawa et al., 2001](#)). The momentum conservation equations which can be applied to this study are explained below and we aim to quantify the flow structure in the body region.

The momentum conservation equation for a two-phase flow by the two-fluid model is described as

$$\frac{\partial f_L \rho_L \mathbf{u}_L}{\partial t} + \nabla \cdot f_L \rho_L \mathbf{u}_L \mathbf{u}_L = -f_L \nabla p + \mathbf{M}_{LL} + \mathbf{M}_{SL}, \quad (4-16)$$

$$\frac{\partial f_S \rho_S \mathbf{u}_S}{\partial t} + \nabla \cdot f_S \rho_S \mathbf{u}_S \mathbf{u}_S = -f_S \nabla p + \mathbf{M}_{SS} + \mathbf{M}_{LS}, \quad (4-17)$$

where suffix L and S denote liquid and solid phase. The local time-dependent variables  $f$ ,  $\mathbf{u}$ ,  $p$  are volume fraction, velocity vector, and pressure, respectively. The terms  $\mathbf{M}_{LL}$  and  $\mathbf{M}_{SS}$  are the inner phase momentum transport, which is modeled in the case of particle-laden flow as below:

$$\begin{aligned}
 \mathbf{M}_{LL} + \mathbf{M}_{SS} = & \\
 \nabla \cdot \mu \left\{ \nabla \mathbf{u}_L + (\nabla \mathbf{u}_L)^T - \frac{2}{3} (\nabla \cdot \mathbf{u}_L) \right\} + f_L \rho_L \mathbf{g} & \quad (4-18) \\
 + \nabla \cdot \mu \left\{ \nabla \mathbf{u}_S + (\nabla \mathbf{u}_S)^T - \frac{2}{3} (\nabla \cdot \mathbf{u}_S) \right\} + f_S \rho_S \mathbf{g} &
 \end{aligned}$$

where  $\mu$  and  $\mathbf{g}$  are viscosity and the acceleration vector of gravity, respectively. Here, the velocity vectors  $\mathbf{u}_L$  and  $\mathbf{u}_S$  can be treated as the same value  $\mathbf{u}$  according to Stokes number which is a dimensionless number characterizing the behavior of particles suspended in a fluid flow:

$$St = \frac{\rho_p d_p^2 U_0}{18 \mu_w L_0} \quad (4-19)$$

where  $U_0$  and  $L_0$  are representative flow velocity and length, and their values are substituted by the time-averaged values of the layer-averaged velocity  $U$  and zero-velocity height  $h_t$  shown in [Table 4-1](#). As the result of calculation, the value of  $St$  is in order of  $10^{-5}$  ( $St \ll 1$ ), which means that the motion of the suspended particles is traceable to the fluid flow in this experimental case. Therefore, the Eq.( 4-18 ) is rewritten as

$$\begin{aligned}
 \mathbf{M}_{LL} + \mathbf{M}_{SS} = & \\
 \nabla \cdot \mu_H \left\{ \nabla \mathbf{u} + (\nabla \mathbf{u})^T - \frac{2}{3} (\nabla \cdot \mathbf{u}) \right\} + f_L \rho_L \mathbf{g} + f_S \rho_S \mathbf{g} & \quad (4-20)
 \end{aligned}$$

where  $\mu_H$  is the effective viscosity of particle-suspended fluid. In case of clay-free dispersions of sand, the value of effective viscosity was given by [Davidson et al. \(1977\)](#) as

$$\mu_H = \mu_w (1 - 1.35\alpha)^{-2.5}, \quad (4-21)$$

where  $\alpha$  is the volume fraction of the quartz in this case. Then, the terms  $\mathbf{M}_{GL}$  and  $\mathbf{M}_{LG}$  are mutual phase momentum transport. These two terms have the following relationship according to Newton's third law:

$$\mathbf{M}_{SL} + \mathbf{M}_{LS} = 0. \quad (4-22)$$

Taking sum of Eq.( 4-16 ) and Eq.( 4-17 ), the equation of total momentum conservation is described by

$$\begin{aligned}
 \frac{\partial (f_L \rho_L + f_S \rho_S) \mathbf{u}}{\partial t} + \nabla \cdot (f_L \rho_L + f_S \rho_S) \mathbf{u} \mathbf{u} = & \\
 -(f_L + f_S) \nabla p + \nabla \cdot \mu_H \left\{ \nabla \mathbf{u} + (\nabla \mathbf{u})^T - \frac{2}{3} (\nabla \cdot \mathbf{u}) \right\} + (f_L \rho_L + f_S \rho_S) \mathbf{g} & \quad (4-23)
 \end{aligned}$$

The fluid is composed of just the quartz particles and water, so there is a relationship as

$$f_L + f_S = 1, \quad (4-24)$$

$$f_L \rho_L + f_S \rho_S = \rho_H; \quad (4-25)$$

hence,

$$\frac{\partial \rho_H \mathbf{u}}{\partial t} + \nabla \cdot \rho_H \mathbf{u} \mathbf{u} = -\nabla p + \nabla \cdot \mu_H \left\{ \nabla \mathbf{u} + (\nabla \mathbf{u})^T - \frac{2}{3} (\nabla \cdot \mathbf{u}) \right\} + \rho_H \mathbf{g}. \quad (4-26)$$

Treating the quartz-suspended fluid as incompressible fluid yields

$$\frac{\partial \rho_H \mathbf{u}}{\partial t} + \nabla \cdot \rho_H \mathbf{u} \mathbf{u} = -\nabla p + \nabla^2 (\mu_H \mathbf{u}) + \rho_H \mathbf{g}. \quad (4-27)$$

As seen in the previous section, the horizontal velocity component is dominant in the body region of the turbidity current. Focusing on streamwise direction (horizontal velocity), the momentum conservation equation expressed by componential velocity is described by

$$\frac{\partial \rho_H u}{\partial t} + \frac{\partial \rho_H u u}{\partial x} + \frac{\partial \rho_H u v}{\partial y} + \frac{\partial \rho_H u w}{\partial z} = -\frac{\partial p}{\partial x} + \left( \frac{\partial^2 \mu_H u}{\partial x^2} + \frac{\partial^2 \mu_H u}{\partial y^2} + \frac{\partial^2 \mu_H u}{\partial z^2} \right) + F_g, \quad (4-28)$$

where  $F_g$  denotes the external force caused by the gravity. The following variable separation into time-average and fluctuation components is carried.

$$\left\{ \begin{array}{l} \rho_H = \overline{\rho_H} + \rho'_H \\ u = \overline{u} + u' \\ v = \overline{v} + v' \\ w = \overline{w} + w' \\ \mu_H = \overline{\mu_H} + \mu'_H \end{array} \right. \quad (4-29)$$

where  $u$ ,  $v$ , and  $w$  stand the streamwise velocity, vertical velocity, and spanwise velocity, respectively. By substituting these equations into Eq.( 4-28 ) and averaging overall time for the body region  $35 < t < 70$  s, the following equation is obtained:

$$\begin{aligned} & \frac{\partial}{\partial x} \left( \overline{\rho_H u u} + \overline{\rho_H u' u'} + 2\overline{\rho_H u' u} + \overline{\rho_H u' u'} \right) \\ & + \frac{\partial}{\partial y} \left( \overline{\rho_H u v} + \overline{\rho_H u' v'} + \overline{\rho_H v' u} + \overline{\rho_H u' v'} + \overline{\rho_H u' v'} \right) \\ & + \frac{\partial}{\partial z} \left( \overline{\rho_H u w} + \overline{\rho_H u' w'} + \overline{\rho_H w' u} + \overline{\rho_H u' w'} + \overline{\rho_H u' w'} \right) \\ & = \frac{\partial^2 (\overline{\mu_H u} + \overline{\mu'_H u'})}{\partial x^2} + \frac{\partial^2 (\overline{\mu_H u} + \overline{\mu'_H u'})}{\partial y^2} + \frac{\partial^2 (\overline{\mu_H u} + \overline{\mu'_H u'})}{\partial z^2} + \frac{\partial p}{\partial x} + F_g \end{aligned} \quad (4-30)$$

In a well-developed flow, there is no mean vertical velocity ideally and no mean spanwise velocity. The gradient of momentum in the streamwise and spanwise directions is also negligible;

therefore,

$$\frac{\partial}{\partial y} \left( \overline{\rho_H \overline{u'v'}} + \overline{\rho_H \overline{v'u}} + \overline{\rho_H \overline{u'v'}} \right) = \frac{\partial^2 \left( \overline{\mu_H \overline{u}} + \overline{\mu_H \overline{u'}} \right)}{\partial y^2} + \frac{\partial p}{\partial x} + F_g. \quad (4-31)$$

This equation is rewritten by

$$\frac{\partial p}{\partial x} = \frac{\partial}{\partial y} \left( \frac{\partial \overline{\mu_H \overline{u}}}{\partial y} + \frac{\partial \overline{\mu_H \overline{u'}}}{\partial y} - \overline{\rho_H \overline{u'v'}} - \overline{\rho_H \overline{v'u}} - \overline{\rho_H \overline{u'v'}} \right) + F_g. \quad (4-32)$$

Eventually the shear stress in the case of turbidity current consists of five terms as follows:

$$\tau_1 = \frac{\partial \overline{\mu_H \overline{u}}}{\partial y}, \quad (4-33)$$

$$\tau_2 = \frac{\partial \overline{\mu_H \overline{u'}}}{\partial y}, \quad (4-34)$$

$$\tau_3 = -\overline{\rho_H \overline{u'v'}}, \quad (4-35)$$

$$\tau_4 = -\overline{\rho_H \overline{v'u}}, \quad (4-36)$$

$$\tau_5 = -\overline{\rho_H \overline{u'v'}}. \quad (4-37)$$

In the study by [Middleton \(1966\)](#), it is reported that the shape and velocity in the head region are adequately independent of the slope of the flume in case with angle  $< 2.3^\circ$ . Hence, the term of  $F_g$  was assumed to be negligible, because the experimental flume was inclined at just  $1.38^\circ$  in the present study.

The computed results of the five components of shear stress are shown in [Fig. 4-14](#), where the shear stresses from the effect of viscosity  $\tau_1$  and  $\tau_2$  are shown in [Fig. 4-14\(a\)](#) and the three components of turbulent shear stress  $\tau_3$ ,  $\tau_4$ , and  $\tau_5$  are shown in [Fig. 4-14\(b\)](#). These values are computed from the experimental results obtained by a pair of UVPs in the body region of the current, where the averaging window is  $35 < t < 70$  s. The shear stresses shown on the horizontal axis are normalized by wall shear stress  $\tau_w$  estimated from the logarithmic fitting for the experimental results of velocity distribution according to the law of the wall as discussed above, and the  $y$  axis denotes normalized height by the zero-velocity height  $h_t$ . As you can see, the shear stress of  $\tau_1$  shows the maximum value of  $\tau_1 / \tau_w \approx 0.3$  near the bed and the value is largest in the whole distributions and the values of  $\tau_2$  is much smaller than  $\tau_1$ . In the profiles of the three components of turbulent shear stress, Reynolds shear stress  $\tau_3$  is dominant, and the distributions of  $\tau_4$  and  $\tau_5$  have small fluctuation of the

values, but the values are much smaller than  $\tau_3$ . In the previous study about gas–liquid two–phase channel flow, it was reported that the profiles of  $\tau_4$  take negative values near the top, which was caused by the fluctuation correlation between the local void fraction and the vertical liquid velocity (Murai *et al.*, 2006). Considering that result, it is expected that the profiles of  $\tau_4$  in this study show different distribution from that in case of single–phase flows. Actually, however, the noticeable difference cannot be observed. The reason for deriving such a result seems to be that the local volume fraction of suspended particle ( $\alpha \leq 0.5\%$ ) is much smaller than that in the case of bubbly flow with around 60% in the maximum void fraction.

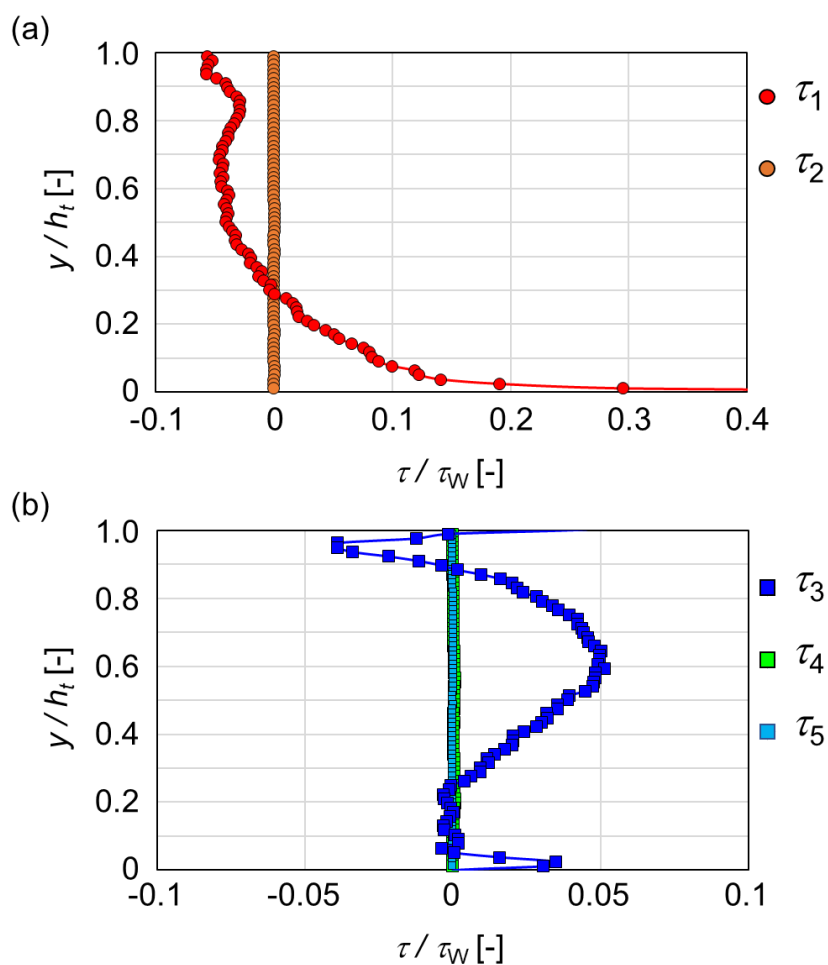


**Fig. 4-14** Computed profiles of the shear stress; (a) shear stresses caused by viscosity and (b) turbulent shear stresses

In addition, the distribution of viscous stress  $\tau_1$  and Reynolds stress  $\tau_3$  show characteristic shapes. Ideal distributions of  $\tau_1$  and  $\tau_3$  in a channel flow are shown in Fig. 4-15 (Kida and Yanase, 1999 (in Japanese)), and such an axisymmetric flow contains point-symmetric distributions of shear stresses.

Contrary to that, the distributions of  $\tau_1$  and  $\tau_3$  in this study do not have such profiles. The difference about  $\tau_1$  between the present study and a channel flow is the upper boundary, where it is an ambient fluid in this study and a solid wall in the channel flow. Therefore, the result of  $\tau_1$  in this experiment, which the upper part takes negative values overall, is due to the shear flow by the ambient fluid. On the other hand, the Reynolds shear stress  $\tau_3$  takes a value of close to zero near the bed (inner region:  $y < h_m$ ). The presence of particles may suppress the fluctuation of velocity components as described above.

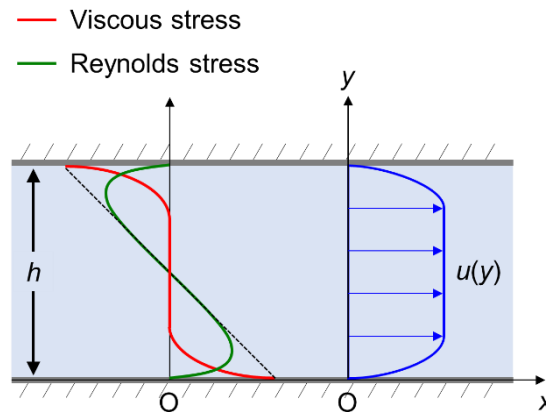


**Fig. 4-15** Schematic of shear stress in case of single-phase channel flow (Kida and Yanase, 1999 (in Japanese))

The total shear stress, which is the sum of five shear stress components ( $\tau_1$ ,  $\tau_2$ ,  $\tau_3$ ,  $\tau_4$ , and  $\tau_5$ ), is shown in Fig. 4-16. The computed result taking the value close to zero in the range of  $0.3 < y/h_t < 0.8$  indicate that the values of  $\tau_1$  and  $\tau_3$  are nearly canceled out. The total shear stress at  $y = 0.561$  mm, the lowest measurement point by UVP in this study, is 0.030 Pa. That value is the same order as 0.086 Pa of the wall shear stress  $\tau_w$  estimated from the fitting result for the velocity distribution according to law of the wall.

Additionally, the wall shear stress is roughly estimated just from the geometric configuration in case of this experimental facility. An extremely simplified experimental flume is shown in Fig. 4-17 to discuss the force balance in a hydrostatic fluid pressure. In the figure,  $A$  and  $B$  denote area of the bottom and the cross section of the flume, respectively. Then, the wall shear stress working at the bed is described as  $\tau_w$  and the pressure difference  $\Delta p$  is generated by the density difference of the both fluids between the left-hand side and the right-hand side. Considering the force balance of these physical quantities, the following equation is obtained,

$$\tau_w \cdot A = \Delta p \cdot B. \quad (4-38)$$

Here, it can be assumed that the pressure difference  $\Delta p$  is generated by the density difference between the particle-suspended fluid and ambient fluid, and their density are shown as  $\rho_H$  and  $\rho_W$ , respectively. Using such an assumption, the following relationship is obtained.

$$\begin{aligned}\Delta p &\approx \Delta \rho g \frac{B}{2} \\ &= (\rho_H - \rho_W) g \frac{B}{2}.\end{aligned}\quad (4-39)$$

As mentioned above, the test section is a rectangle flume with 4,548 mm in total length, 210 mm in height and 143 mm in width, so the values of  $A$  and  $B$  can be calculated easily. Substituting Eq.( 4-39) in Eq.( 4-38 ), the following equation is obtained,

$$\tau_w = \frac{B^2}{2A} \Delta \rho g . \quad (4-40)$$

The calculated value of the wall shear stress is 0.055 Pa, assuming that other forces like friction on the side walls are not working. This value shows the same order as the shear stresses calculated from the velocity distribution discussed above ( $\tau_w = 0.086$  Pa according to law of the wall). From this extremely simplified validation result, it is confirmed that the wall shear stress estimated form velocity distribution shows the reasonable order of value.

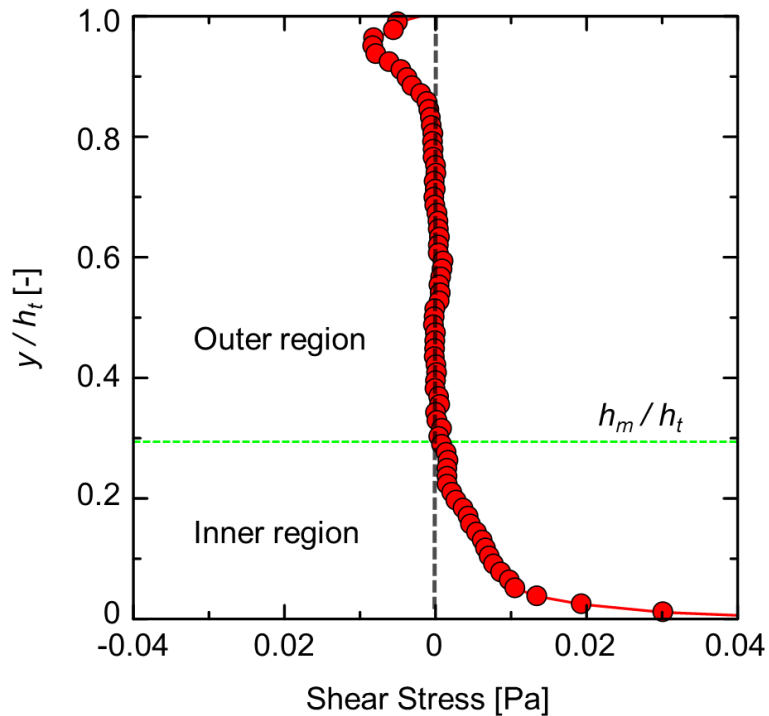


**Fig. 4-16** Sum of five shear stress components

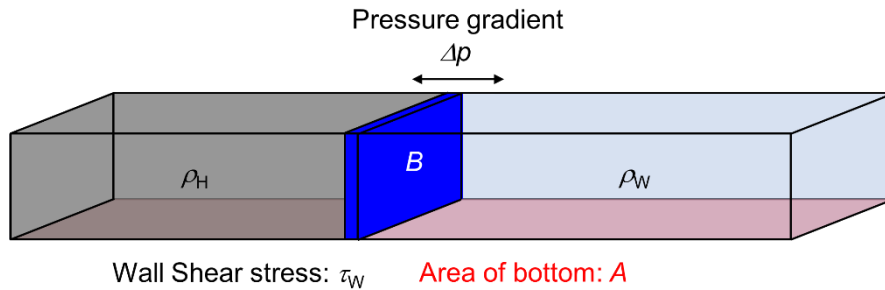


**Fig. 4-17 Schematic image of simplified experimental flume**

According to Eq.( 4-32 ), vertical profiles of the pressure gradient acting on the body region of the current ( $35 < t < 70$  s) can be calculated by differentiating the total shear stress with respect to the height  $y$  direction, and the obtained distribution is shown in Fig. 4-18. As mentioned above, since the shear stresses are balanced inside the flow (outer region:  $h_m < y < h_t$ ), the pressure gradient shows large values only near the upper ( $y \approx h_t$ ) and lower boundaries (inner region:  $y < h_m$ ).

Such a phenomenon seen in the region  $0.3 < y / h_t < 0.8$  (outer region) shows a negative momentum transfer against the mean velocity gradient, which is working to keep a stable stratification. The negative momentum transfers are reported in the previous experimental studies on turbulent transport phenomenon in density stratification, for instance, saline density stratified flows and wind tunnel experiments (e.g. Komori *et al.*, 1983; Piccirillo and van Atta, 1997). This study reveals the existence of such the phenomenon in the turbidity currents containing fine particles, that is, solid–liquid two–phase turbulent flows. In this case, as the result of the turbulent energy balanced with the potential energy of the suspended particles, it is expected that the particles are being mixed by the velocity fluctuation components. It has the effect to suppress the settling of the suspended particles and to keep  $\rho_H$  at a roughly constant value. Additionally, in the inner region of the body region, the particle-laden flow with high density  $\rho_H$  is extruded from the rear by a pressure gradient shown in Fig. 4-18, that contributes to a large amount of particle transporting action.

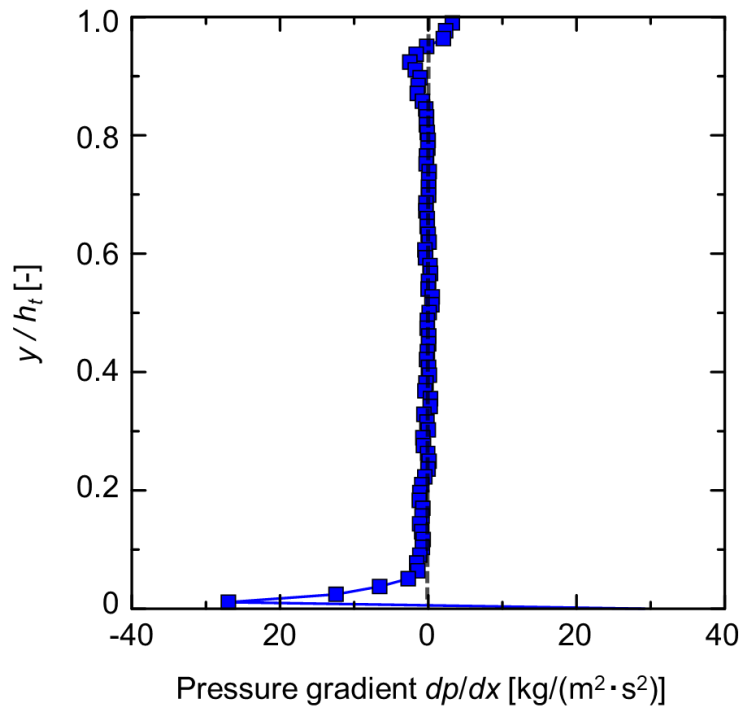


**Fig. 4-18** Computed pressure gradient

#### 4.3. Comparison of flow structures between quartz-suspended currents, and opalin-suspended currents, and two-layer turbidity currents

In this section, the differences of flow characteristics between one-layer turbidity currents including quartz-suspended currents and opalin-suspended currents and two-layer turbidity currents are discussed. The behavior of currents with more clearly different initial conditions from each other than the conditions discussed above is described. The currents of total nine experimental cases are mainly discussed in this section. These initial conditions and front velocity calculated by the pattern matching method are summarized in [Table 4-5](#). In Case 19, the quartz-suspended fluid contained in tank A was colored by a red ink to distinguish from the fluid contained in the tank B.

**Table 4-5 Initial conditions and calculated front velocity**

Exp. case	Density [kg/m <sup>3</sup> ]		$U_f$ [mm/s]
	Tank A	Tank B	
1		Q1008	50.0
9		Q1016	74.2
10		Q1032	114.8
16		O1008	41.1
17		O1016	48.8
18		O1032	74.0
19	Q1032	Q1016	87.3
20	Q1032	O1016	85.8
22	O1032	Q1016	69.5

#### 4.3.1. Experimental snapshots of the currents

Outline motions of the two-layer turbidity currents invading into the ambient fluid are monitored as sequential images from  $t = t_0$  to  $t_0 + 10.5$  s. The images were taken by the digital camera installed in front of the flume for Case 19, 20, and 22 (Fig. 4-19, Fig. 4-20, and Fig. 4-21). In the images of Case 19, the lower layer is composed of water colored by red ink and quartz particles with 2.0% in volume fraction, but it is difficult to distinguish the red lower layer from white upper layer. On the other hand, the sequential images of experimental Case 20 and 22 show the rough boundary distinguishing the upper layer and lower layer due to the color differences of those two layers, which means that the quartz-suspended layer has white color and the opalin-suspended layer has black color. From these images, it is confirmed that this experimental facility is able to generate two-layer turbidity currents. Comparing the sequential images of the three cases, flow structures of them can be discussed qualitatively. The large vortex structures attributed to the K-H instability can be observed near the upper boundary in the all cases. Although the quantitative discussion cannot be done, the wavenumber of the interfaces between the particle-laden fluid and the ambient fluid formed by some visible large vortices in the images almost does not vary under the three conditions. In addition, the rolling-up structures in the head region is particularly well visible in the images of the Cases 20 and 22.

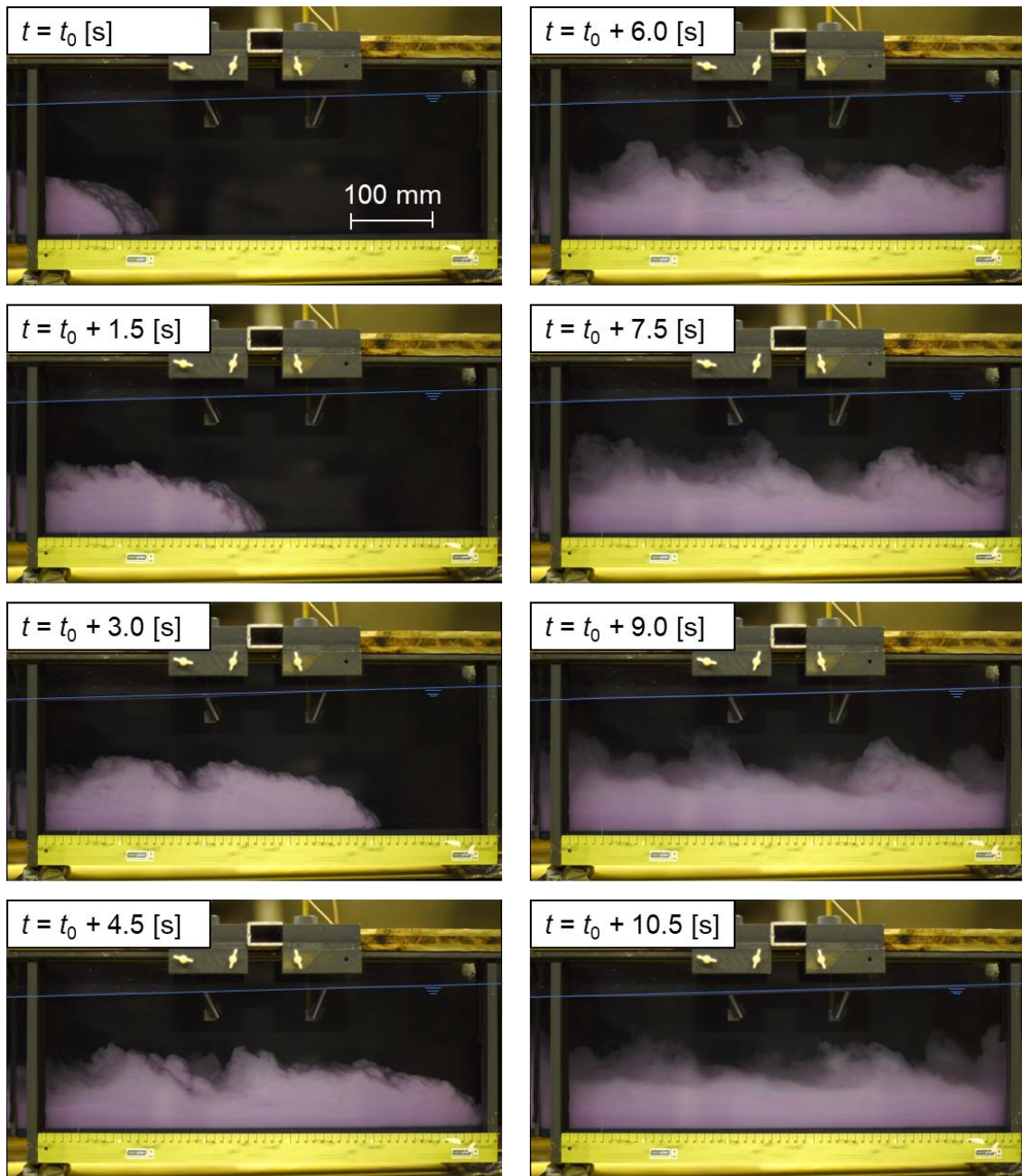


**Fig. 4-19** Snapshots of quartz-suspended turbidity currents of Case 19 from  $t = t_0$  to  $t_0 + 10.5$  s

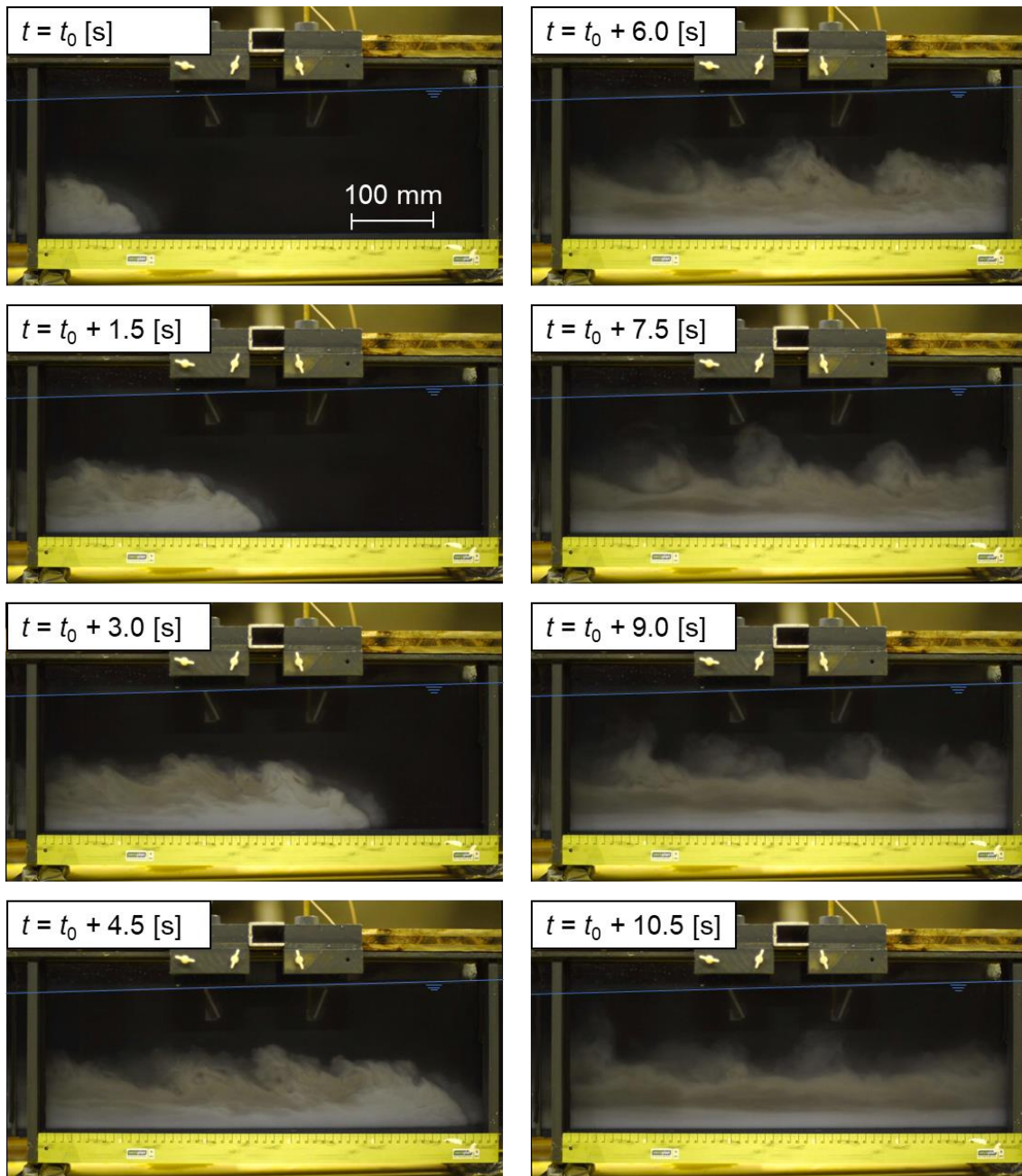


**Fig. 4-20** Snapshots of quartz-suspended turbidity currents of Case 20 from  $t = t_0$  to  $t_0 + 10.5$  s

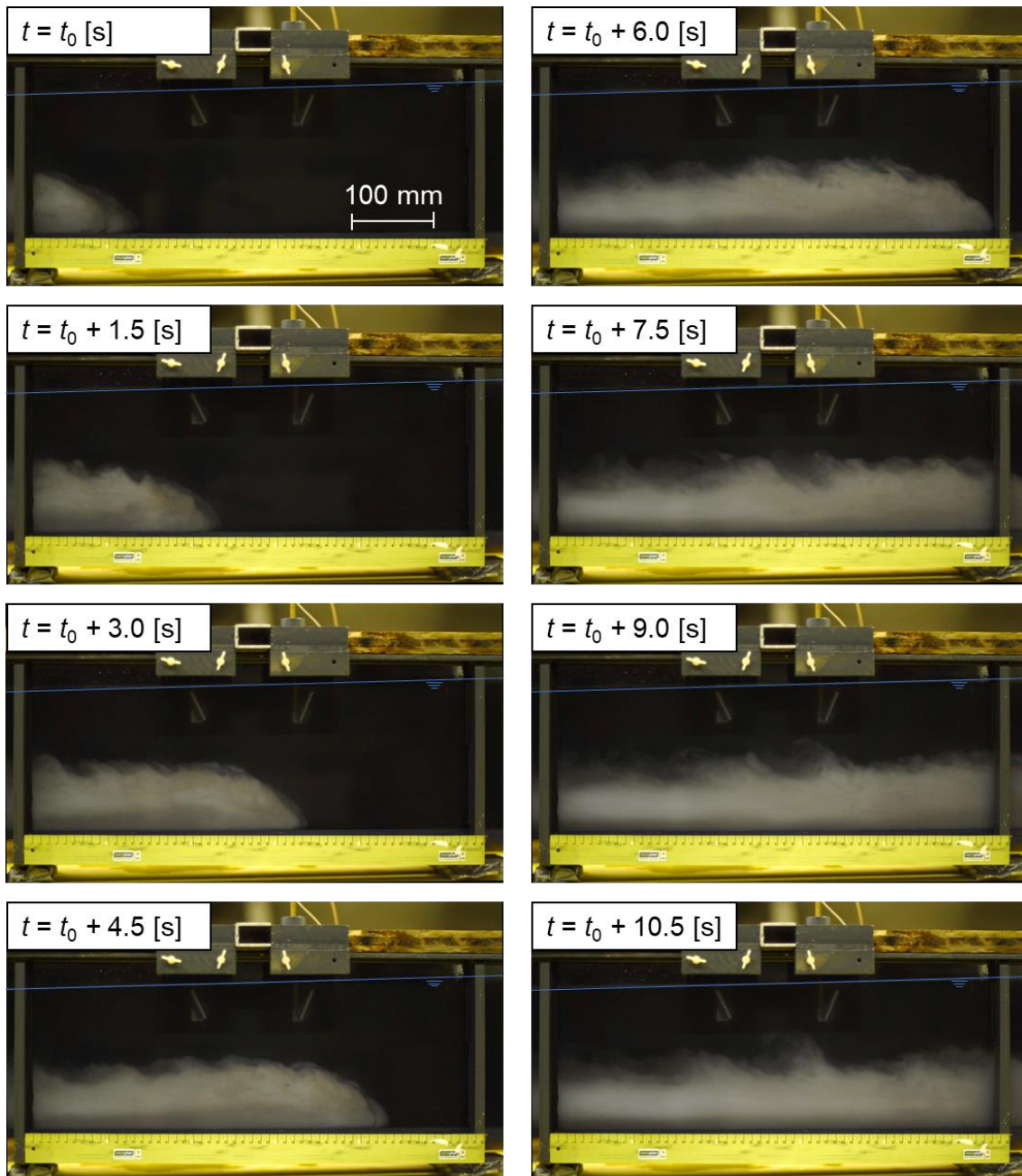


**Fig. 4-21** Snapshots of quartz-suspended turbidity currents of Case 22 from  $t = t_0$  to  $t_0 + 10.5$  s

#### 4.3.2. Inner flow structures

Spatio-temporal distributions of horizontal and vertical velocity components ( $u$  and  $v$ ) obtained by VVP in each case are shown in Fig. 4-22 and Fig. 4-23, where (a) left, (b) middle, and (c) right panels represents the results of quartz-laden currents, opalin-laden currents, and two-layer currents, respectively. The axes denote the height ( $y$ ) from the bed and the elapsed time ( $t$ ) from the release of

the gate 1. As the color scale of velocity magnitude,  $u$  is dominant in the flow in those cases too. Paying attention to the cases of (a) quartz-laden currents and (b) opalin-laden currents, the initial density of the particle-suspended fluids becomes larger from the upper panels to lower, namely the density of the upper panels, middle panels, and lower panels are 1008, 1016, and 1032 kg/m<sup>3</sup>, respectively. Under each condition, it is confirmed that the horizontal velocity component  $u$  is increasing as the initial density of the particle-suspended fluids becomes larger from color contour in the panels. In addition, comparing the quartz-laden current and the opalin-laden current having the same initial density, it also can be confirmed that the quartz-laden current exhibits larger velocity values as a rough tendency. Contrary to that, the bulk density of (c) two-layer turbidity currents is constant value within experimental Case of 19, 20, and 22. The calculated bulk density considering the volume difference between the tank A and the tank B is 1023 kg/m<sup>3</sup>. In those three cases, the spatio-temporal distributions of horizontal velocity  $u$  show similar values and trends between the experimental Cases 19 and 20, but the distribution of Case 22, where the bottom is composed of the opalin layer, shows lower velocity values in comparison with those two cases (Case 19 and Case 20). From these comparisons, it is predicted that the opalin-laden currents and two-layer currents, where the bottom layer is the opalin, have a tendency to have lower velocity values comparing with the quartz-laden currents. The dot lines shown in Fig. 4-22 indicate the expected arrival time  $t^*$  defined in the previous section at  $x_l = 1005$  mm that is the cross point of two ultrasonic measurement lines. Those expected arrival time summarized in Table 4-6 roughly coincides with the results measured by UVP in the cases discussed in this section.

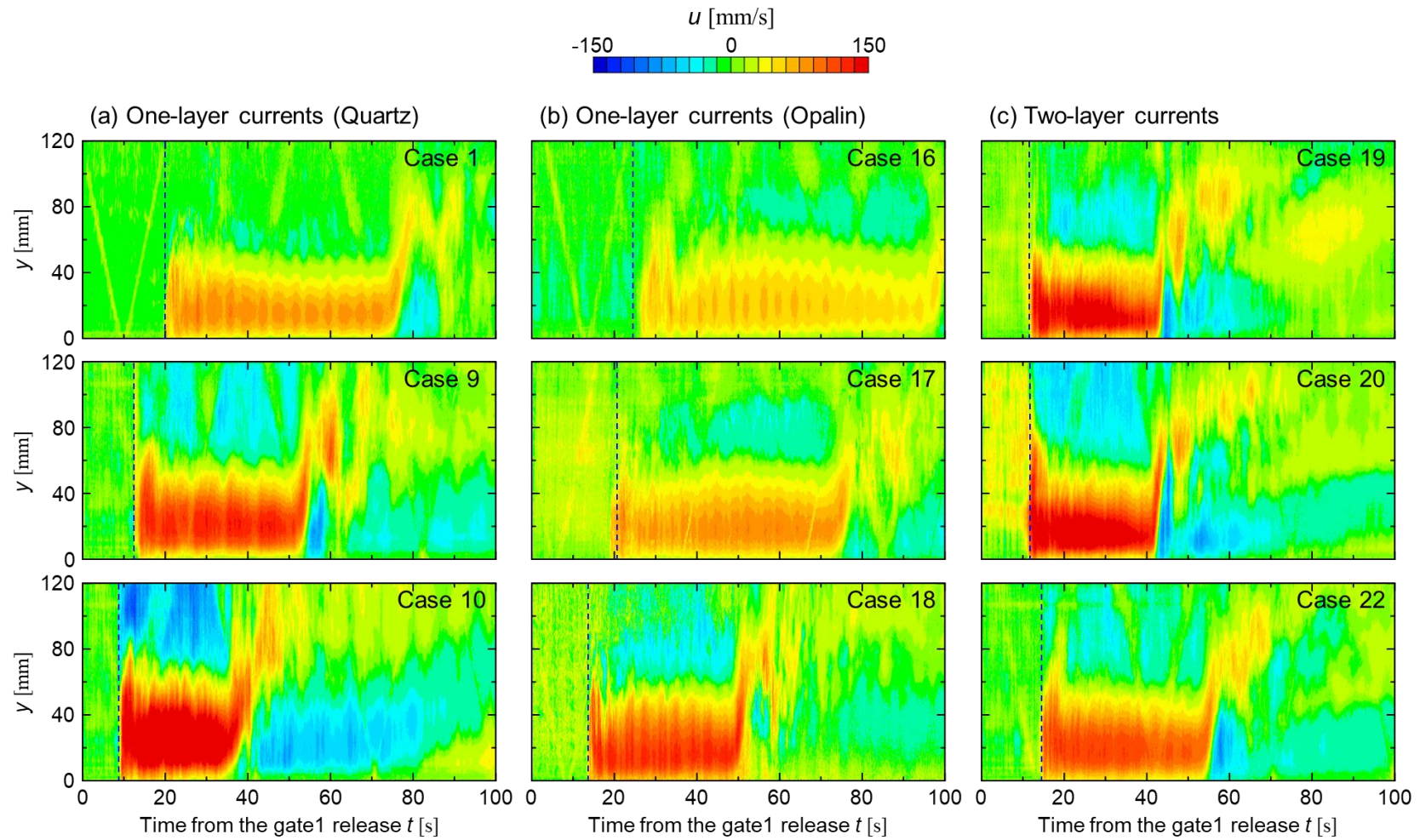


**Fig. 4-22** Spatio-temporal distributions of horizontal velocity component: (a) quartz-laden currents, (b) opalin-laden currents, and (c) two-layer turbidity currents

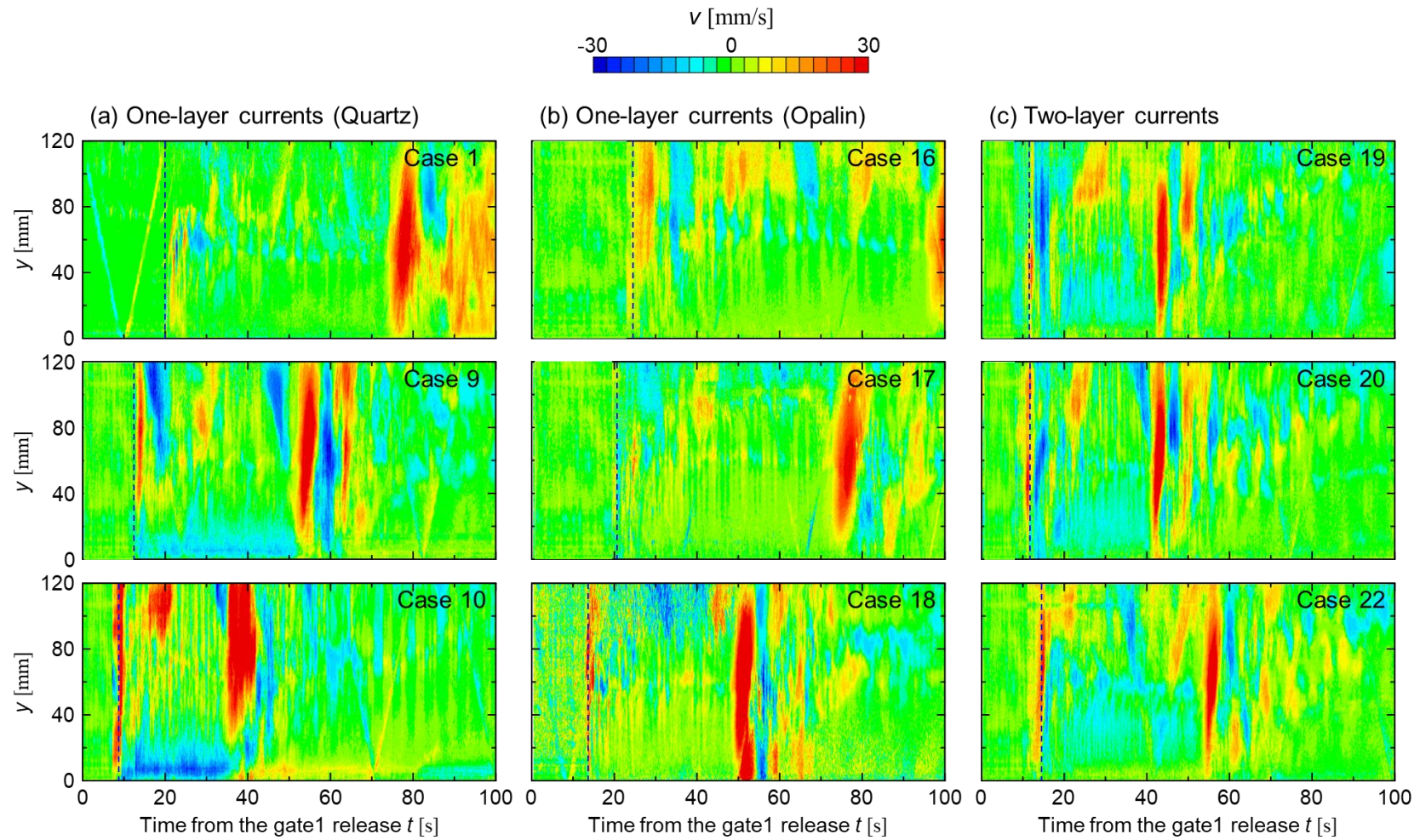


**Fig. 4-23** Spatio-temporal distributions of vertical velocity component: (a) quartz-laden currents, (b) opalin-laden currents, and (c) two-layer turbidity currents

In order to estimate the wall shear stress working in the body region, the body region should be separated from the head region. In these cases, however, the front velocity  $U_f$  varies with the initial conditions, and thus it is difficult to define the separation point between the head and the body of the currents from elapsed time  $t$ . Therefore, the length of the head is estimated from these experimental results. Concretely, combining the front velocity value  $U_f$  and the duration time evaluated from velocity distributions, the length of the head region can be estimated roughly. The duration time means passing time of the head of the currents under the ultrasonic measurement lines.  $U_f$  calculated by pattern matching method is used for the analysis. For qualitative understandings, the flow character defining the separation point between the head and the body is defined as the wake behind the head in a previous research. For example, such a flow character can be observed in the section of 4.2. As the results of such a process, the length of the head region in this study is estimated to be about 500 mm. Furthermore, based on empirical judgment using experimental results, in the experimental conditions and the experimental facility of this study, it was estimated that the body region, which is the wake of the head region, propagates over at least a length corresponding to 2000 mm. Using these estimated lengths, each time for the averaging window is defined as,

$$t_1 = t_{x=x_I+500 \text{ mm}}^* = \frac{x_I + 500}{U_f}, \quad (4-41)$$

$$t_2 = t_{x=x_I+2500 \text{ mm}}^* = \frac{x_I + 2500}{U_f}. \quad (4-42)$$

The time-averaging window is from  $t = t_1$  to  $t_2$ , so the window sizes are different in each experimental case as shown in Table 4-6.

**Table 4-6 Summary of the estimated arrival times**

Case	$U_f$ [mm/s]	$t_{x=1005 \text{ mm}}^*$ [s]	$t_1$ [s]	$t_2$ [s]
1	50.0	20.1	30.1	70.1
9	74.2	13.5	20.3	47.2
10	114.8	8.75	13.1	30.5
16	41.1	24.4	36.6	85.2
17	48.8	20.6	30.9	71.8
18	73.8	13.6	20.4	47.5
19	87.3	11.5	17.2	40.1
20	85.8	11.7	17.6	40.9
22	69.5	14.5	21.6	50.4

The profiles of the time-averaged  $u$  of each case are shown in Fig. 4-24, with the averaging window is from  $t = t_1$  to  $t_2$  calculated for each experimental case. In the panels of Fig. 4-24(a) and (b), the results in the cases of the quartz-laden currents and opalin-laden currents are shown and it is

confirmed that the values of the horizontal velocity components  $u$  also increase according to the initial density of the particle-suspended fluids (in these panels, the blue, green, and red symbols denote the experimental results of particle-laden flows with  $\rho_H = 1008$ , 1016, and 1032 kg/m<sup>3</sup>, respectively.).

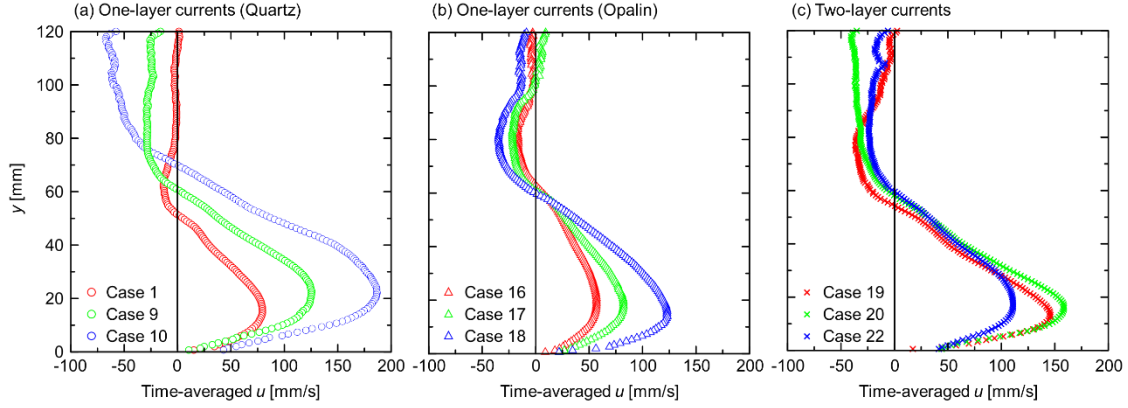


**Fig. 4-24 Time-averaged profiles of horizontal velocity component in the body region ( $t_1 < t < t_2$ ) of (a) quartz-laden currents, (b) opalin-laden currents, and (c) two-layer currents**

The representative horizontal velocity  $u$  and the heights of the currents calculating from the time-averaged velocity profiles are summarized in Table 4-7. Here,  $u_{\text{mean}}$  denotes the mean velocity based on the integration from  $y = 0$  to  $h_t$ . The dimensionless numbers to evaluate the general flow structures like Reynolds number (the ratio of inertial forces to viscous forces), densimetric Froude number (the ratio of inertia to the gravity), and Richardson number (the ratio of buoyancy term to inertia) are defined in the study by Kneller *et al.* (1999) as

$$u_{\text{mean}} = \frac{1}{h_t} \int_{y=0}^{h_t} u(y) dy, \quad (4-43)$$

$$Re = \frac{\rho_H u_{\text{mean}} D}{\mu_H}, \quad (4-44)$$

$$Fr' = \frac{u_{\text{mean}}}{\sqrt{g'D}}, \quad (4-45)$$

$$Ri = \frac{g'D}{2 u_{\text{mean}}^2}, \quad (4-46)$$

where,  $D$  is the current thickness and the quantitative clear definition of  $D$  is not expressed in the previous studies. In this study, therefore,  $h_t$  was used as the current thickness instead of  $D$ . Calculated those dimensionless numbers in the body region are shown in Table 4-8. The Reynolds numbers in the all cases have values of  $O(10^3)$ , so the currents are treated as turbulent flows. Comparing the one-layer currents between the quartz-laden and opalin-laden currents having same initial density, the Reynolds number is larger in cases of quartz-laden currents, which means that the viscosity more

affects the flow behavior in cases of opalin-laden currents. Based on the definition of  $Fr'$  and  $Ri$ , they have a relationship derived as

$$Ri = \frac{1}{Fr'^2} . \quad (4-47)$$

Paying attention to the values of  $Fr'$  and  $Ri$ , the quartz-laden currents and two-layer currents in Case 19 and Case 20, where the bottom layer is the quartz-suspended fluid, show higher  $Fr'$  values exceeding 0.7 than the remaining cases. Therefore, the  $Ri$  values show the opposite trend. It means that, in opalin-laden currents and two-layer currents of Case 22, where the bottom layer is the opalin-suspended fluid, buoyancy term is dominant.

**Table 4-7 Representative horizontal velocity and heights on the currents**

Case	$u_{\max}$ [mm/s]	$h_m$ [mms]	$h_r$ [mms]	$u_{\text{mean}}$ [mm/s]
1	79.7	15.3	56.2	50.6
9	125.9	187.3	61.6	77.6
10	187.3	22.7	69.0	116.1
16	57.0	20.7	73.7	37.7
17	82.1	18.0	62.3	53.4
18	123.0	14.0	58.9	79.7
19	146.0	13.3	54.9	84.1
20	158.5	16.0	58.2	91.2
22	111.0	16.7	60.9	70.4

**Table 4-8 Summary of dimensionless numbers; Reynolds number, densimetric Froude number, and Richardson number**

Case	$Re$ [-]	$Fr'$ [-]	$Ri$ [-]
1	$2.04 \times 10^3$	0.757	1.74
9	$3.39 \times 10^3$	0.788	1.61
10	$5.57 \times 10^3$	0.788	1.61
16	$2.00 \times 10^3$	0.495	4.08
17	$2.36 \times 10^3$	0.539	3.44
18	$3.27 \times 10^3$	0.586	2.92
19	$3.24 \times 10^3$	0.752	1.77
20	$3.74 \times 10^3$	0.792	1.60
22	$3.02 \times 10^3$	0.597	2.80

In order to estimate the wall shear stress in the body region  $y < h_m$  of these currents, the logarithmic fitting based on law of the wall, which was already discussed in chapter 4.1.3 was applied to these profiles. The fitting results are shown in Fig. 4-24, here the von Karman constant  $\kappa$  is substituted 0.41 assuming a smooth bed. In the panels shown as single logarithmic charts, each symbol indicates the experimental values and each solid line indicates the fitting results, and the distributions of both values show generally good agreement. The fitting results obtained by this method are summarized in Table 4-9. As the value of the maximum velocity of the horizontal component  $u$  increases, the value of  $u^*$  increases. Therefore, the value of  $u^*$  is normalized by  $u_{\max}$  and those values of  $u^*/u_{\max}$  take an averaged value of 0.114 in these nine cases not depending on the initial conditions. Utilizing this property, the friction coefficient  $C_f$  was calculated using the following equation

$$C_f = 2 \left( \frac{u^*}{u_{\max}} \right)^2. \quad (4-48)$$

The calculated values of  $C_f$  are shown in Table 4-9. Because of  $u^*/u_{\max} \approx 0.114$ , the values of  $C_f$  take around 0.0260, which was found to be one order larger than the values measured by the bubbly flows in case of horizontal channel flows (Murai *et al.*, 2006; Murai *et al.*, 2007) and towing tank experiment (Park *et al.*, 2018).

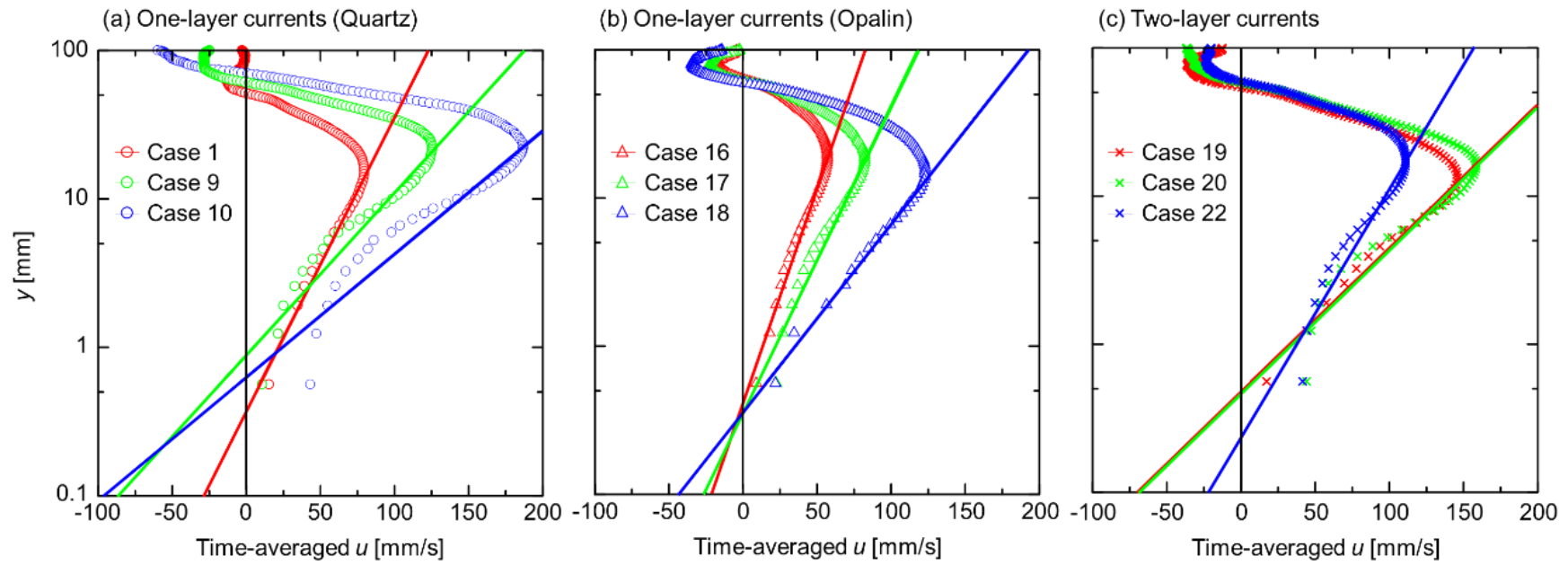


**Fig. 4-25** Fitting results for time-averaged profiles of horizontal velocity component in the body region of (a) quartz-laden currents, (b) opalin-laden currents, and (c) two-layer currents

**Table 4-9 Fitting results for experimental velocity values in the body region**

Case	$u^*$ [mm/s]	$y_0$ [mm]	$\tau_w$ [Pa]	$u^*/u_{\max}$ [-]	$C_f$ [-]
1	9.09	0.386	0.0833	0.114	0.0260
9	16.4	0.896	0.272	0.130	0.0338
10	21.4	0.635	0.474	0.114	0.0262
16	6.17	0.418	0.0384	0.108	0.0235
17	8.55	0.354	0.0743	0.104	0.0217
18	14.0	0.361	0.2028	0.114	0.0260
19	18.4	0.486	0.3472	0.126	0.0318
20	18.4	0.460	0.345	0.116	0.0268
22	10.6	0.235	0.116	0.0958	0.0184

### 4.3.3. Interfaces in two-layer turbidity currents

In the two-layer turbidity currents of the experimental Case 19, 20 and 22, the detection of two interfaces on ambient fluid–upper layer and upper layer–lower layer was tried to evaluate the flow behaviors. Optical timeline images for each case are shown in Fig. 4-26, which shows the time variation at  $x_l = 1005$  mm, corresponding to the cross point of two ultrasonic measurement lines. Since these images are taken from the front of the flume, the visible region is the flow state near the front side wall. In spite of that, the interfaces can be observed in these cases from the color differences between two layers. Especially, the interface between the upper layer and lower layer is easy to be detected in Case 20. In the image of Case 20, it is confirmed that the lower layer composed of quartz-suspended fluid reaches at  $y \approx 60$  mm in the head region, then the interface is distributed around  $y = 20$  mm in the body region, gradually decreasing from about  $t = 30$  s. After  $t = 40$  s, the flow returning from the end of the flume can be observed. Here, it is confirmed that the shape of the current head is maintained and that is invading under the current flowing from the left-hand side as shown like Fig. 4-27. From this behavior, it is predicted that the density of the head region is larger than that of the body region flowing from the left-hand side.

To compare the arrangements of the two layers (the lower layer and the upper layer) with these three Cases 19, 20 and 22, timeline image at  $x = x_l$  of the case 24 is shown in Fig. 4-28. In the Case 24, the current is composed of the lower quartz-suspended layer with  $\rho_H = 1032$  kg/m<sup>3</sup> and the upper opalin-suspended layer with  $\rho_H = 1008$  kg/m<sup>3</sup>. The bulk density considering the volume difference between the tank A and the tank B is 1019 kg/m<sup>3</sup>. In that case, the density difference between the lower layer and the upper layer is larger than the three cases mentioned above (Cases 19, 20 and 22), so the lower layer propagates much faster than the upper layer in Case 24. In the Fig. 4-28,

the upper layer is not clearly confirmed in the head region, and the black upper layer composed of opalin-suspended fluid can be seen at around  $t \geq 20$  s.

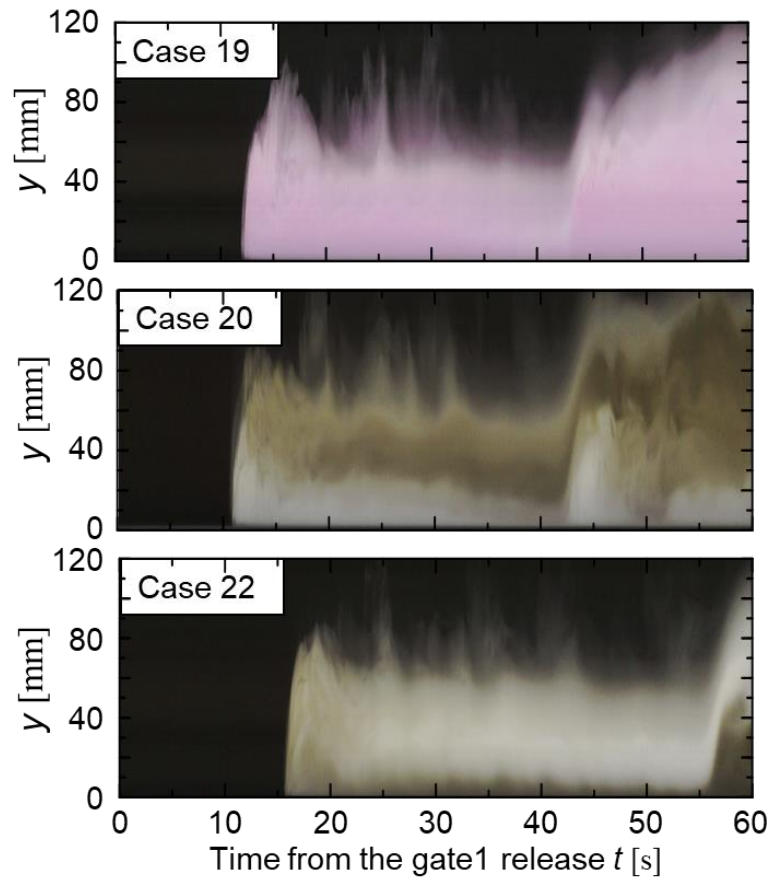


**Fig. 4-26** Timeline image at the cross-point of two ultrasonic beams, Case 19 is composed of quartz layers, Case 20 is composed of lower quartz layer and upper opalin layer, Case 20 is composed of lower opalin layer and upper quartz layer

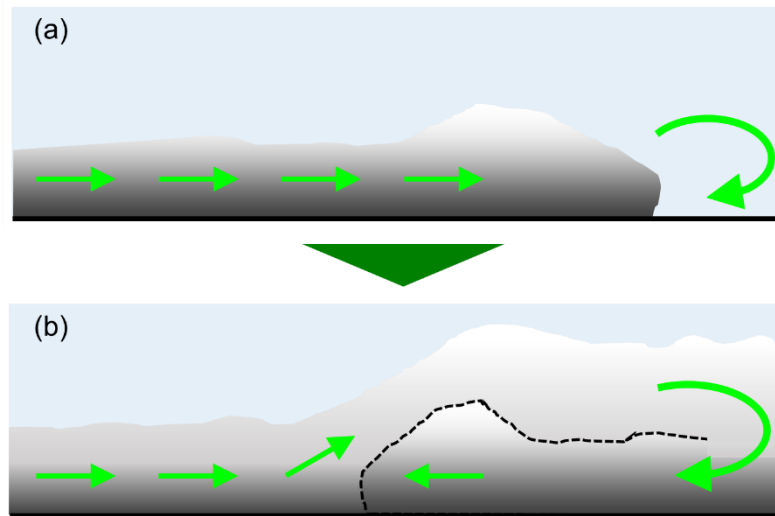


**Fig. 4-27** Schematic drawing of propagation of the head region under the down stream flow

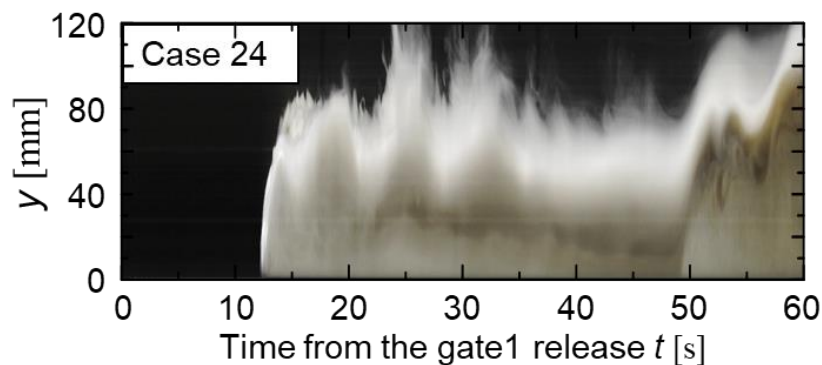


**Fig. 4-28** Timeline image of Case 24 at the cross-point of two ultrasonic beams

In order to evaluate the height of the interfaces, spatio-temporal echo distributions obtained by UVP were used. As mentioned above, in the simultaneous measurement of two UVPs, the ultrasonic interference noise occurs. To reduce the noise, the following series of processing (Fig. 4-29) was performed using the two echo distributions obtained from TDX 1 and TDX 2. In this processing, firstly, time correction method is applied to the spatio-temporal echo distribution too using front velocity  $U_f$  according to Eq.( 3-3 ) and Eq.( 3-4 ), since the positions of two ultrasonic transducers have a certain displacement outside the intersection point. As seen in Fig. 4-29(2), the echo distribution contains the ultrasonic interference noises distributed over time and space, which shows clearly large fluctuations compared with surrounding values. Next, therefore, the echo amplitude value which is the absolute value of the difference from the average value of the echo intensity, was calculated. Then, the smaller values are chosen for the reasonable values at each measurement point comparing two echo amplitude

values obtained from TDX 1 and TDX 2, because the noise has an obviously large value of echo amplitude. As the result of this processing, the noise-reduced distribution of echo amplitude can be obtained like Fig. 4-29(5).

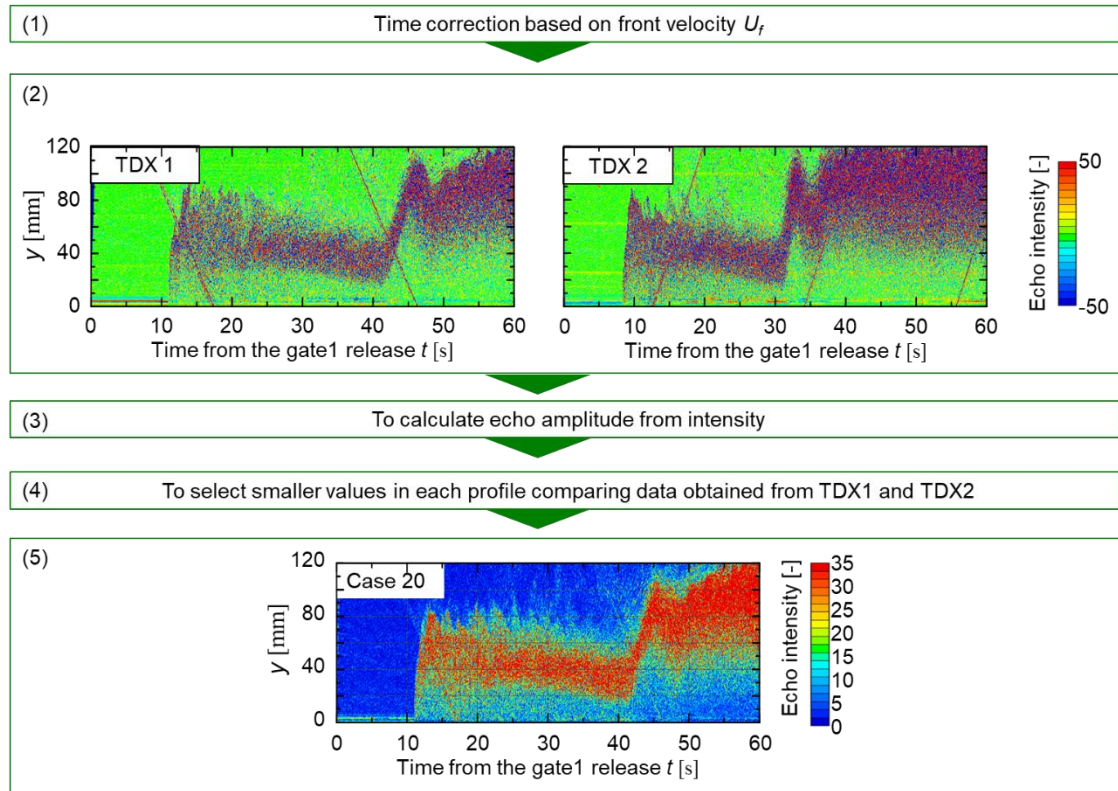


**Fig. 4-29 A series of noise reduction method in echo distributions**

The echo amplitude distributions of Case 19, 20, and 22 obtained using the noise reduction method are shown in Fig. 4-30. The noises are still remaining in these panels, but it is greatly improved in comparison with raw data of echo intensity distribution obtained by UVP. Comparing the results of the three cases, there are interesting differences depending on the combination of the kind of suspended particles contained in two layers; the upper layer and the lower layer. In Case 19, both layers are composed of quartz-suspended fluid, and echo amplitude distribution show approximately uniform values in the current. Contrary to that, the distributions of Case 20 and 22 have two regions in the currents; one of them shows a relatively larger values and the other is not so. The region showing large values is the layer composed of opalin-suspended fluid. As mentioned above, in case where the particle diameter  $d$  is much smaller than ultrasonic wave length  $\lambda$  ( $d/\lambda \ll 1$ ), Rayleigh scattering occurs. The scattering intensity increases as the particle diameter becomes larger in the cases of Rayleigh scattering. Since the center diameter of quartz and opalin particles are 12.2 and 18.9  $\mu\text{m}$ , respectively, it is reasonable that the opalin layer shows larger echo amplitude values. Using the characteristic, the

detection of two interfaces was examined for the experimental Cases 20 and 22.

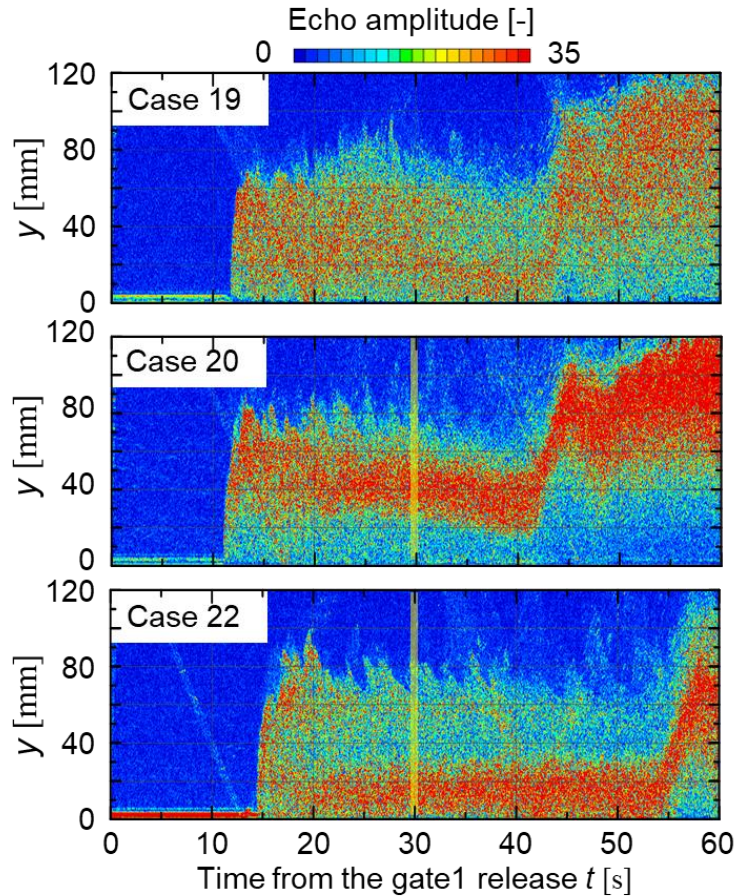


**Fig. 4-30** Spatio-temporal distributions of echo amplitude, Case 19 is composed of quartz layers, Case 20 is composed of lower quartz layer and upper opalin layer, Case 20 is composed of lower opalin layer and upper quartz layer

To measure the positions of interfaces quantitatively, the vertical profile of echo amplitude in Case 20 at  $t = 30$  s is shown in Fig. 4-31 as a sample. As shown in the figure, the echo amplitude has large fluctuations, that makes it difficult to detect interfaces using these instantaneous profiles at each measurement time. In order to overcome this difficulty, polynomial fitting was applied to the echo amplitude distributions at each measurement time, although an arbitrary property remains in this method. In this study, tenth-order polynomial function was examined for the fitting and the results are also shown in Fig. 4-31 by a blue solid line. The fitting result takes maximum value at  $y \approx 40$  mm and the height corresponds to approximately the center position of opalin layer in comparison with the distribution shown in Fig. 4-30. This method was also applied to the echo distribution on Case 22 and the results are shown in Fig. 4-32. In this result for the Case 22 shown by blue line too, the fitting

curve takes maximum value at  $y \approx 20$  mm corresponding to roughly the center of opalin layer. Therefore, it is expected that the values obtained from the polynomial fitting provide beneficial information to detect interfaces. The polynomial fitting was applied to the whole measurement time of echo amplitude in the Case 20 and 22, and the results are shown in Fig. 4-33.

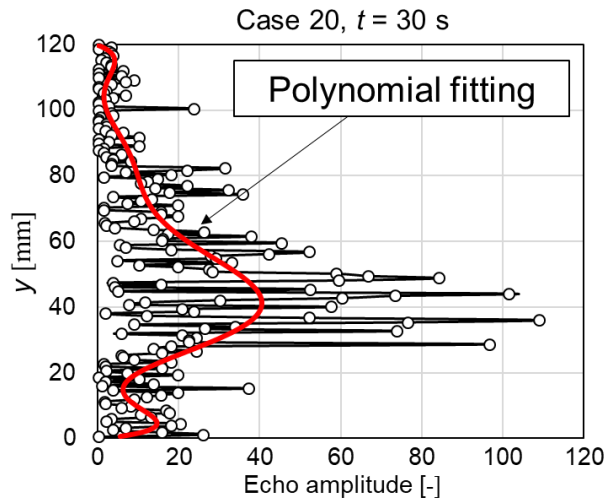


**Fig. 4-31** Vertical profile of echo amplitude in Case 20 at  $t = 30$  s

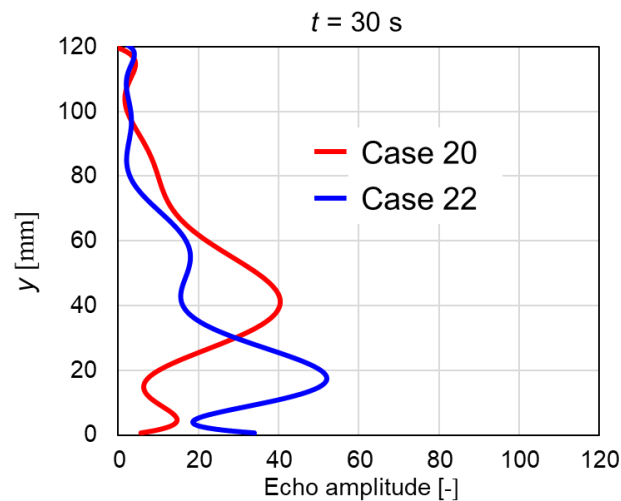


**Fig. 4-32** Fitting results for the Case 20 and 22

Using the fitting results, two kinds of threshold values  $T_1$  and  $T_2$  for the echo amplitude values  $E(y, t)$  were defined to determine two interfaces. The threshold value  $T_1$  is used for the interface between the upper layer and the lower layer, using the slope of the echo amplitude for the direction of height. In the two cases, the height of the opalin layer changes depending on the experimental case, so the values of  $T_1$  have different definition for each case like

$$T_1 = \text{Max.} \left[ \frac{dE(y,t)}{dy} \right] \text{ (for Case 20) ,} \quad (4-49)$$

$$T_1 = \text{Min.} \left[ \frac{dE(y,t)}{dy} \right] \text{ (for Case 22) .} \quad (4-50)$$

The height  $y_1$  satisfying the above conditional expression at each measurement time is treated as the interface 1. In addition, to determine the interface 2 between the upper layer and the ambient fluid, the values of  $T_2$  was defined as follows

$$T_2 = \frac{(E(y_1,t) - \text{Min.}[E(t)])}{2}, \quad (4-51)$$

where  $\text{Min.}[E(t)]$  means the minimum value of the echo amplitude at  $t$ , and its value becomes nearly zero at most time  $t$ . The echo amplitude distribution was examined from the top at every measurement time, and the height  $y_2$  at which the echo amplitude exceeded the threshold at the beginning was defined as the interface 2.

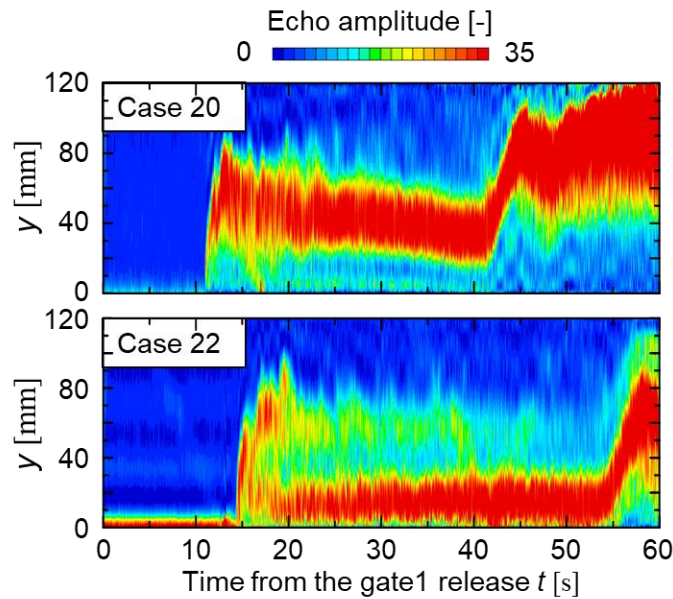


**Fig. 4-33** Spatio-temporal distributions of polynomial fitting results for echo amplitude, Case 20 is composed of lower quartz layer and upper opalin layer, Case 22 is composed of lower opalin layer and upper quartz layer

Using those threshold values  $T_1$  and  $T_2$  for the echo amplitude values, the two interfaces at each measurement time were detected and the results are shown in Fig. 4-34. The detected interfaces are shown on the timeline image at  $x = x_t$ . Comparing the detected interfaces with optical images, the interface 2 corresponding to the upper interface is in good agreement in both cases of 20 and 22. On

the other hand, there is room for discussion about the interface 1 corresponding to the lower interface. In particular, at around  $15 < t < 25$  mm in the Case 22, a discontinuous distribution about the height of the interface 1 determined from the echo amplitude is observed. Here, about the shape of the echo amplitude distributions, the existence distribution of opalin having a large diameter is dominant. That is, according to the above definition of  $T_1$ , it is possible to indicate the lower limit of the height at which the opalin exists in the upper layer for the Case 20 and the upper limit of the height at which the opalin exists in the lower layer for the Case 22. Considering this characteristic, the distribution at around  $15 < t < 25$  mm in the Case 22 shows that the rolling-up head region of the currents is composed of not only the upper layer but also the lower layer.

Additionally, these results can support qualitatively the rough validation of the density distribution shown in Fig. 4-12 estimated from the echo amplitude obtained by UVP. In that density distribution, the head region and the lower body region has relatively large values of the density, and near the upper boundary region at about  $25 < t < 40$  s also shows a large value sparsely. Such high-density values near the upper boundary seem related to the rolling-up structure in the head region. Namely, the distribution is attributed to the raised high-density fluid which is transported from near the bed to the upper boundary region. That hypothesis can explain the tendency of the density distribution shown in Fig. 4-12.

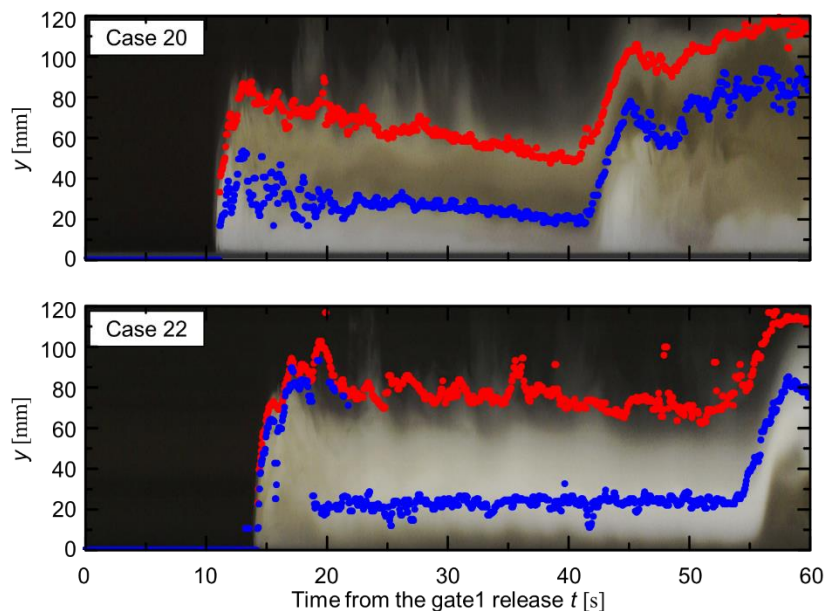


**Fig. 4-34** Distributions of the detected two interfaces using echo amplitude values, Case 20 is composed of lower quartz layer and upper opalin layer, Case 22 is composed of lower opalin layer and upper quartz layer

#### 4.3.4. Summary of flow behaviors in the some kinds of turbidity currents

This part summarizes the comparison of the flow behaviors between the quartz-laden currents, opalin-laden currents, and two-layer currents.

In the discussion about the front velocity  $U_f$ , it is revealed that the quartz-laden currents propagate faster than the opalin-laden currents with the same initial density  $\rho_H$  as a particle-suspended fluid. In addition, in cases of two-layer currents, the bottom layer is dominant to determine the  $U_f$ . In all conditions, the friction coefficient  $C_f$  shows values of around 0.0260 in the case that the maximum horizontal velocity  $u_{\max}$  in the body region is used for normalization, because the relation of  $u^* / u_{\max} \approx 0.114$  is confirmed in these experimental cases.

Using echo amplitude distributions, it becomes possible to detect two interfaces, because the scattering intensity in the cases of Rayleigh scattering reflected by the fine particles varies depending on the diameter of the particles. In this study, therefore, the echo amplitude values based on the scattering by the opalin particles are larger than that by the quartz particles. Considering the results obtained from the interfaces distribution in Case 22, the rolled-up structure can be observed in the head region and it is revealed that the head is composed of not only upper layer but also lower layer as shown in Fig. 4-35(a). This tendency can be mentioned in the study of Gladstone *et al.* (2004), although their study focused on the saline density currents. As shown in Fig. 1-2, the lower layer and the upper layer mix in case of the dimensionless density ratio between the layers  $\rho^* \approx 0.5$  like these experimental cases. On the other hand, the dimensionless density ratio of the Case 24 is  $\rho^* \approx 0.25$ , which means that the density difference between the two layers is larger than in the Case 22. In such a case, the lower layer propagates much faster than the lower layer, so the mixing of the two layers cannot be confirmed in the head region as shown in Fig. 4-35(b).

At the bottom, the lower layer plays a major role in determining the friction occurring between the lower layer and the bed. Furthermore, near the head region of currents, there is an interaction between the current and the ambient fluid, water. As a result of the rolled-up structure like shown in Fig. 4-35, only the lower layer is related to the most of these interactions. Therefore, in a discussion of front velocity and friction acting on the bed, it is determined by the kind of the lower layer. This hypothesis well describes the obtained experimental results. Under these experimental conditions, it is considered that the front velocity is not so influenced by the interaction based on the K-H instability seen near the upper boundary.

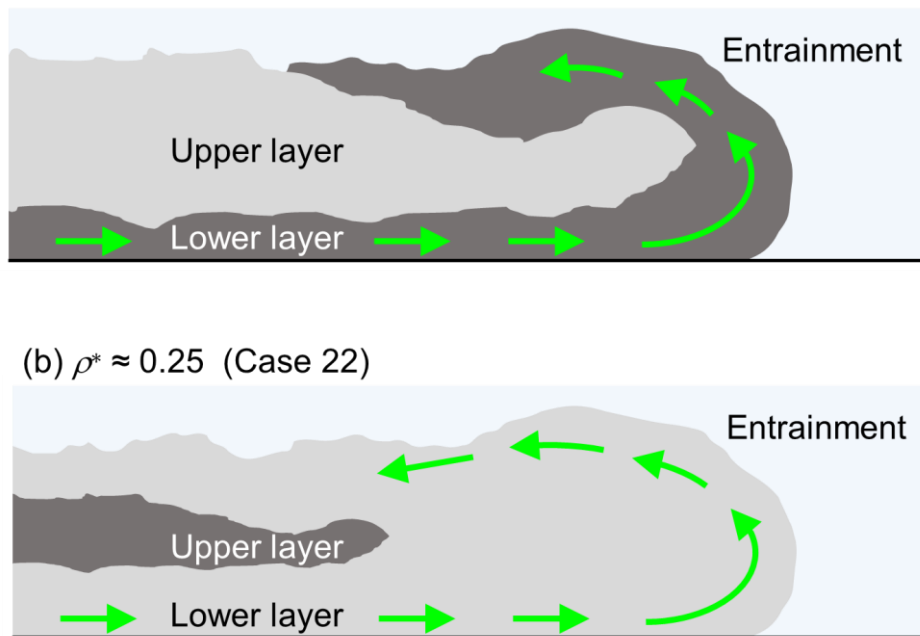


**Fig. 4-35** Schematic drawing of the flow behavior in case the two-layer turbidity currents, (a) in case of  $\rho^* \approx 0.5$  and (b) in case of  $\rho^* \approx 0.25$

## 5. Conclusion

This study was carried out for elucidating the long-distance propagation mechanism of turbidity currents, which are sediment-gravity flows and driven by the density difference between particle-suspended fluid and ambient fluid. Such turbidity currents have complicated inner flow structures and they cannot be measured by optical approaches because of their opacity. In order to evaluate their flow behaviors quantitatively, it was required to expand the utility of ultrasonic measurement techniques to be applied to solid-liquid two-phase flows. The conclusion about results and knowledge obtained in this study are summarized below.

### Ultrasonic measurement technique

- Ultrasonic velocity profiler (UVP) was applied to the measurements for particle-laden flows. The diameter of suspended particles  $d$  was order of  $10\ \mu\text{m}$  and the volume fraction of particles  $\alpha$  was in range of  $0.01 < \alpha < 15\%$ . This condition is difficult for UVP measurement to work well, because the size of  $d$  is too small to work as a reflector of ultrasonic waves with 4 MHz in basic frequency in water and large volume fraction promotes attenuation of the ultrasonic waves. Nevertheless, in case of quartz particles with  $12.2\ \mu\text{m}$  in center diameter, the reasonable velocity distributions could be measured by UVP in  $0.1 < \alpha < 5\%$ .
- Use of a pair of UVPs makes it possible to obtain both velocity components of horizontal  $u$  and vertical  $v$ . In addition to that, this study suggested the time-correction method at each measurement position using representative velocity.
- When the particle diameter  $d$  is much smaller than wavelength of ultrasound  $\lambda$  ( $d / \lambda \ll 1$ ), Rayleigh scattering, which is almost isotropic scattering, occurs. In such a case, the estimation of particle volume fraction was examined in this study. The novelty of this method is that echo obtained by UVP was applied to experimental turbidity current and boundary condition was modified for turbidity currents. Although highly accurate measurement results have not yet been obtained, it seems to become of great help for the elucidation of the flow structures of solid-liquid two-phase flow.
- In the condition of  $d / \lambda \ll 1$ , scattering intensity increases as the diameter of suspended particles becomes larger. Using this property, in cases of two-layer turbidity currents, it was successful to detect two interfaces of ambient fluid-upper layer and upper layer-lower layer.

### Flow structures of gravity currents

- A quantitative method to track the head positions of the gravity currents using the pattern matching method for consecutive experimental images was established, and the front velocity  $U_f$ , which is the advection velocity of the current, was calculated for each experiment. As the results,

it was found that the turbidity currents containing quartz particles propagates 19.0% faster than the saline density currents, for the same initial density. Additionally, the turbidity currents containing quartz particles propagates 38.5% faster than turbidity currents containing opalin particles. From this, it was confirmed that the front velocity  $U_f$  varies greatly due to the interaction caused by the suspended particles.

- The flow structure of the turbidity currents containing quartz particles and the saline density currents were compared. Comparing the height of the two gravity currents in the body region, it was found that the height of the turbidity current was lower. This is because the diffusion is predominant in the density current, whereas, in case of the turbidity current, settling of the particles is also included. As the results, the distribution of the velocity fluctuation component greatly changed. In case of the turbidity current, large fluctuation occurred at  $y > h_m$ , but in case of the density current, the tendency was reversed. From this, it is thought that the existence of the particles suppresses the velocity fluctuations in the vicinity of the bed. Besides, the particles are mixed by the turbulent velocity fluctuations in the region above that ( $y < h_m$ ). That mixing acts as an effect giving potential energy to particles, namely the supplemental driving force is supplied for the current, because the density difference is kept. That is why, despite the fact that the friction coefficient  $C_f$  is smaller in case of the density current, the turbidity current can propagate faster than the density current.
- Flow behavior of the turbidity current containing quartz particles as the solid–liquid two–phase flow was analyzed, using momentum conservation equation in the body region. From the calculated results of each shear stress distribution, it was found that viscous stress  $\frac{d\mu_H u}{dy}$  and Reynolds shear stress  $-\rho_H \overline{u'v'}$  are dominant as in cases of single–phase flows. In cases of the turbidity current, because the volume fraction  $\alpha$  of quartz particles is small, the value of  $-\rho_H \overline{v'u'}$  was found to be sufficiently smaller than  $-\rho_H \overline{u'v'}$ . On the other hand, it was confirmed that since the  $\frac{d\mu_H u}{dy}$  and  $-\rho_H \overline{u'v'}$  are canceled out at outside the bottom and the upper boundary, the pressure gradient hardly acts. Namely, a negative momentum transfer against the mean velocity gradient, which is working to keep a stable stratification, is confirmed in the outer region ( $y > h_m$ ) of the body region. It is expected that the particles are being mixed by the velocity fluctuation components, that suppresses the settling of the suspended particles and to keep  $\rho_H$  at a roughly constant value.
- Analysis of two-layer turbidity currents showed that the type of particles suspended in the lower



layer determines the front velocity  $U_f$ , when the bulk density  $\rho_H$  as initial condition is equal. In the two-layer turbidity currents composed of different kinds of particle-suspended fluid, it was confirmed that the lower layer was rolled up in the head region and the upper layer was wrapped. Therefore, in these conditions, not only the friction with the bed but also the interaction with the ambient fluid in the vicinity of the head is dominated by the lower layer. From this, it was found that the front velocity  $U_f$  was determined by the friction at the bottom and the interaction at the head region, and the influence of shear flow at the upper boundary in the body region does not work much.

- In cases of the turbidity currents, it was confirmed that the relationship between the friction velocity  $u^*$  and the maximum velocity  $u_{\max}$  in the body region was  $u^*/u_{\max} \approx 0.114$  in every experimental case. It was also confirmed that the friction coefficient  $C_f \approx 0.0260$  was obtained using this relationship, the obtained values of  $C_f$  are one order larger than that measured in gas-liquid two-phase flows.

## 6. Bibliography

- Altinakar, M. S., Graf, W. H., Hopfinger, E. J., "Flow structure in turbidity currents." *Journal of Hydraulic Research* 34.5 (1996): 713-718.
- Azpiroz-Zabala, M., *et al.* "Newly recognized turbidity current structure can explain prolonged flushing of submarine canyons." *Science advances* 3.10 (2017): e1700200.
- Barr, D. I. H. "Densimetric exchange flow in rectangular channels III. Large scale experiments." *La Houille Blanche* 22 (1967): 619-632.
- Cesare, G. D., Anton, S., Felix, H., "Impact of turbidity currents on reservoir sedimentation." *Journal of Hydraulic Engineering* 127.1 (2001): 6-16.
- Chamoun, S., Cesare, G. D., Schleiss, A. J., "Managing reservoir sedimentation by venting turbidity currents: A review." *International Journal of Sediment Research* 31.3 (2016): 195-204.
- Davidson, J. F., Harrison, D., Carvalho, J. R. F. G. D., "On the liquid like behavior of fluidized beds." *Annual Review of Fluid Mechanics* 9.1 (1977): 55-86.
- Dong, X., *et al.* "Oil–water two-phase flow velocity measurement with continuous wave ultrasound Doppler." *Chemical Engineering Science* 135 (2015): 155-165.
- Downing, A., Thorne, P. D., Vincent, C. E., "Backscattering from a suspension in the near field of a piston transducer." *The Journal of the Acoustical Society of America* 97.3 (1995): 1614-1620.
- Ellison, T. H., Turner, J. S., "Turbulent entrainment in stratified flows." *Journal of Fluid Mechanics* 6.3 (1959): 423-448.
- Fisher, F. H., Simmons, V. P. "Sound absorption in sea water." *The Journal of the Acoustical Society of America* 62.3 (1977): 558-564.
- Gladstone, C. *et al.*, "An experimental investigation of density-stratified inertial gravity currents." *Sedimentology* 51.4 (2004): 767-789.
- Guerrero, M., Vittorio, D. F., "Suspended sediment assessment by combining sound attenuation and backscatter measurements—analytical method and experimental validation." *Advances in Water Resources* 113 (2018): 167-179.
- Hitomi, J. *et al.* "Ultrasound Flow-Monitoring and Flow-Metering of Air-Oil-Water Three-Layer Pipe Flows." *IEEE Access* 5 (2017): 15021-15029.
- Hitomi, J., Nomura, S., Cesare, G. D., Takeda, Y., Park, H. J., Tasaka, Y., Murai, Y., "Flow Monitoring of Particle-laden Flows Combining Ultrasonic Doppler and Echo Intensity Profiling Techniques.", Proc. of the 11th International Symposium on Ultrasonic Doppler Methods for Fluid Mechanics and Fluid Engineering 11th ISUD, September 5-7, (2018), Berlin, Germany, pp. 75-78
- Jamshidnia, H., Takeda, Y., "An experimental study of the effect of a baffle on the flow structure in a rectangular open channel using UVP." *Journal of Fluid Science and Technology* 5.3 (2010):



542-557.

- Kang, L., Feeney, A., Dixon, S., "Flow measurement based on two-dimensional flexural ultrasonic phased arrays." *Proceedings of Meetings on Acoustics 6ICU*. Vol. 32. No. 1. ASA, 2017.
- Keulegan, G. H., "An experimental study of the motion of saline water from locks into fresh water channels." *Nat. Bur. Stand. Rept. Technical Report 5168* (1957).
- 木田 重雄, 柳瀬 眞一郎. 乱流力学. 朝倉書店, 1999.
- Kikura, H., Hamdani, A., Ihara, T., "Development of Two-dimensional Vector UVP with Phased Array." *Development* 28 (2016): 30.
- Kitagawa, A., Murai, Y., Yamamoto, F., "Two-way coupling of Eulerian–Lagrangian model for dispersed multiphase flows using filtering functions." *International journal of multiphase flow* 27.12 (2001): 2129-2153.
- 北浦秀和, 村井祐一, and 武田靖. "UVP による渦輪の速度ベクトル場の計測 (流体力学, 流体機械)." *日本機械学会論文集 B 編* 76.772 (2010): 2143-2151.
- Kneller, B. C., Bennett, S. J., & McCaffrey, W. D., "Velocity structure, turbulence and fluid stresses in experimental gravity currents. " *Journal of Geophysical Research: Oceans*, 104(C3) (1999), 5381-5391.
- Kneller, B., & Buckee, C., "The structure and fluid mechanics of turbidity currents: a review of some recent studies and their geological implications. " *Sedimentology*, 47 (2000), 62-94.
- Komori, S. *et al.* "Turbulence structure in stably stratified open-channel flow." *Journal of Fluid Mechanics* 130 (1983): 13-26.
- Lee, T. H., & Hanes, D. M., "Explicit solution to the acoustic backscatter equation to measure the concentration of uniform, suspended particles. " *Journal of Geophysical Research*, 100(C2) (1995), 2649-2657.
- Longo, S., *et al.* "Gravity currents produced by constant and time varying inflow in a circular cross-section channel: Experiments and theory." *Advances in Water Resources* 90 (2016): 10-23.
- Malvern S. A., "Operational qualification for Mastersizer 3000 (MAZ3000) optical bench", 2013.
- Middleton, G. V. "Sediment deposition from turbidity currents." *Annual review of earth and planetary sciences* 21.1 (1993): 89-114.
- Middleton, G. V. "Experiments on density and turbidity currents: I. Motion of the head." *Canadian Journal of Earth Sciences* 3.4 (1966): 523-546.
- Murai, Y., Matsumoto, Y., "Numerical study of the three-dimensional structure of a bubble plume." *Journal of fluids engineering* 122.4 (2000): 754-760.
- Murai, Y. *et al.* "Turbulent shear stress profiles in a bubbly channel flow assessed by particle tracking velocimetry." *Experiments in Fluids* 41.2 (2006): 343.
- Murai, Y. *et al.* "Skin friction reduction by large air bubbles in a horizontal channel flow." *International journal of multiphase flow* 33.2 (2007): 147-163.



- Murai, Y. *et al.* "Development of an ultrasonic void fraction profiler." *Measurement Science and Technology* 20.11 (2009): 114003.
- Murai, Y. *et al.* "Ultrasonic detection of moving interfaces in gas–liquid two-phase flow." *Flow Measurement and Instrumentation* 21.3 (2010): 356-366.
- Murakawa, H., Kikura, H., Aritomi, M., "Application of ultrasonic multi-wave method for two-phase bubbly and slug flows." *Flow measurement and instrumentation* 19.3-4 (2008): 205-213.
- Nogueira, H. I., Adduce, C., Alves, E., Franca, M. J., "Image analysis technique applied to lock-exchange gravity currents." *Measurement Science and Technology* 24.4 (2013): 047001.
- Nomura, S. *et al.* "Sediment mass movement of a particle-laden turbidity current based on ultrasound velocity profiling and the distribution of sediment concentration." *Geological Society, London, Special Publications* 477 (2018a): SP477-19.
- Nomura, S., Hitomi, J., Cesare, G. D., Murai, Y., Tasaka, Y., Takeda, Y., and Sakaguchi, H., "Instantaneous Flow Vector Measurement by a Pair of Ultrasound Doppler Instruments. ", Proc. of the 11th International Symposium on Ultrasonic Doppler Methods for Fluid Mechanics and Fluid Engineering 11th ISUD, September 5-7, (2018b), Berlin, Germany, pp. 119-122
- Oehy, C. D., Cesare, G. D., Schleiss, A. J., "Effect of inclined jet screen on turbidity current." *Journal of Hydraulic Research* 48.1 (2010): 81-90.
- Park, H. J., Tasaka, Y., Murai, Y., "Bubbly drag reduction accompanied by void wave generation inside turbulent boundary layers." *Experiments in Fluids* 59.11 (2018): 166.
- Parker, G., Fukushima, Y., Pantin, H. M., "Self-accelerating turbidity currents." *Journal of Fluid Mechanics* 171 (1986): 145-181.
- Pedocchi, F., García, M. H., "Acoustic measurement of suspended sediment concentration profiles in an oscillatory boundary layer." *Continental Shelf Research* 46 (2012): 87-95.
- Piccirillo, P., van Atta, C. W., "The evolution of a uniformly sheared thermally stratified turbulent flow." *Journal of Fluid Mechanics* 334 (1997): 61-86.
- Poelma, C., "Ultrasound imaging velocimetry: a review." *Experiments in Fluids* 58.1 (2017): 3.
- Povey, M. J., *Ultrasonic techniques for fluids characterization*. Elsevier, 1997.
- Shi, X., *et al.* "Oil-gas-water three-phase flow characterization and velocity measurement based on time-frequency decomposition." *International Journal of Multiphase Flow* 111 (2019): 219-231.
- Simpson, J. E., Britter, R. E. "The dynamics of the head of a gravity current advancing over a horizontal surface." *Journal of Fluid Mechanics* 94.3 (1979): 477-495.
- Su, Q., Chao, T., Feng, D., "Mechanism modeling for phase fraction measurement with ultrasound attenuation in oil–water two-phase flow." *Measurement Science and Technology* 28.3 (2017): 035304.
- Symons, W. O., *et al.* "A new model for turbidity current behavior based on integration of flow monitoring and precision coring in a submarine canyon." *Geology* 45.4 (2017): 367-370.



- Taishi, T., Kikura, H., Aritomi, M., "Effect of the measurement volume in turbulent pipe flow measurement by the ultrasonic velocity profile method (mean velocity profile and Reynolds stress measurement)." *Experiments in Fluids* 32.2 (2002): 188-196.
- Takeda, Y., ed. Ultrasonic Doppler velocity profiler for fluid flow. Vol. 101. Springer Science & Business Media, 2012.
- Theiler, Q., Franca, M. J. "Contained density currents with high volume of release." *Sedimentology* 63.6 (2016): 1820-1842.
- Thorne, P. D., Hanes, D. M., "A review of acoustic measurement of small-scale sediment processes." *Continental shelf research* 22.4 (2002): 603-632.
- Zheng, H., *et al.* "Real time multicomponent echo particle image velocimetry technique for opaque flow imaging." *Applied physics letters* 88.26 (2006): 261915.
- Zordan, J., Schleiss, A. J., Franca, M. J. "Structure of a dense release produced by varying initial conditions." *Environmental Fluid Mechanics* (2018): 1-19.



## Acknowledgements

この卒業論文を完成させるまでには、多くの皆様のご協力・ご支援をいただきました。ここで、感謝の意を示させていただきます。

村井祐一教授には、研究の奥深さや面白さ、難しさを徹底的に教えていただきました。研究に関する相談をさせていただく度に、当然のことながら「自分はまだまだ追いつけないな」と感じるばかりでした。それでも、何とかその差を縮めようともがいていた期間こそが、今振り返ってみると、私を大きく成長させてくれたと感じています。また、学会発表や海外インターンシップ、論文執筆等、まだまだ未熟な私に対して、数多くの貴重な経験をさせていただきありがとうございます。何事にも前向きに挑戦するという心構えを持てるようになりました。

田坂裕司准教授には、研究内容に関しては勿論のこと、英文執筆の際にも熱心な指導をしていただきました。研究発表や文章の添削をお願いした際には、私の稚拙な表現にもかかわらず、その意図をくみ取り、より良い表現方法を提案してくださいました。今でも私は、英語での表現には不安が残りますが、先生の熱心なご指導によって恐怖心を払拭することができました。また、研究面だけでなく、音楽のこと、スポーツのこと、自動車のこと、お子さんのこと等、多くのお話を聞かせていただき、楽しませていただきました。今後とも、先生の間人味溢れるご指導を続けていただきたいと思います。

朴炫珍助教授には、日常的に計測技術に関する相談に乗っていただきました。特に私の場合は、超音波計測がメインだったので、それに関して多くを教えていただきました。LFCのように実験系の研究室では、計測機器の取り扱いが、研究の善し悪しを決定づける大きな要素です。そのため、教えていただいた多くの超音波に関する知識は、実際に実験を行うときだけでなく、解析をする際にも大いに活用させていただきました。

山保敏幸技官には、実験装置の改良の際に大変お世話になりました。学部4年生の段階で既に、素晴らしい“シーソー装置”を作っていただきました。おかげさまで、その研究は論文にまとめることができ、修士課程のほとんどはスイスでの実験メインになりました。そのため、本格的な実験装置の作成をお願いする機会が無く、少し寂しい気持ちでした。それでも、装置に合わせた円筒形の亚克力部品が必要な旨をお話しした際には、翌日に完成させて持ってきてくださいました。やはり、山保さんの技術こそがLFCの研究実績を支える大きな核になっていることを改めて実感した瞬間でした。今後とも、お身体を大切になさってください。また、私が再び研究室を訪れた際には、自動車関係のお話をさせていただければ幸いです。

秘書の宮崎優衣さんには、学会参加や短期雇用関連、その他の事務的な手続き等で、大変お世話になりました。学部生の時には分からなかったのですが、修士課程になり、多くの出張等を経験させていただくうちに、宮崎さんの行う仕事の量とその早さに驚かすにはいられてませんでした。また、そのようなお忙しい中でも、会議室の確保や書類関連の相談をさせ



ていただいた際には、快く対応していただきました。おかげさまで、私は研究活動に集中することができました。時には、野球の話で楽しませていただきました。また改めて日ハムの最新情報を聞かせていただくのを楽しみにしております。

野村瞬博士には、修士課程の研究で特にお世話になりました。「乱泥流」という研究テーマに対して、二人で試行錯誤しながら実験を行い、解析し、議論をして改善を繰り返した日々は忘れられません。ローザンヌの EPFL の駅で初めて会った時から、気さくに話しかけてくださり、私も楽しい時間を多く共有させていただきました。研究だけでなく、旅行や食事にも幾度となく誘っていただき、大変感謝しております。二人で計測した乱泥流の研究成果、並びに、JAMSTEC と LFC の共同研究のより一層の発展を願っております。また、ご家族の皆さんにもご挨拶に伺わせていただくのを楽しみにしております。

Dear Prof. De Cesare Giovanni: Thanks to your kind cooperation and many supports, I could have a good opportunity to study in LCH and to spend a precious time in Lausanne. You look so fun always and have a sense of humor, so I really enjoyed researching turbidity currents and discussing the analysis data with you. My dream is not only to bring the fruits of research on turbidity currents, but also to improve my English skill and to make a joke with you. I am looking forward to seeing you again.

武田靖教授には、乱泥流研究で大変お世話になりました。私が EPFL でインターンシップを行っている際には、何度もローザンヌまで足を運んでいただき、研究に関する議論をさせていただきました。「一見何も見えないと思いついて入っている実験動画でも、よく見ると流れの構造が表れている」というお言葉をいただいてから、私は計測手法だけでなく、流体力学に向き合いたいと思うようになりました。乱泥流プロジェクトは、工学部の知見を活かして、新たな切り口から流れの内部構造を明らかにするという趣旨があります。そういった挑戦的なテーマに取り組むきっかけを与えてくださり、ありがとうございました。

LFC の先輩方、同期の皆、後輩達にも感謝をしています。研究に行き詰った際には相談に乗ってくれたり、文章の書き方や発表の仕方に関して丁寧な指導をしてくれたりと、とても頼りがいのある LFC の先輩方を見てきました。いざ自分がその立場になって、しっかりと先輩としての役割を果たせたかは分かりません。それでも、一生懸命に研究に取り組む後輩達の姿は、私の研究に対するモチベーションに火をつけてくれましたし、研究以外の場面でも、楽しい時間を共有してくれました。さらに、個性あふれる同期の存在は、「ああ、自分は自分のスタイルを貫けばいいんだな」と常に背中を押してくれるものでした。多様性に富んだ研究室の皆さんと、流体力学のテーマに対して真っ向から挑戦した期間は、私を大きく成長させてくれました。

こうして振り返ってみると、多くの方々に支えられて、研究活動を行って来たことを実感しました。上に挙げた方々だけでなく、見守ってくれた家族であったり、意見交換をさせていただいた多くの研究者の方々であったり、関わってくださった皆さんに感謝の気持ちを



示したいと思います。そして、LFC で培ったチャレンジ精神は、来年度からは社会人として発揮していけるよう頑張っていきたいと思います。皆さんの益々のご活躍を祈っております。大変、お世話になりました。

人見純平

2019年2月21日



## List of publications

- Journal

- (1) [J. Hitomi](#), Y. Murai, H.J. Park, Y. Tasaka, “Ultrasound flow-monitoring and flow-metering of air–oil–water three-layer pipe flows”, *IEEE Access*, Vol.5, No.1 (2017), pp.15021-15029, DOI10.1109/ACCESS.2017.2724300 (**Impact Factor =3.557**)

- International conference

- (1) Y. Murai, [J. Hitomi](#), H.J. Park, Y. Tasaka, “Ultrasound Doppler velocimetry applied for air-oil-water three-phase pipe flows in slugging regime”, *Proc. 11th Japan-U.S. Seminar on Two-Phase Flow Dynamics*, (2017), pp.121-124.
- (2) S. Nomura, [J. Hitomi](#), G. De Cesare, Y. Takeda, Y. Yamamoto, H. Sakaguchi, “Sediment mass movement of a particle-laden turbidity current based on ultrasound velocity profiling and the distribution of sediment concentration”, *Geological Society London Special Publications*, (2018), 477
- (3) S. Nomura, G. De Cesare, [J. Hitomi](#), Y. Takeda, Y. Tasaka, Y. Murai, H. Sakaguchi, “Velocity and concentration distribution of saline density and turbidity current”, *Proc. 5th IAHR Europe Congress - New Challenges in Hydraulic Research and Engineering* (2018).
- (4) D. Noto, [J. Hitomi](#), H.J. Park, Y. Tasaka, Y. Murai, “A proposal of a novel flow visualization method using rheoscopic fluid”, *Proc. 8th ETH-HU Academic Exchange and Collaborative Research* (AECOR8), (2018), pp.9-9.
- (5) [J. Hitomi](#), S. Nomura, G. De Cesare, Y. Takeda, H. J., Y. Tasaka, Y. Murai, “Flow Monitoring of Particle-laden Flows Combining Ultrasonic Doppler and Echo Intensity Profiling Techniques”, *Proc. of the 11th International Symposium on Ultrasonic Doppler Methods for Fluid Mechanics and Fluid Engineering* 11th ISUD, (2018), pp. 75-78
- (6) S. Nomura, [J. Hitomi](#), G. De Cesare, Y. Murai, Y. Tasaka, Y. Takeda, H. Sakaguchi, “Instantaneous Flow Vector Measurement by a Pair of Ultrasound Doppler Instruments”, *Proc. of the 11th International Symposium on Ultrasonic Doppler Methods for Fluid Mechanics and Fluid Engineering 11th ISUD*, (2018), pp. 119-122
- (7) [J. Hitomi](#), S. Nomura, G. De Cesare, Y. Takeda, H.J. Park, Y. Tasaka, Y. Murai, “Comparison of flow behaviors between experimental turbidity currents and saline density currents combining ultrasonic and optical techniques”, *Proc. 8th ETH-HU Academic Exchange and Collaborative Research* (AECOR8), (2018), pp.10-10.
- (8) S. Nomura, [J. Hitomi](#), G. De Cesare, Y. Takeda, “Steady state in experimentally produced turbidity current under a large amount of suspension supply”, *EGU General Assembly 2019*, (7–12 April, 2019).



● Domestic conference (in Japan)

- (1) ○人見純平, 朴 炫珍, 田坂裕司, 村井祐一, “UVP を用いた管内水・油・空気層状流の流量計測”, *第45回可視化情報シンポジウム*, (2017), Vol. 38, Suppl. No.1, A101, pp.1-5.
- (2) ○人見純平, 野村瞬, De Cesare Giovanni, 武田靖, 阪口秀, 朴炫珍, 田坂裕司, 村井祐一, “UVP を用いた乱泥流の構造解析手法の確立”, *可視化情報全国講演会(室蘭2017)*, (2017), No. OS4-1, pp.1-5.
- (3) ○澤田航希, 人見純平, 芳田泰基, 朴炫珍, 田坂裕司, 村井祐一, “エコー強度情報を用いた超音波流速分布計の多成分化”, *日本機械学会北海道学生会 第47回学生員卒業研究発表講演会*, (2018), 317.
- (4) ○人見純平, 野村瞬, De Cesare Giovanni, 武田靖, 朴炫珍, 田坂裕司, 村井祐一, “乱泥流内粒子群運動の超音波による定量計測”, *混相流シンポジウム 2018*, (2018), No. 0059, pp.1-2. (ベストプレゼンテーション賞受賞)
- (5) ○李瑞雪, 芳田泰基, 人見純平, 澤田航希, 朴炫珍, 田坂裕司, 村井祐一, Stéphane Fischer, “ステンレス管内を流れる乳製品の超音波診断”, *日本機械学会第96期流体力学部門講演会*, (2018), AM5-OS4-1, pp.1-3.
- (6) ○赤坂信太郎, 人見純平, 澤田航希, 朴炫珍, 田坂 裕司, 村井 祐一, “超音波パルスエコーグラフィによる気液二相チャネル流の高時間分解計測”, *日本機械学会北海道学生会 第48回学生員卒業研究発表講演会*, (2019年3月)

Received March 31, 2017, accepted June 6, 2017, date of publication July 11, 2017, date of current version August 22, 2017.

Digital Object Identifier 10.1109/ACCESS.2017.2724300

# Ultrasound Flow-Monitoring and Flow-Metering of Air–Oil–Water Three-Layer Pipe Flows

JUNPEI HITOMI, YUICHI MURAI, HYUN JIN PARK, AND YUJI TASAKA

Laboratory for Flow Control, Division of Energy and Environmental Systems, Faculty of Engineering, Hokkaido University, Sapporo 060-8628, Japan

Corresponding author: Yuichi Murai (murai@eng.hokudai.ac.jp)

**ABSTRACT** The combined use of ultrasound pulse-echo intensity and Doppler shift frequency is examined as a means to measure strong unsteady three-phase pipe flows of a gas and two liquids. With air, oil, and water as components of the fluid media, particular attention is given to analyze ultrasound responses at the air–oil and oil–water interfaces. Reciprocating slugging is generated inside a 55-mm-diameter circular pipe, of which edges oscillate vertically at a controlled frequency. We use an ultrasound velocity profiler to obtain the 1-D cross-sectional distributions of the instantaneous flow velocity at the sampling rate of 60 Hz. All the measurements are realized by a single ultrasound transducer located outside the pipe. Measurement accuracy is validated using a high-speed camera coupled with particle image velocimetry that is synchronized with the profiler. The results demonstrate that the proposed technique works properly in sensing both interfaces as well as in-phase flow velocity distributions. In addition, multiphase volume flow rates for the constituents are obtained by velocity profile integration assuming vertical phase stratification in an approximation.

**INDEX TERMS** Doppler method, flow metering, multiphase flow, particle image velocimetry, pipe flow, pipe line, ultrasound

## I. INTRODUCTION

Using ultrasound Doppler information for flow metering is a non-invasive, first-principle-based measurement [1]. The volume flow rate is directly given by area integration of the spatial distribution of the velocity within a target plane. Distinct from ordinary indirect flow-metering devices, no calibration is required preliminarily because of the capability of velocity distributions [2]. This feature enables the target of flow metering to be expanded widely such as for curved flows [3], non-Newtonian flows [4]–[6], and for multiphase flows [7]–[19]. In particular, the application to multiphase flow is challenging. Conventional approaches to flow metering of multiphase flows are such that an individual phase needs to be sufficiently separated for the metering device to be effective. Alternatively, homogeneous mixing allows the devices to approximate the flow rate [20]. However, such phase-control operations require a change in pipeline systems and invariably experiences a significant pressure loss. Therefore, for large systems such as in power and chemical plants, a non-invasive approach along with related technology to monitor directly internal multiphase flows is keenly waited to be developed.

To handle the strong unsteady three dimensionality of multiphase pipe flows in the measurement section, several strategies are now being developed such as by electric

capacitance [21], [22], by optical rays [23], [24], and acoustic approaches. Among various non-invasive monitoring principles, ultrasound has multiple advantages in comparison with others. One is access to opaque fluids such as chemical solutions, fuel oils, and their suspensions. Another is spatial resolution, which suffices to monitor internal flow structures with a control of basic wavelength of ultrasound. As the sensors can be located outside the pipe, portability and easy-to-mount operation are further additional benefits to consider wide industrial applications. The known disadvantage, conversely, is the damping of weak ultrasound pulses during propagation in fluid media. Users should also take care of acoustic noise from multiple reflections of pulses in the acoustic environment around the measurement section.

In our previous series of developments, we found how to extract position of the fluid–fluid interface from the ultrasound pulse waveform in echoes from multiphase flows. For gas–liquid combinations, three kinds of waveform analysis were proposed to obtain automated interfacial detection [15]. Based on the technique, we also developed an ultrasound void-fraction profiler [11] and ultrasound viscometry [17] for bubbly two-phase flow regimes. In the present work, we apply such ultrasonic sensing to three-phase pipe flows of gas–liquid–liquid stratifications. The demand for three-phase flow measurements have risen in the fuel pipe line industry

where oil and water co-flow with a gas component. Such flows have a contrasting variety of flow patterns depending on the combination of three flow rates. The local flow structure must be monitored for stable continuous fuel transport as well as security from the risk of pulsatile behavior. Similar issues exist in chemical plants that handle complex multiphase flows consisting of phases of largely different properties.

To meet these demands, we investigated specifically air–oil–water pipe flows to assess whether the ultrasound pulse technique is applicable. For the platform of experimentation, a seesaw type of oscillating three-phase pipe flow system was built (Fig. 1). Using this system, we obtained multiple interface echoes from a single sequence of ultrasound pulse emissions, and in-phase velocity profiling. From echo intensities and Doppler frequencies, we were able to examine flow metering to estimate the volume flow rates of each phase. The accuracy of the method is validated by particle image velocimetry enabling measurement error to be evaluated and the dynamics of three-phase pipe flows to be quantified.

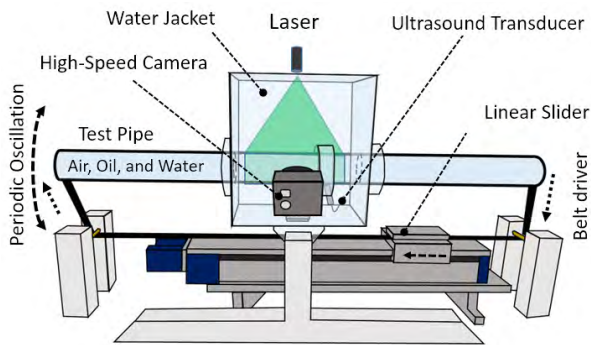


**FIGURE 1.** Seesaw-driven multiphase pipe flow facility. Three phases are filled in the pipe with end plates on both edges, and oscillated by a single belt connected with a computer controlled linear slider. UVP and high-speed video imaging are conducted on the oscillation frame.

## II. EXPERIMENTATION PLATFORM

For the seesaw-driven facility (Fig. 1), the pipe diameter and length are  $D = 55$  mm, and  $L = 1000$  mm, respectively. To record the flow optically the pipe was made of transparent acrylic resin.

Both ends of the pipe are connected to a single moving belt driven by a motor linear slider. The motion of this slider is controlled by a PC, which regulates the amplitude and frequency of the pipe ends. The maximum amplitude and frequency are 200 mm and 1.0 Hz. Air, oil, and water enter the pipe at the laboratory temperature of 25 °C. The test oil was Silicone oil of kinematic viscosity 10 cSt and density of 935 kg/m<sup>3</sup> and is immiscible with water.

### A. ULTRASOUND INSTRUMENTATION

Three kinds of measurement instrumentation were introduced to the platform providing ultrasound monitoring, backlight visualization, and laser sheet illumination.

For ultrasound monitoring, an ultrasound transducer is set beneath the pipe at 15° to the pipe cross sectional plane.

The transducer is submerged in a water jacket so that the propagation of the pulse into the pipe interior is easier as well as its return echo to the transducer. The water jacket is a cubic buffer tank with side length of 255 mm, sufficient to eliminate ultrasound residuals from around as the measurement section is monitored at 2 kHz in pulse repetition frequency. The transducer emits and receives periodic ultrasound pulse of 4 MHz in basic frequency. The nominal intensity of the emitted pulse is 150 V whereas the echo intensity level is only of an order of a few millivolts. The effective diameter of the ultrasound pulse is 5 mm. The cycle number of the pulse is set to 4. Therefore, the spatial resolution in water is estimated to be a 5 mm-diameter disk of thickness  $4[(1497 \text{ m/s}) / (4 \times 10^6 \text{ Hz})] / 2 = 0.75$  mm, where 1497 m/s is the speed of sound in the experiment. The temporal resolution is given by the sampling rate of Doppler velocity profiling in the ultrasound velocity profiling (UVP) operation, which is 60 Hz under present conditions.

### B. OPTICAL FLOW VISUALIZATION

To verify the ultrasound monitoring performance, two kinds of optical flow visualization were applied. One is backlight projection of the phase distribution [Fig. 2(a)], in which oil is dyed red, the dye being solvable in oil but insoluble in water. For water, aqueous green food dye was mixed in to identify the oil–water interface as contrast between red and green colors. Diffused white light of 650-W power illuminated the pipe from behind to enable a backlight color projection video image to be recorded. The camera was set up on the opposite side of the light source.

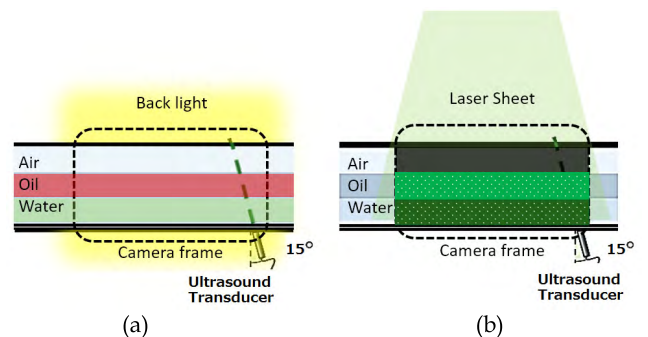


**FIGURE 2.** Methods for visualizing the flow: (a) white backlighting of dyed liquids to see the projection phase distributions, and (b) laser sheet illumination of central plane where UVP measurement line is applied.

The other is laser illumination of the oil and water phases for PIV measurements. For water, high-porous polymer particles were used as the tracers. The particles have a density of 1010 kg/m<sup>3</sup> and were 80 to 120 μm in diameter. For oil the tracers were water-repellent solid particles of density 920 kg/m<sup>3</sup> and peak diameter 110 μm. We observed that a small percentage of the particles adhered to the air–oil and the oil–water interfaces. Whereas the adhesion may change the interfacial property slightly, the Weber number (to be explained later) was kept high enough to have an

insignificant effect on the dynamic behavior of the three-phase flow. Moreover, the laser sheet scatters on the interfaces because of the adhesion, which assisted in viewing the two interfaces. The number density of tracer particles in each phase is guaranteed due to periodic wave-breaking generated on both interfaces during the oscillatory motion of the pipe.

Fig. 3 shows how each phase behaves during a single 5-s-period cycle of the seesaw motion of the pipe. Left and right rows correspond with rightward and leftward flows driven by the pipe inclination. Note that the camera is mounted on the same oscillation frame so that consecutive images depict interfacial motions relative to the pipe wall. The pipe-bulk volume fractions of air, oil, and water are set to 1/3. The oil layer produces a wave-breaking front that rapidly propagates in the air–oil interface at  $t = 1.0$  s and  $t = 3.5$  s. Water accelerates slowly with a time lag of  $t = 1.5$  s and  $t = 4.0$  s after wave propagation in the upper oil phase. During this cycle, capillary waves move along the oil–water interface due to shear stress transfer through the interface. Slightly dark spots observed along both interfaces indicate wavy surfaces that accompany three-dimensional interfacial structures. Apart from these spots, the main flow is confirmed to be approximately two-dimensional.

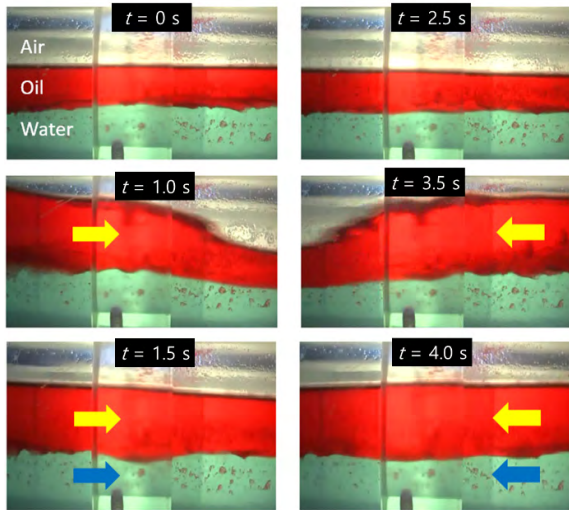


FIGURE 3. Cyclic behavior of the three-phase flow visualized using color projection in a single cycle of the pipe oscillation.

Fig. 4 presents the time-line image of the phase distribution, sampled from the video image. The sampling line is set vertically at the same position of the UVP measurement (to be described below). As the time-line image shows, the air–oil interface repeats a sharp rise and slow fall in every cycle whereas the oil–water interface fluctuates at a higher frequency but with small amplitude. With diverse combinations of volume ratios of air, oil, and water, many different types of interfacial behavior were observed. From these characteristics of the interfacial motion, ultrasound monitoring is examined.

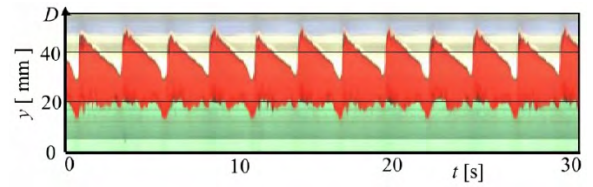


FIGURE 4. Time-line image of the three-phase flow at the central plane of the oscillating pipe, showing wavy passage of oil and water phases with different interfacial structures observed at the oscillation period of  $T = 5$  s.

Fig. 5 presents the same time sequence of tracer particle images illuminated by a laser sheet. These images are processed by PIV software to verify the results from ultrasound measurements.

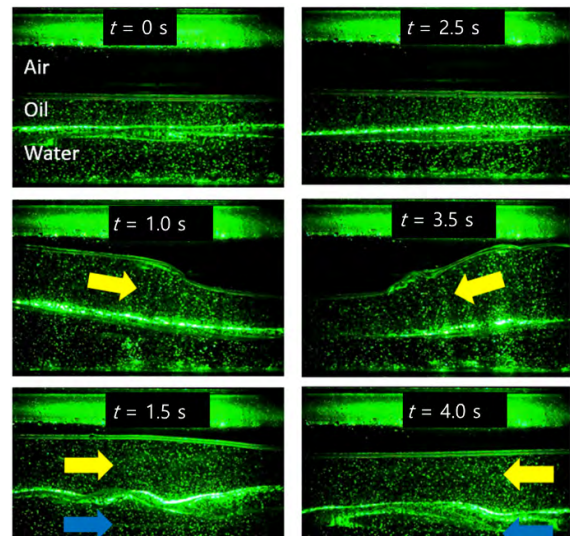


FIGURE 5. Particle images for PIV measurements, in which fluid interfaces at the central plane are also visualized.

### III. RESULTS AND DISCUSSION

To analyze the data, for the oscillating three-phase pipe flow, dimensionless parameters are introduced:

$$Re_j = \frac{\rho_j D U}{\mu_j}, \quad j = \{a, o, w\}, \quad (1)$$

$$Fr_{jk} = \frac{U}{\sqrt{g D (\Delta \rho_{jk} / \rho_j)}}, \quad jk = \{a/o, o/w\} \quad (2)$$

$$We_{jk} = \frac{\rho_j U D}{\sigma_{jk}}, \quad (3)$$

where  $D$  and  $U$  denote the pipe diameter and bulk mean flow velocity, respectively. Subscripts  $a$ ,  $o$ , and  $w$  denote the phase of air, oil, and water, respectively. The range of  $D$  treatable by the present ultrasound sensing is from 20 to 100 mm while we fix  $D = 55$  mm in the present demonstration. There are hence three Reynolds numbers—two Froude numbers, and two Weber numbers—giving a total of seven dimensionless parameters. In each definition, the characteristic speed of

the flow  $U$  is given by the pipe oscillation frequency  $F$  and amplitude  $H$ ,

$$U = 2\pi FH \quad (4)$$

In the present range of test measurements,  $Re$  has order  $O(10^5)$  in water,  $O(10^4)$  in air, and  $O(10^3)$  in oil. This implies that the air–water interface is influenced by in-phase turbulence whereas the oil phase belongs to a transitional regime.  $Fr$  has order  $O(1)$  for air–water and  $O(10)$  for oil–water interfaces, evidencing the emergence of a wave-breaking front on both interfaces. The two Weber numbers are of order  $O(10)$  corresponding to a characteristic length scale of a few millimeters for capillary waves that may appear on the interfaces.

Hence, the ultrasound sensing performance is assessed for all the above-mentioned flow elements stemming from within the three-phase flow, such as turbulence in each phase, density stratification, gravity-induced waves, shear-induced capillary waves, and periodic flow sandwiched by the two neighbor interfaces.

### A. ECHO INTENSITY AND DOPPLER VELOCITY

Prior to the experiment, we estimated the transmittance and reflectance of ultrasonic waves in the three-phase pipe flow including the pipe wall. Fig. 6 shows the result of the estimation with the three phases stratified vertically. With the ultrasound transducer set at the bottom of the pipe directed upward, echoes are received from six interfaces that exist between the transducer and the counter surface of the pipe. At each interface, formed between two media with acoustic impedances  $Z_1$ , and  $Z_2$ , the reflection ratio of ultrasound is

$$R = \frac{Z_2 - Z_1}{Z_2 + Z_1}, \quad \begin{cases} Z_1 = \rho_1 C_1 \\ Z_2 = \rho_2 C_2 \end{cases} \quad (5)$$

where  $\rho$  and  $C$  are density and speed of sound, respectively. The acoustic pressure  $A.P.$  of the ultrasound wave that propagates directly beyond multiple interfaces is

$$A.P. = (1 - R_1)(1 - R_2) \cdots = \prod_{k=1}^K (1 - R_k). \quad (6)$$

Here the acoustic pressure is normalized by the value of the initial pressure of the emitted wave. In the present configuration, the values of the reflection ratios  $R$  and the acoustic pressure  $A.P.$  are obtained (Fig. 6). The acoustic pressure decreases to 0.30 in water, decreases further to 0.26 in oil, and almost disappears below  $10^{-5}$  in air. The acoustic pressure of echoes that the transducer receives is further weakened by the square impact from  $A.P.$  because of shuttled propagation. Therefore we ignore the echo signal from the air phase as its acoustic pressure is below the sensing limit  $O(10^{-5})$ . Moreover, the echo from the air–oil and the oil–water interfaces are expected to be sufficiently strong as their pressure estimates are 0.07 and 0.01, respectively.

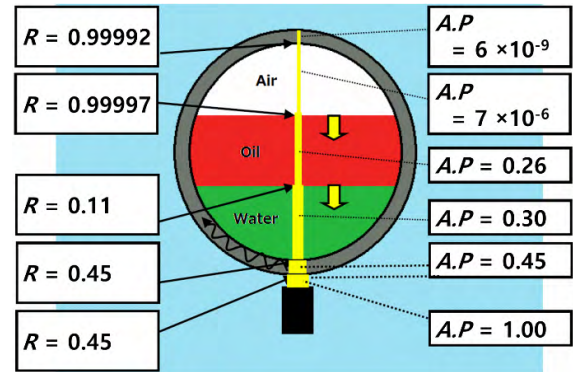


FIGURE 6. Schematic of ultrasonic transmission via six interfaces along the straight path subject to different reflection ratio  $R$  and penetration of acoustic pressure  $A.P.$

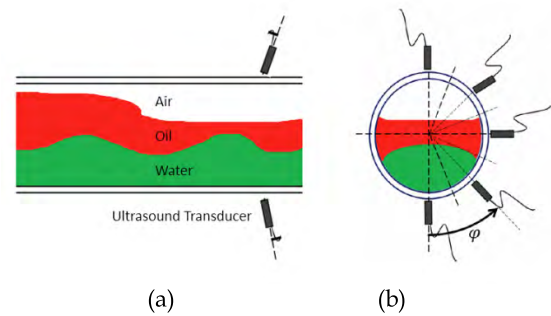
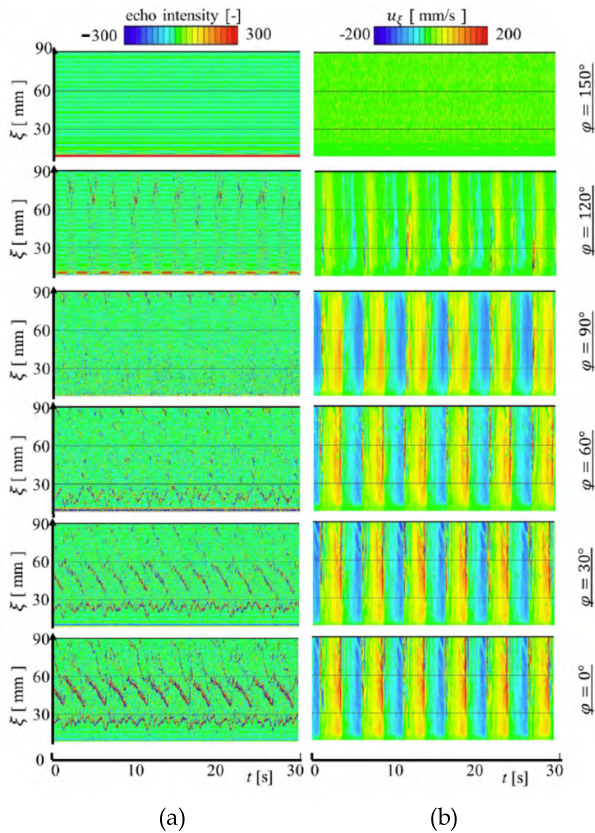


FIGURE 7. Position of ultrasound transducer for examination of orientation dependent signal characteristics. (a) Side view. (b) Cross-section view.

With the estimation, we examined the signal quality of the echo by changing the angle of inclination of the transducer (Fig. 7). The results obtained (Fig. 8) were for equal volume ratios of three phases in the pipe, which oscillated at  $F = 0.2$  Hz. The left and right columns present the echo intensity and Doppler velocity, respectively. Echo intensities were originally recorded as electric voltages with both positive and negative signs of an order of millivolts, and subsequently normalized in a linear scale by the lowest limit of sensible voltage. Doppler velocities were computed from the Doppler frequency shift involved in echo waveforms, the basic frequency of ultrasound, and the speed of sound. With the transducer inclined at  $\varphi < 60^\circ$ , the two interfaces are identifiable in the echo intensity plots. At  $\varphi = 90$ , the interfaces no longer appear because from the geometry the horizontal ultrasound pulses miss them. At  $\varphi > 120$ , the echoes disappear completely because pulses encounter the first air phase blocking transmission to the liquid phases. From the Doppler velocity profiles, the fluid motion is properly captured with repeated cycles of oil and water phases. However, Doppler velocities do not include any obvious information on interfacial position, but rather give a virtual velocity for the air phase. Next a method is described that eliminates this velocity.



**FIGURE 8.** Difference in echo intensity and Doppler velocity involved in the pulse waveforms taken in six different angles. (a) Echo intensity. (b) Doppler velocity.

**B. METHOD OF INTERFACE DETECTION**

With a significant echo intensity confirmed from both interfaces, we analyze the echo data to detect these interfaces automatically.

The procedure (see outline in Fig. 9) involves first, applying a median filter to reduce pixel noise associated with the time-space echo distribution. The size of a single pixel is defined by the temporal sampling frequency and the spatial sampling interval. Next, echo amplitudes are computed from the enveloping function, taking positive values over the entire domain. In this step, two sharp peaks appear in the spatial coordinates (middle graph of the figure) corresponding to the positions of the air–oil and oil–water interfaces. A threshold is given to detect the central coordinates of the intensity peaks. The threshold value can be determined reductively from the above-mentioned theoretical reflections. However, the reflections in actual situations are complicated through the influence of turbulence, beam divergence, and, capillary waves. Therefore, we determine the threshold from a recursive approach, selecting its value at which two positions of the strong echo are always detected. This threshold value is automatically computable from a statistical analysis of the echo data, and is relatively robust to the various flow behaviors taking place.

The three-phase identification realized by the present interface detection is shown in Fig. 10. The figure involves

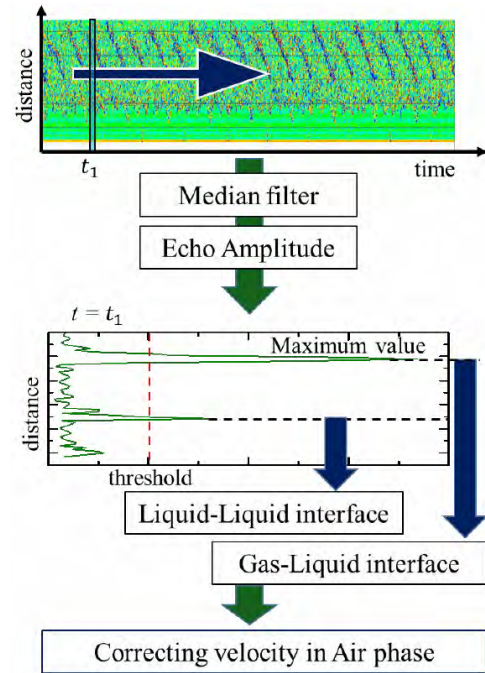


**FIGURE 9.** Flow chart of UVP-data processing with interface detection to classify the domain into gas, oil, and water phases.

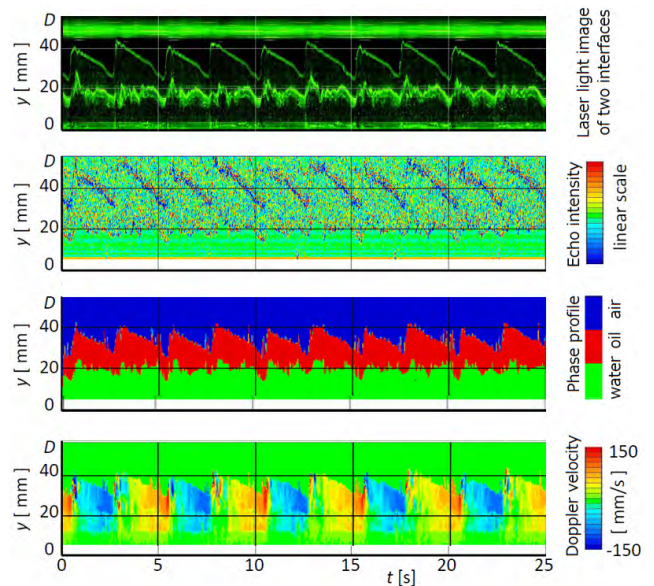


**FIGURE 10.** Samples of interface detection: (a) optical visualization, (b) echo intensity distribution, (c) phase distribution, and (d) Doppler velocity distribution.

individual time-line images of (a) the laser illumination of the two interfaces, (b) the echo intensity distribution, (c) the identification of the three-phase distribution, and (d) Doppler velocity profiles inside the oil and water phases. Regarding phase identification, some peaked errors remain at the air–oil interface in comparison with the color backlight visualization (see Fig. 4). These errors come from miss-detection of the air–oil interface due to sharp inclines in the local interface,

from where no echoes are received. Nevertheless, the three-phase flow structure is captured with acceptable accuracy for general purposes such as for measurements of volume fractions, constituent volume flow rates, and spectral analysis of interface displacements.

**C. FLOW VELOCITY PROFILING COMPARED WITH PIV**

The flow velocity distribution in the oil and water are obtained from Doppler velocities using the ultrasound velocity profiling technique (UVP). There are two main concerns when UVP is applied to two kinds of co-flowing liquids in a single measurement section. One is the pulse refraction at the oil–water interface when inclined non-perpendicularly to the propagating direction of the pulse. The other is multi-dimensional flow events excited in the three-phase flow, which UVP cannot detect because velocity profiling is one dimensional. To quantify these features, particle image velocimetry (PIV) of the flow field is employed.

From raw PIV data taken over a single cycle of the pipe oscillation, we extracted a time series of instantaneous flow velocity distributions. (Fig. 11); the magnitude of velocity vector is color coded. Here the pipe oscillation period is set at  $T = 5.0$  s (hence the frequency is  $F = 0.2$  Hz). The absence of local PIV data occurs in the result because the intensity of laser light saturates and incorrectly correlates the particle image in regions of rapid distortion in the fluid. After an adequate spatial interpolation is applied, a single vertical line along the same position of UVP is chosen to reproduce the time-line image of the velocity distribution (Fig. 12). Here the data for both UVP and PIV are the components of the flow velocity in the direction of ultrasound pulse propagation, i.e.,  $15^\circ$  to the plane perpendicular to the axial direction of the pipe. From the figure, the UVP and PIV data exhibit strong similarities. Discrepancies in the data from the air–oil interface are attributable to absences of corresponding PIV data.

A more quantitative comparison (Fig. 13) is obtained from flow velocity fluctuations at mid-height in the oil phase ( $y = 25$  mm from the bottom) and in the water phase ( $y = 15$  mm). In the velocity computation from Doppler shift frequency, values for the speed of sound in oil and water are inputted, obtained already from information gleaned from the oil–water interface. In all tests under different flow conditions, the velocity magnitude of the oil phase from UVP is always larger than that from PIV. The ratio of the root-mean-square value of UVP to PIV ranges between 1.20 and 1.25. The high value is attributed to the mean dynamic inclination of the oil–water interface induced by slugging waves. In the water phase, such a bias is less than 10%. Note though that acoustic refraction on a flat oil–water interface, which has a refraction index of  $n = 1.53$ , does not directly induce such bias error in the resultant velocity in the oil phase. The reason is simply that the pulse propagates both ways. In water-to-oil transmission, the pulse bends with refractive index  $n$ . From its own echo, it transmits a returning pulse propagating from oil to water that bends depending on the reciprocal index  $n^{-1}$  that

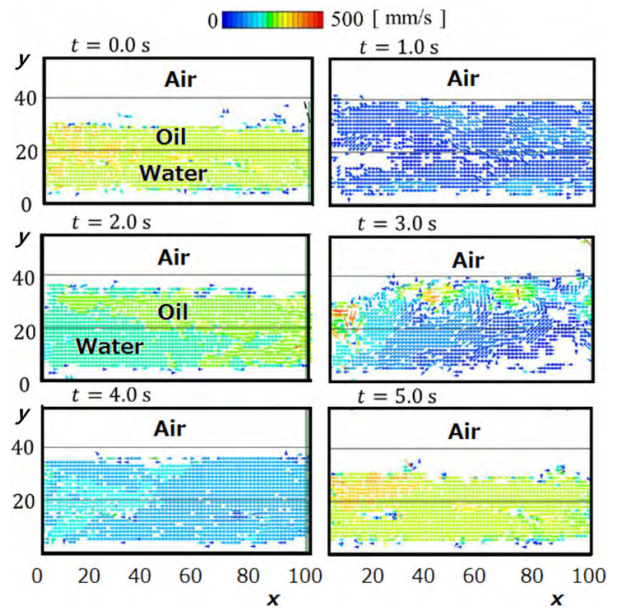


**FIGURE 11.** Instantaneous PIV data obtained inside the two liquid phases at six different timing within a single oscillation.

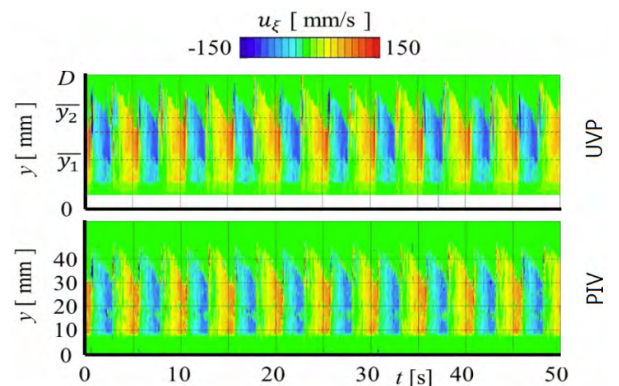


**FIGURE 12.** Comparison of fluid velocity data between UVP and PIV where PIV data are extracted on the same line of UVP.

cancels out refraction in the oil phase. The present bias of the velocity magnitude is therefore attributed to curvature effects of the interface arising from the dynamics of multiphase flow.

**D. CONSTITUENT FLOW RATES**

In addressing our final objective, constituent volume flow rates of the three-phase flow were estimated from the measured information. The present technique provides a one-dimensional three-phase flow measurement that, in principle, lacks information to correctly estimate the flow rates. An approximation model of the phase distribution is introduced for this estimation.

In testing this approach, we modeled the local phase distribution as a simple vertical stratification of the three layers (Fig. 14). In this model, a single transducer is placed at the bottom of the pipe. The flow rate of each phase is computed using the area integration of the velocity distribution within

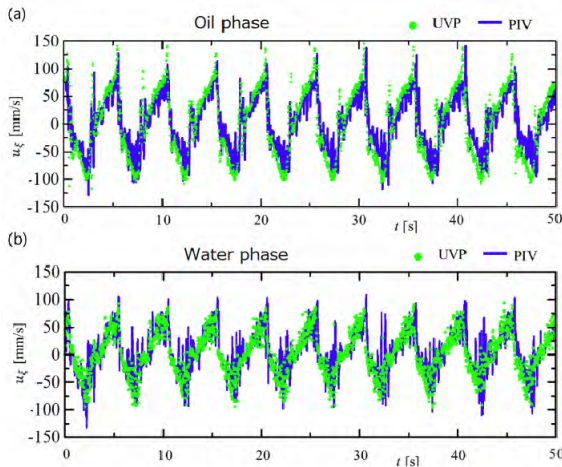


FIGURE 13. Flow velocity fluctuations in (a) the oil phase at  $y = 25$  mm and (b) the water phase at  $y = 15$  mm.

the border of the target phase,

$$Q(t) = \int_A u_x(y, z) dydz, \quad (7)$$

where  $u_x$  is the flow velocity along the axial direction of the pipe, and  $(y, z)$  are the two-dimensional coordinates in its cross-sectional plane.  $A$  is the area over which the velocity distribution is integrated, and corresponds to the area of the target phase. The present ultrasound monitoring obtains the velocity distribution  $u_x(y, z)$ , the air–oil interfacial position  $y_{ao}(z)$ , and the oil–water interfacial position  $y_{ow}(z)$  on the central line at  $0 < y < D$ ,  $z = 0$ . Conditions for perfect stratification of the three phases implies  $u_x(y, z) = u_x(y, 0)$ ,  $y_{ao}(z) = y_{ao}(0)$ , and  $y_{ow}(z) = y_{ow}(0)$ . This simplification leads to two formulae that give simultaneously the volume flow rates of both oil and water:

$$\begin{cases} Q_o(t) = \int_{y_{ow}(0)}^{y_{ao}(0)} u_x(y, 0) \cdot 2\sqrt{y(D-y)} \cdot dy, \\ Q_w(t) = \int_0^{y_{ow}(0)} u_x(y, 0) \cdot 2\sqrt{y(D-y)} \cdot dy. \end{cases} \quad (8)$$

These quantities are computed using discrete numerical integration based on the rectangular rule, and depend on the spatial sampling interval. Note that these two independent flow rates are obtained as a function of time at a given arbitrary sampling frequency of the ultrasound measurement.

Fig. 15 shows the plots of the time-dependent flow rates for oil and water in the half-period of the pipe oscillation at sampling rate of 67 Hz. The oil phase moves earlier than the water phase and its flow rate peaks first. This is due to gravity waves in the oil phase propagating above the water phase. The water phase then flows and accelerates whereas the oil flow settles. When the water flow rate peaks, the oil flow moves again which persists after the water flow stops. Large scattering of the data in the oil flow rate near the tail of the distribution is attributed to a vertical fluctuation of the oil–water interface owing to shear-induced waves amplified. The total flow rate of oil and water phases (marked in black) increases

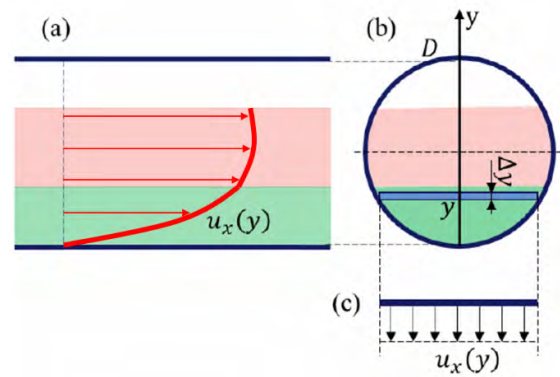


FIGURE 14. Velocity profile integration: (a) side view, (b) cross-section view, and (c) definition of  $u_x(y)$ .

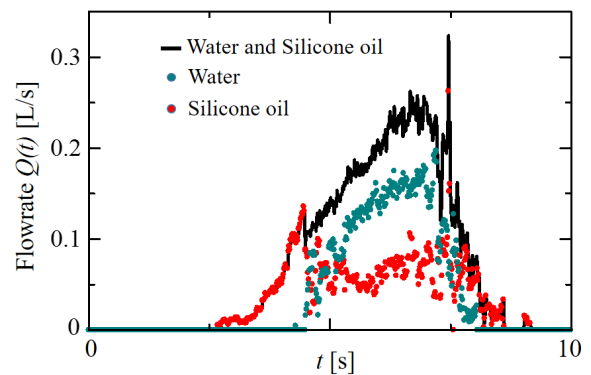


FIGURE 15. Instantaneous volume flow rates measured by cross-sectional integration of axial velocity profile for each phase.

monotonically, peaks, and gradually decreases, being simpler than the behavior of the constituent flow rates. This implies that the total flow rate behaves as a two-phase flow of gas and liquid [25]–[27]; its decomposition into three phases shows no functional similarity to the total liquid flow rate. A large peak in the total flow rate in the tail comes from a three-phase flow instability, which takes place at the moment when the flow rate of water decelerates quickly and falls below that of oil. Note that, in the present experimentation platform, the volume flow rate of air is given simply by  $Q_a = -(Q_o + Q_w)$  as the three phases are packed inside a single pipe with closed ends. In a long pipe without ends, the flow rate of the gas phase can be estimated using the equation of continuity for incompressible multiphase flow.

A quantitative assessment of the accuracy in flow rate measurements is possible as a cumulative flow volume is evaluated from the time-dependent constituent flow rates. The results for the cumulative flow volume for each phase (Fig. 16) were calculated using

$$V(t) = \int_{t=0}^t Q(t) dt. \quad (9)$$

In tests, we poured 400 mL of water and 300 mL of Silicone oil into the pipe. For the measurement system to demonstrate perfect accuracy, the cumulative flow volumes need

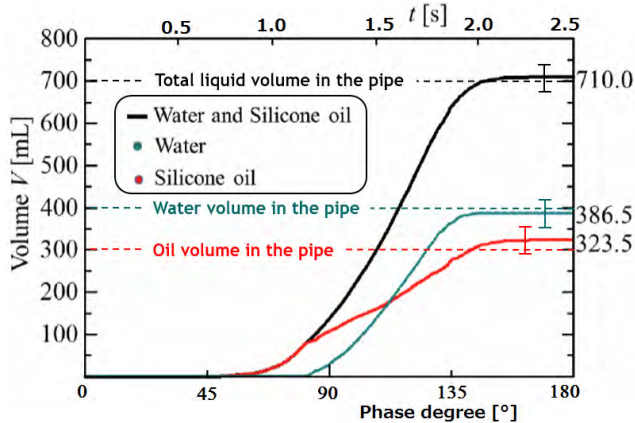


**FIGURE 16.** Measured cumulative flow volumes given by space-time integral of UVP-velocity data as 300 mL and 400 mL of oil and water were filled inside the pipe. Error bars indicate 10 % in relative error.

to recover these same values. The measured results in the figure indicate that the error is 3% for water and 8% for oil. The error for the total liquid flow rate is 2%. By the same assessment for the other three-phase flow conditions, the maximum error has been found to be less than 10% for constituent flow rates and 5% for total flow rates. These evaluations are notable in the single slugging motion of the three-phase flow, and in principle, therefore, the flow rate over long-duration time averages, including unsteady flow, would yield better accuracy using the sampling law, i.e. the inverse square-root principle. For instance, 10% of the random error for a single event is comparable with 5% for four events, and 1% for 100 events. In applications, we assume users will choose time-average durations depending on their needs when applying the present measurement technique.

#### IV. SUMMARY

An experimental technique for ultrasound monitoring of three-phase pipe flow was presented. We designed a saw-tooth type of pipe oscillation facility and an experimentation platform to control the internal three-phase behavior with arbitrary unsteadiness. For an in-depth analysis, multiple measurement instrumentations were mounted on the same frame. Our main focus on three-phase flow was periodic co-flowing stratified flow that accompanied multiple flow elements to evaluate the performance of ultrasound sensing. The flow features slugging wave fronts on the air–oil interface, shear-induced displacements on the oil–water interface, and turbulence in the tail of the stratified flow.

The following conclusions are drawn: (i) Ultrasound echoes are detectable from both the air–oil interface and the oil–water interface as long as the transmission occurs in the first of either liquid in the pipe; (ii) The flow velocity obtained from pulse Doppler signals is influenced by acoustic refraction at the oil–water interface leaving a bias error dependence in the flow behavior; (iii) The identification of the fluid phase is realized by thresholding the echo intensity

profile. With the identification, the virtual Doppler velocity distribution inherent in the air phase can be eliminated; and (iv) Constituent flow rates are obtained by spatial integration of velocity distribution within each identified phase. The volume error is less than 10% for a single slugging event, which is equivalent to 1% in calculations of a 100-ensemble-averaged flow rate. The next step of development is to use multiple ultrasound measurement lines, which may improve the three-dimensional monitoring of three-phase flows.

#### Acknowledgments

The authors express their thanks to the technical supporting staff, Mr. Toshiyuki Sampo, Mr. Taiki Yoshida, Ms. Megumi Akashi (Hokkaido University) and collaborative partner, Dr. Shinsuke Sato (Mitsubishi Heavy Industries, Ltd).

#### REFERENCES

- [1] Y. Inoue, H. Kikura, H. Murakawa, M. Aritomi, and M. Mori, "A study of ultrasonic propagation for ultrasonic flow rate measurement," *Flow Meas. Instrum.*, vol. 19, nos. 3–4, pp. 223–232, Jun./Aug. 2008.
- [2] Y. Takeda, "Velocity profile measurement by ultrasound Doppler shift method," *Int. J. Heat Fluid Flow*, vol. 7, no. 4, pp. 313–318, 1986.
- [3] B. Beulen, A. C. Verkaik, N. Bijnens, M. Rutten, and F. van de Vosse, "Perpendicular ultrasound velocity measurement by 2D cross correlation of RF data—Part B: Volume flow estimation in curved vessels," *Experim. Fluids*, vol. 49, no. 6, pp. 1219–1229, 2010.
- [4] M. J. W. Povey, *Ultrasonic Techniques for Fluids Characterization*. London, U.K.: Academic, 1997, pp. 11–44.
- [5] B. Ourlev and E. Windhab, "Novel ultrasound based time averaged flow mapping method for die entry visualization in flow of highly concentrated shear-thinning and shear-thickening suspensions," *Meas. Sci. Technol.*, vol. 14, no. 1, pp. 140–147, 2003.
- [6] T. Nakashima, T. Shiratori, Y. Murai, Y. Tasaka, Y. Takeda, and E. J. Windhab, "Viscoelastic responses of flow driven by a permeable disk investigated by ultrasound velocity profiling," *Flow Meas. Instrum.*, vol. 48, pp. 97–103, Apr. 2016.
- [7] T. Wang, J. Wang, F. Ren, and Y. Jin, "Application of Doppler ultrasound velocimetry in multiphase flow," *Chem. Eng. J.*, vol. 92, nos. 1–3, pp. 111–122, 2003.
- [8] H. Murakawa, H. Kikura, and M. Aritomi, "Application of ultrasonic Doppler method for bubbly flow measurement using two ultrasonic frequencies," *Experim. Thermal Fluid Sci.*, vol. 29, no. 7, pp. 843–850, 2005.
- [9] Y. Murai, H. Fujii, Y. Tasaka, and Y. Takeda, "Turbulent bubbly channel flow investigated by ultrasound velocity profiler," *J. Fluid Sci. Technol.*, vol. 1, no. 1, pp. 12–23, 2006.
- [10] M. R. Widyanto, M. B. Utomo, K. Kawamoto, B. Kusumoputro, and K. Hirota, "Local gas holdup measurement of a bubble column using SONIA-ultrasonic non-invasive method," *Sens. Actuators A, Phys.*, vol. 126, no. 2, pp. 447–454, 2006.
- [11] Y. Murai, S. Ohta, A. Shigetomi, Y. Tasaka, and Y. Takeda, "Development of an ultrasonic void fraction profiler," *Meas. Sci. Technol.*, vol. 20, no. 11, p. 114003, 2009.
- [12] S. R. G. A., Y. Murai, and Y. Takeda, "Chapter 1 ultrasound-based gas–liquid interface detection in gas–liquid two-phase flows," *Adv. Chem. Eng.*, vol. 37, pp. 1–27, Dec. 2009.
- [13] S. M. van der Meer et al., "Microbubble spectroscopy of ultrasound contrast agents," *J. Acoust. Soc. Amer.*, vol. 212, no. 1, pp. 648–656, 2007.
- [14] H. Murakawa, H. Kikura, and M. Aritomi, "Application of ultrasonic multi-wave method for two-phase bubbly and slug flows," *Flow Meas. Instrum.*, vol. 19, nos. 3–4, pp. 205–213, 2008.
- [15] Y. Murai, Y. Tasaka, Y. Nambu, and Y. Takeda, S. R. G. A., "Ultrasonic detection of moving interfaces in gas–liquid two-phase flow," *Flow Meas. Instrum.*, vol. 21, no. 3, pp. 356–366, 2010.
- [16] Y. Takeda, Y. Murai, and Y. Tasaka, "Ultrasonic multiphase flowmeter, ultrasonic multiphase flow rate measurement program, and multiphase flow rate measurement method using ultrasonic wave," U.S. Patent 8401805 B2, Mar. 13, 2013.

[17] Y. Tasaka, T. Kimura, and Y. Murai, “Estimating the effective viscosity of bubble suspensions in oscillatory shear flows by means of ultrasonic spinning rheometry,” *Experim. Fluids*, vol. 56, p. 1867, Jan. 2015.

[18] H. J. Park, Y. Tasaka, and Y. Murai, “Ultrasonic pulse echography for bubbles traveling in the proximity of a wall,” *Meas. Sci. Technol.*, vol. 26, no. 12, p. 125301, 2015.

[19] M. M. F. Figueiredo, J. L. Goncalves, A. M. V. Nakashima, A. M. F. Fileti, and R. D. M. Carvalho, “The use of an ultrasonic technique and neural networks for identification of the flow pattern and measurement of the gas volume fraction in multiphase flows,” *Experim. Thermal Fluid Sci.*, vol. 70, pp. 29–50, 2016.

[20] G. Oddie and J. R. A. Pearson, “Flow-rate measurement in two-phase flow,” *Annu. Rev. Fluid Mech.*, vol. 36, pp. 149–172, Jan. 2004.

[21] A. J. Mwambela and G. A. Johansen, “Multiphase flow component volume fraction measurement: Experimental evaluation of entropic thresholding methods using an electrical capacitance tomography system,” *Meas. Sci. Technol.*, vol. 12, no. 8, pp. 1092–1101, 2001.

[22] W. Warsito and L.-S. Fan, “Measurement of real-time flow structures in gas–liquid and gas–liquid–solid flow systems using electrical capacitance tomography (ECT),” *Chem. Eng. Sci.*, vol. 56, nos. 21–22, pp. 6455–6462, 2001.

[23] Y. Murai, Y. Matsumoto, and F. Yamamoto, “Three-dimensional measurement of void fraction in a bubble plume using statistic stereoscopic image processing,” *Exp. Fluids*, vol. 30, no. 1, pp. 11–21, 2001.

[24] E. Hervieu, E. Jouet, and L. Desbat, “Development and validation of an X-ray tomography for two-phase flow,” *Ann. New York Acad. Sci.*, vol. 972, no. 1, pp. 87–94, 2002.

[25] Y. Murai, H. Oiwa, T. Sasaki, K. Kondou, S. Yoshikawa, and F. Yamamoto, “Backlight imaging tomography for gas–liquid two-phase flow in a helically coiled tube,” *Meas. Sci. Tech.*, vol. 16, no. 7, pp. 1459–1468, 2005.

[26] Y. Murai, S. Yoshikawa, S. Toda, M. Ishikawa, and F. Yamamoto, “Structure of air–water two-phase flow in helically coiled tubes,” *Nucl. Eng. Des.*, vol. 236, no. 1, pp. 94–106, 2006.

[27] Y. Murai, K. Inaba, Y. Takeda, and F. Yamamoto, “Backlight imaging tomography for slug flows in straight and helical tubes,” *Flow Meas. Instrum.*, vol. 18, nos. 5–6, pp. 223–229, 2007.



**YUICHI MURAI** received the Ph.D. degree in engineering from the University of Tokyo in 1996. He was involved in nuclear engineering with Fukui University and applied optics with the Imperial College London from 1995 to 2012. He has been a Full Professor with Hokkaido University since 2010. His research interests are dynamics of multiphase flows, measurement techniques of fluid flows, and renewable energy.



**HYUN JIN PARK** received the Ph.D. degree from Hokkaido University in 2016. He was with LG Electronics Inc. and the Institut de Mécanique des Fluides de Toulouse. He has been an Assistant Professor with Hokkaido University since 2016. His research interests are ship drag reduction, multiphase flow, ultrasound technology, PIV, image processing, laser applications, and signal processing for various thermo-fluid physics and engineering systems.



**JUNPEI HITOMI** received the degree from the Department of Mechanical Intelligence System Engineering, Hokkaido University, in 2017. He received the Hatakeyama Prize given for best students in the field of mechanical engineering and from the Japan Society of Mechanical Engineers in 2017. His main research is the development of ultrasound techniques for dynamic multiphase flow systems.



**YUJI TASAKA** received the Ph.D. degree from Hokkaido University in 2004. He started his professional research career with Hokkaido University, as a Research Associate, and where he has been an Associate Professor since 2011. His research interests are flow instability and transition phenomena, as well as the development of measurement techniques.

...

# Flow Monitoring of Particle-laden Flows Combining Ultrasonic Doppler and Echo Intensity Profiling Techniques

Jumpei Hitomi<sup>1,2</sup>, Shun Nomura<sup>2,3</sup>, Giovanni De Cesare<sup>2</sup>, Yasushi Takeda<sup>4</sup>, Hyun Jin Park<sup>1</sup>, Yuji Tasaka<sup>1</sup>, and Yuichi Murai<sup>1</sup>

<sup>1</sup>Laboratory for Flow Control, Hokkaido University, N13-W8, Kita-ku, Sapporo, Hokkaido 060-8628, Japan

<sup>2</sup>Ecole polytechnique fédérale de Lausanne EPFL, Plateforme de constructions hydrauliques PL-LCH, Station 18, CH-1015 Lausanne, Switzerland

<sup>3</sup>Mathematical Science and Advanced Technology, JAMSTEC, Yokohama Institute of Earth Sciences, 3173-25 Showa-machi, Kanazawa-ku, Yokohama 236-001, Japan

<sup>4</sup>Laboratory for Food Research Engineering, Swiss Federal Institute of Technology Zurich, Zurich 8092, Switzerland

The methodology to reveal inner structures of turbidity currents are required. Their behaviors have important roles to affect the sedimentation or transportation of fine particles. We have proposed a novel monitoring methodology for flows containing fine particles, combining Doppler velocity and echo information obtained from ultrasonic velocity profiler (UVP). In this study, we captured the relationship between the echo profiles and particle number distributions. To simplify turbidity currents, stirring flows in a cylindrical container were chosen. As suspended particles, quartz particles with 13.5  $\mu\text{m}$  in the central diameter was examined. In a certain range of quartz volume fraction  $\alpha$ , UVP can detect integral echo signals obeying Rayleigh scattering and Doppler-shift frequencies, although the quartz diameter is much smaller than ordinary tracer particles adopted for UVP. The echo distribution of  $\alpha = 1\%$  showed that the stirring flow causes the local particle number distributions. Moreover, the possibility to reconstruct particle number distributions from echo amplitude distributions was indicated.

**Keywords:** Echo intensity, Particle-laden fluid, Particle number density distribution, Solid-liquid two-phase flow, Rotational flow

## 1. Introduction

In the hydraulic industry, liquid-solid two-phase flows which contain solid particles have important roles to utilize aquatic resources. For example, collecting minerals and fossil fuels under the sea and transportation or sedimentation mechanisms of solid particles in reservoirs have been paid attention to. An example of them and main topic of our research group is turbidity currents [1-3] which are gravity currents driven by the density difference between particle-laden fluid and ambient fluid. They have complicated flow structures due to turbulence and complex interaction caused between each particle. They show local mixture density fluctuation accompanying clusters and clouds of particles, which is hardly investigated by optical approaches and numerical simulations. Our research group, therefore, has proposed the direct monitoring methodology of such particle-laden flows using ultrasonic technique. Ultrasonic velocity profiler (UVP) [4] can be applied to opaque fluids and measure the spatio-temporal velocity distributions using frequency veering based on Doppler effects. In addition, echo signals which are reflected waves scattered by suspended particles give us beneficial information on particle number distributions. In past studies, scattering processes from clouds of fine particles are researched [5, 6]. Even echo signals obtained from UVP could be used to detect moving interfaces of multi-phase or multi-layer flows [7, 8]. In addition, they were applied to obtain the profiles of suspended sediment concentration [9] and to measure void fractions [10]. Combining two distributions of Doppler velocity and

echo information, a novel monitoring methodology for turbidity currents expects to be established.

The objective of this study is to reveal relationship between number density distribution of fine particles and echo information. Stirring flows in a cylindrical container were chosen to simplify particle-laden flows like turbidity currents. As suspension particles, quartz particles with order of 10  $\mu\text{m}$  in the central diameter are examined. This range of particle diameter is less than one-tenth the ultrasonic wavelength of central frequency 4 MHz in water, so Rayleigh scattering, which is almost isotropic scattering, occurs. They are not used for UVP measurement basically, because the intensity of reflected waves from a quartz particle is too small to be detected by ultrasonic transducers. It was, therefore, another objective to elucidate the flow conditions and the volume fractions of the quartz particles that UVP can measure reasonable velocity distributions of particle-laden flows.

## 2. Experiments

### 2.1 Experimental setup

The experimental setup is shown in figure 1. The experiments were conducted in a cylindrical container with 100 mm outer diameter, and 3 mm thickness of lateral wall and 120 mm height. The cylinder is made of acrylic resin and filled with test fluids containing the fine particles. The cylinder does not have a lid and thus top of fluid layer is free surface. The cylinder was mounted inside the water jacket to keep uniform temperature and allow transmission of ultrasonic wave from the outside of

the cylinder. The flow was driven by a stirrer with 60 rpms in the rotational speed, and a stirring bar dipped into the bottom of the cylinder.

Velocity distribution and echo information were measured by UVP. The obtained ultrasonic signals reflected from clouds of particles were processed by UVP monitor model Duo (Met-Flow S.A.) into spatio-temporal distributions of Doppler velocity and echo information. An ultrasonic transducer with 4 MHz central frequency was fixed in the jacket with a horizontal displacement 10 mm from the center line. This off-axis measurement makes it possible to obtain the velocity component including not only radial but also azimuthal velocity component. In case of rigid body rotation, the obtained velocity components show uniform profile along the measurement line. The advantage of this method, therefore, is that flow structures can be imagined from obtained velocity distributions relatively easily and reconstructed assuming axisymmetric flow field. The transducer was set at 25 mm from the bottom of the cylinder to avoid the blind of ultrasonic propagation due to the free surface. Table 1 summarizes the setting parameters of UVP measurement. Especially, amplification is important parameter in this study. Both values of “gain start” and “gain end” were fixed at constant values not to amplify the echo value depending on the distance from the transducer.

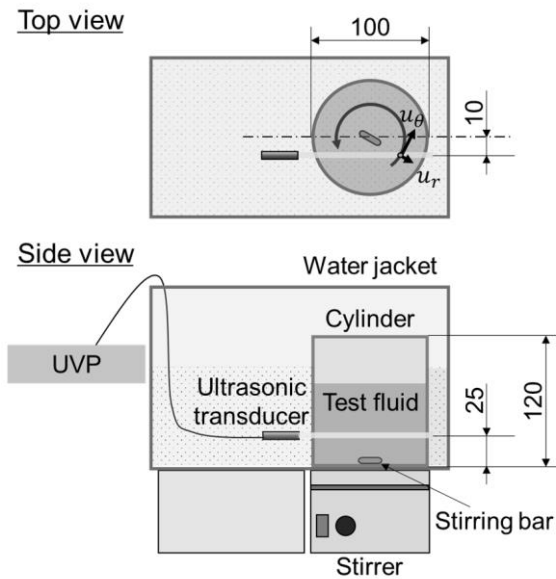


Figure 1: Schematic diagram of experimental setup and arrangement of the measurement line.

## 2.2 Test fluid

In this study, quartz (Quartz K13, Carlo Bernasconi AG) which is often used as laden particles of experimental turbidity currents was examined. Quartz has particle size distribution and the central diameter is  $13.5 \mu\text{m}$ , and density equals to  $2650 \text{ kg/m}^3$ . It is predicted that Rayleigh scattering, which is almost isotropic scattering, occurs in the test fluids, because quartz diameter is less than about one-tenth the ultrasonic wavelength of central frequency

4 MHz in water. The cylinder was filled with 500 mL of tap water and quartz was added based on each volume fraction  $\alpha$ . Total seven cases with different volume fractions  $\alpha = 0, 0.01, 0.1, 1, 5, 10, \text{ and } 15\%$  were conducted.

Table 1: Setting parameters of UVP.

Central frequency	4	MHz
Temporal resolution	10	ms
Spatial resolution	0.74	mm
Velocity resolution	4.75	mm/s
Number of cycles	4	-
Number of repetitions	32	-
Amplification (gain)	6-6	-

## 3. Results and discussions

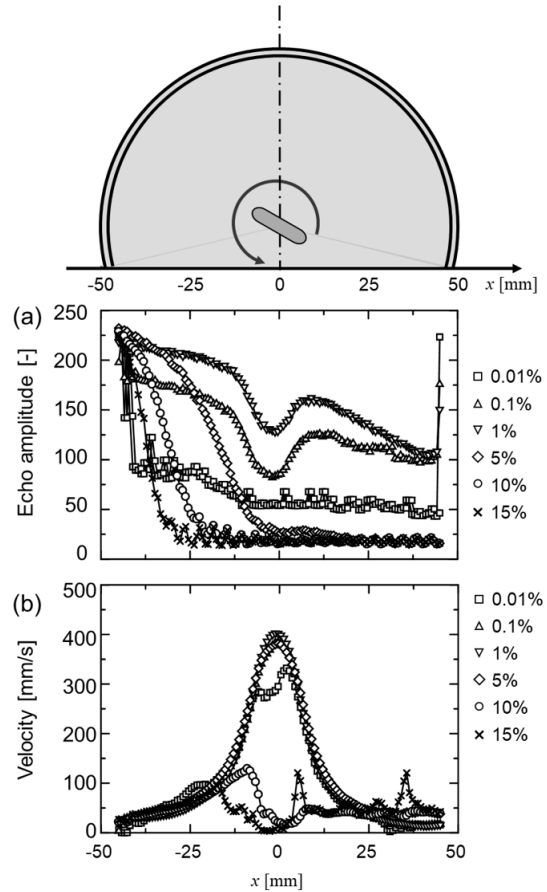


Figure 2: Distributions of time-averaged value of each volume fraction; (a) echo amplitude and (b) Doppler velocity distribution.

Firstly, we tried to comprehend the trends of echo distribution measured in this setup. Figure 2 (a) shows the echo amplitude profiles obtained by UVP in each case. The measurements were conducted for 40 s after the flows reached adequate developed states, and the corresponding number of the velocity profiles for time-averaging is 4000. These echo amplitudes were calculated as the absolute values of difference from

background ( $\alpha = 0\%$ ) UVP echo values. In this figure,  $x$  axis indicates the distance from the center of the cylinder and the ultrasonic measurement direction is from left to right side. As the volume fraction becomes larger in the cases of  $\alpha = 0.01, 0.1, \text{ and } 1\%$ , echo amplitude values are getting larger. Their echo amplitudes of these cases show large values on the opposite side from the ultrasonic transducer because of the reflection from the wall. In contrast, the reflected waves from the wall disappears under the conditions  $\alpha \geq 5\%$  due to the attenuation of ultrasonic waves and the attenuation is getting larger depending on their volume fractions. Figure 2 (b) shows velocity distributions measured by UVP. These velocities show the components of the measurement direction that contain the azimuthal and radial velocity components. In the cases of  $0.1 \leq \alpha \leq 5\%$ , reasonable velocity distributions can be observed. In this study, the velocity profiles measured with usual tracer particles (DIAION HP20SS, Mitsubishi Chemical, diameter  $60 - 150 \mu\text{m}$ , density  $1020 \text{ kg/m}^3$ ) is defined as correct distribution, and “reasonable velocity distribution” means having good agreement with the correct distribution. The velocity profiles of  $0.1 \leq \alpha \leq 5\%$  have an accuracy that has a high cross-correlation value exceeding 0.95 for the correct distribution. The cases of  $\alpha = 10$  and  $15\%$ , however, do not show the reasonable velocity distributions. It seems that the attenuation of ultrasonic waves prevents the detection of echo signals by the ultrasonic transducer. In addition, the case of  $\alpha = 0.01$  shows a notable result. The velocity values of this case drop irregularly near the center of the cylinder. This phenomenon implies that the amount of quartz particles is much fewer than wall side due to the centrifugal force. As known from the velocity distribution, high velocity values can be observed near the center. As the distance from the center becomes longer, the velocity values are getting smaller. From these distributions, the existence of a free vortex is indicated. The density of quartz is about 2.65 times larger than that of water, so it is possible that particles are blown from the center to near the wall sides by the centrifugal force. These phenomena are indicated by echo distributions too, because their values also drop near the center under the cases of  $\alpha = 0.1$  and  $1\%$ .

Basically, UVP measurements are applied to flows containing tracer particles with adequate size, density, and concentration to reflect ultrasonic waves. However, the concentrations of particles in these experiments are relatively larger in comparison with the flows of normal UVP measurements. The experimental results for  $0.1 \leq \alpha \leq 5\%$  show reasonable velocity distributions. This range of particle concentration, therefore, might be useful to detect integral echo signals obeying Rayleigh scattering. That is why UVP can obtain velocity distribution, although quartz diameter is much smaller than tracer particles.

To reveal the particle number distributions, a supplemental experiment was conducted. The mean volume fraction  $\alpha$  was fixed at  $1\%$ , because the echo amplitude dramatically dropped near the center

comparing to other conditions and reasonable velocity distributions could be obtained. In this experiment, the stirrer worked in the same manner as previous experiments until 20 s. After 20 s later from start of the measurement, the stirrer was turned off. The results of echo amplitude and velocity distributions are shown in figure 3. The velocity distribution shows that the free vortex near the center disappeared immediately after turning the stirrer off. The echo amplitude distribution, moreover, dramatically changes. During the time from 20 to 40 s, homogeneous dispersion of the quartz particles can be assumed, because it had been completely mixed for the first 20 s. During the first 20 s, the low echo region exists near the center. In contrast, that band near the center disappears after 20 s later, and the echo values measured in the far region from the ultrasonic transducer becomes smaller than that of the first 20 s. As the result of this experiment, it is revealed that not only velocity but also echo distribution were changed dramatically depending on the motion of stirrer. It seems that the change of flow velocity induces the local particle number distribution.

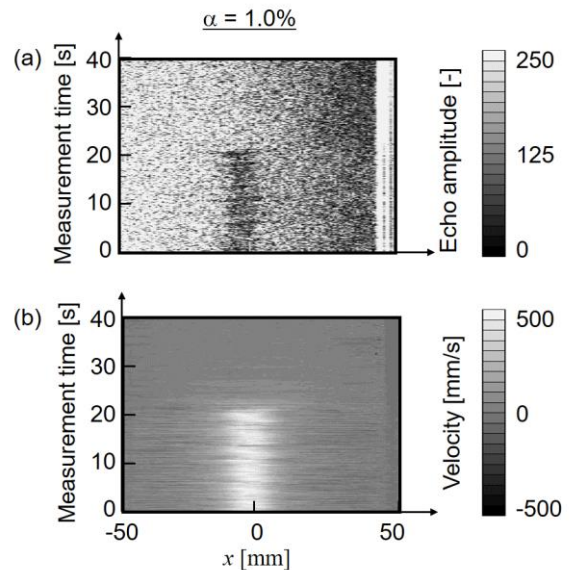


Figure 3: Spatio-temporal distribution of (a) Echo amplitude and (b) Doppler velocity when stirrer was turned off at 20 s later.

To evaluate the relationship between echo amplitude and particle number distribution, time-averaged values of echo amplitude of two cases were calculated. The first is averaged values of the first 15 s and the second is that of the last 15 s. These results are shown in figure 4. The figure 4 shows the characteristic distribution of echo values. The echo values measured in the first 20 s are larger than that of the last 20 s near the both walls, roughly  $|x| > 15$ . In contrast, the echo values measured in the first 20 s drop sharply near the center. This trend of the echo distribution seems to be related to the particle number distribution. That is to say, the stirring flow causes the free vortex and it blows particles from the center to near the wall sides due to the centrifugal force.

The echo amplitude ratio at two conditions are shown in figure 5 (a). In this graph, the range of  $x$  axis shows from 0 to 45 mm which is far side from the ultrasonic transducer. To capture the characteristics of the flow field, Shiratori *et al.* [11] had established the methodology to obtain two velocity components of azimuthal and radial direction assuming axisymmetric flow field. The two velocity components obtained by this methodology are shown in figure 5 (b). In these profiles, the azimuthal velocity is dominant in the cylinder. Range of the lower echo amplitude ratio shown in figure 5 (a), roughly  $0 \leq x \leq 15$  mm, corresponds to relatively higher azimuthal velocity range.

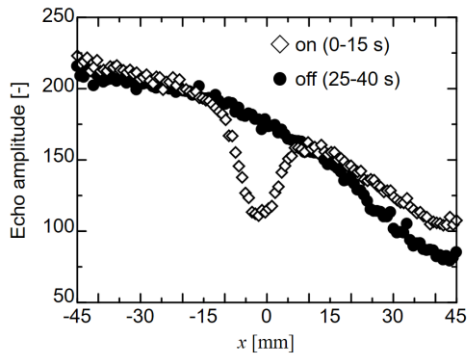


Figure 4: Time-averaged echo amplitude of each case

It would be possible to reconstruct the particle number distributions from echo amplitude ratio. Echo intensity values are the resultant values after some interactions between ultrasonic waves and media including the particles and water, such as attenuation, scattering, and so on. Theoretical models and equations are required to establish the methodology and its applicable range, which can reconstruct particle number distributions.

#### 4. Conclusions

This study revealed the relationship between echo information and number density distribution of fine particles which are much smaller than the wavelength of emitted ultrasonic wave. UVP was applied to particulate rotating flows driven by a stirrer in a cylindrical container. As suspension particles, quartz particles with order of 10  $\mu\text{m}$  in the diameter are examined. Although this range of particle diameter is smaller than ordinary tracer particles adopted for UVP, reasonable velocity distributions could be obtained under the condition where the volume fraction of particles  $\alpha$  is from 0.1 to 5% due to the detection of the integral echo signals which obeys Rayleigh scattering. Paying attention to the echo distribution observed at  $\alpha = 1\%$ , the trend of particle number distribution in the cylinder was newly explored. As the result of the experiment, it was confirmed that the range of lower echo amplitude ratio corresponded to the range such that azimuthal velocity is relatively large. It is therefore inferred that the free vortex containing the dominant azimuthal velocity components relates to the local particle number density, which can be predicted from echo amplitude distribution. As the future work, the

theoretical models and equations describing the model are required to establish comprehensive methodology to reconstruct particle number distributions from echo values.

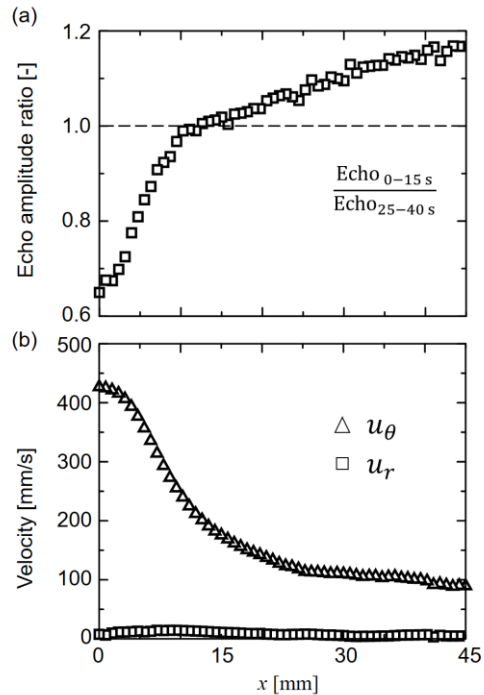


Figure 5: (a) Profiles of echo amplitude ratio at two conditions and (b) profiles of the azimuthal and radial velocity component.

#### References

- [1] Altinaker MS *et al.*: Flow structure in turbidity currents, *J. Hydraul. Res.*, 34 (1996), 713-718.
- [2] Simpson, JE: Gravity currents in the environment and the laboratory, Cambridge University Press, London, (1997).
- [3] De Cesare G *et al.*: Experiments on turbidity currents influenced by solid and permeable obstacles and water jet screens, *ISUD6*, (2008).
- [4] Takeda Y: Ultrasonic Doppler velocity profiler for fluid flow, Springer, (2012).
- [5] Thorne PD & Hanes DM: A review of acoustic measurement of small-scale sediment processes, *Cont. Shelf. Res.*, 22 (2002), 603-632.
- [6] Lee TH & Hanes DM: Direct inversion method to measure the concentration profile of suspended particles using backscattered sound, *J. Geophys. Res.*, 100 (C2) (1995), 2649-2657.
- [7] Murai Y *et al.*: Ultrasonic detection of moving interfaces in gas-liquid two-phase flow, *Flow Meas. Instrum.*, 21 (2010), 356-366.
- [8] Hitomi J *et al.*: Ultrasound flow-monitoring and flow-metering of air-oil-water three-layer pipe flows, *IEEE access*, 5 (2017), 15021-15029.
- [9] Pedocchi F & García MH: Acoustic measurement of suspended sediment concentration profiles in an oscillatory boundary layer, *Cont. Shelf. Res.*, 46 (2012), 87-95.
- [10] Murai Y *et al.*: Development of an ultrasonic void fraction profiler, *Meas. Sci. Technol.*, 20(11), (2009), 114003.
- [11] Shiratori *et al.*: Development of ultrasonic visualizer for capturing the characteristics of viscoelastic fluids, *J. Vis.*, 16 (2013), 275-286.

## Comparison of flow behaviors between experimental turbidity currents and saline density currents combining ultrasonic and optical techniques

Jumpei Hitomi\*, Shun Nomura \*\*, Giovanni De Cesare\*\*\*, Yasushi Takeda\*\*\*\*\*,  
Hyun Jin Park\*, Yuji Tasaka\*, Yuichi Murai\*

\*Laboratory for Flow Control, Faculty of Engineering, Hokkaido University

\*\* Mathematical Science and Advanced Technology, JAMSTEC

\*\*\* Laboratoire de Constructions Hydrauliques, École Polytechnique Fédérale de Lausanne (EPFL)

\*\*\*\* Food Process Engineering Laboratory, Swiss Federal Institute of Technology Zürich (ETH)

hitomi@ring-me.eng.hokudai.ac.jp

Turbidity currents [1], which are driven by density difference between particle-suspended fluid and ambient fluid, have important roles relating to the transportation and sedimentation of fine particles under seas and rivers. They are reported to travel much longer than distance expected from theories and numerical simulations despite containing numerous particles with heavier density than water, the distance is likely to reach a few thousand kilometers. Such a long-range propagation mechanism is not revealed completely yet due to the complicated flow structures and some interactions of particle-particle or particle-fluid. Our research group focuses on the experimental study of the turbidity currents. In this report, we highlight characteristics of turbidity currents by comparing with saline density currents. Those currents were generated by the lock-exchange method using a rectangular container with 4548 mm in overall length, 210 mm in height, and 143 mm in width. The initial densities of the test fluids in all cases were fixed at  $1008 \text{ kg/m}^3$ . Total 11 currents were examined, and 8 of them were turbidity currents and the others were density currents. Their macroscopic motions were evaluated from instantaneous images taken by a video camera, and inner velocity distributions were measured by ultrasonic velocity profiler (UVP) [2] that can be applied to opaque fluids such a particle-suspended fluid. As shown in Fig.2, a significant difference relating to the front velocity could be found depending on the presence or absence of fine particles. In the presentation, quantitative elucidation of long-range propagation mechanism of turbidity current will be explained from spatiotemporal velocity distributions obtained by UVP.

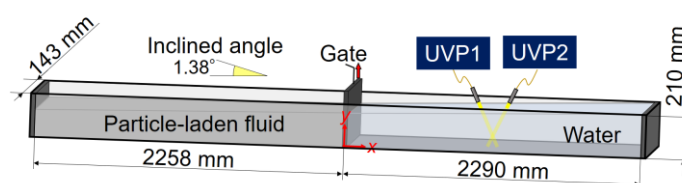


Fig.1 Experimental setup

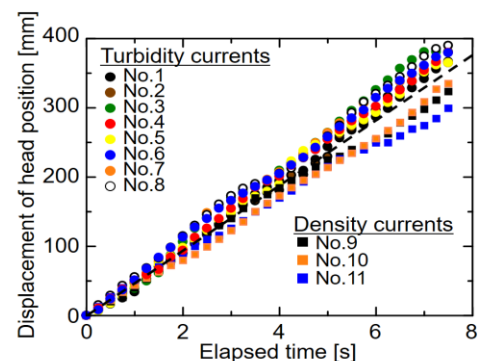


Fig.2 Displacement of head position measured from each experimental image

### References

1. B. Kneller, C. Buckee, The structure and fluid mechanics of turbidity currents: a review of some recent studies and their geological implications. *Sedimentology*, Vol.47, pp. 62-94 (2000)
2. Y. Takeda, *Ultrasonic Doppler velocity profiler for fluid flow*, Springer, (2012).

# UVP を用いた管内水・油・空気層状流の流量計測

人見 純平<sup>○</sup>(北大), 朴 炫珍(北大), 田坂 裕司(北大), 村井 祐一(北大)

## UVP flow-metering of air–oil–water three-layer pipe flows Jumpei HITOMI, HyunJin PARK, Yuji TASAKA and Yuichi MURAI

### ABSTRACT

We have proposed a novel multi-phase flowmeter using ultrasonic velocity profiler (UVP) for quantitative measurement of opaque complex flows in fuel pipeline systems arranged at bottom of the sea. Echo intensity obtained from UVP makes it possible to detect not only gas–liquid but also liquid–liquid interfaces at the same time. UVP flowmeter, therefore, can be extended from single-phase flows to multi-phase flows. Using both of echo intensity and Doppler shift frequency, instantaneous interface positions and velocity distribution are measured, so volume flow rates of each sampling time can be obtained. As a result of comparison with the results of optical visualization, it was revealed that the difference of speed of sound in each phase and refraction of ultrasound on interfaces contribute largely to the calculation of measurement positions and velocities. This paper also proposed the correction method for these and validity of UVP multi-phase flowmeter were mentioned.

**Keywords:** Visualization, Ultrasound, Flow rate, UVP, Echo intensity

### 1. 序 論

エネルギーへの需要が急速に高まっている現代において、それらを持続的に各地へ運搬するパイプラインの果たす役割もまた大きくなっている。ところが、燃料を運搬するパイプラインに関しては、その流量計測技術が発展途上の段階にある。パイプライン内部には、物性の異なるいくつかの流体が混在しているにもかかわらず、現行の流量計測機器の多くは単相流を想定したものが多く、混相流に対応したものの例は少ない。また、混相流量計についても、現在はあらかじめ相分離を行った後に各流量を計測したり、攪拌を行った分散流としての流量を計測したりするものが多く用いられている。パイプラインの多くは、耐圧性や耐食性を考慮し、金属で作られたものが多く、内部流動の様子を光学的に可視化することも困難である。そこで、本研究グループでは、超音波流速分布計<sup>(1)</sup>

(UVP: Ultrasonic Velocity Profiler) を用いた流量計測手法の開発を目指している。UVP を用いるメリットは、超音波が伝搬する物質であれば不透明であっても内部流速の計測が可能であることや、非侵襲での計測のため圧力損失が生じないことが挙げられる。さらに、その時間分解能の高さから瞬時の流量モニタリングが可能のため、非定常な流れに対しても適用することができる。

反射強度を用いることで界面検出を行い、ドップラーシフト周波数を基に流速を算出した。これらの手法によって得られた界面高さや速度分布の妥当性評価を目的として実験を行った。そのため、本実験の円管はアクリル製の透明なものを用い、光学的可視化実験を同時に行えるようにした。最終的に各時刻で計測された界面高さや流速分布を用いることで体積流量を算出した。これについては、計測された瞬時流量の積分値と、計測前に流入させた液体の実際の体積とを比較することで妥当性検証を行った。

本稿では、これらの界面検出手法や流量計算に至るまでの過程について述べ、UVP による混相流量計測技術の可能性を提案する。

### 2. 実験装置及び実験条件

Fig. 1 に実験装置の概略図を示す。実験流路として、内径 55 mm、肉厚 3 mm、長さ 1000 mm の透明アクリル円管を用いた。作動流体には空気、シリコンオイル、水を用い、シリコンオイルと水にはそれぞれトレーサー粒子としてフロービーズ (CL-2507, 住友精化, 直径 78–180  $\mu\text{m}$ , 密度 920  $\text{kg}/\text{m}^3$ ), ダイヤイオン (HP20SS, 三菱化学, 直径 60–200  $\mu\text{m}$ , 密度 1020  $\text{kg}/\text{m}^3$ ) を懸濁させた。円管の両端は、モータースライダーによって駆動されるベルトに取り付けた。このモータースライダーが正弦波振動を行うことにより円管が傾斜し、内部の流体が駆動される。なお、振動周期と振幅は PC を介して自由に設定することが出来る。円管の真下に取り付けられた基本周

波数 4 MHz の超音波トランスデューサーを用いることで UVP 計測を行った。本実験での UVP の時間分解能は 17 ms であった。今回用いた系では管軸方向 ( $x$  方向) の流れが支配的になると考えられ、その流速成分を計測するために超音波トランスデューサーを  $y$  軸に対して  $15^\circ$  傾斜させて設置した。超音波の減衰を抑えるため、UVP による計測線付近を水で満たした水層によって覆い、その温度を  $25^\circ$  に保った。長時間静置した後に実験を行ったため、円管内部の流体も同様に  $25^\circ$  に保たれていると仮定した。このとき、各物質中の音速はシリコンオイル、水、アクリル中で、それぞれ 979 m/s, 1497 m/s, 2730 m/s を用いた。UVP 計測によって得られた結果の妥当性評価のために、出力 2 W のレーザーシートを光源とし、ハイスピードビデオカメラ (以下 HSVC) による光学的可視化実験を行った。

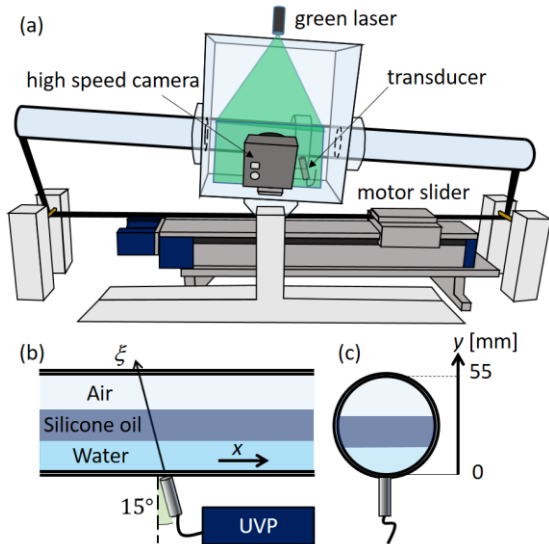


Fig. 1 Schematic image of experimental setup; (a) overall view, (b) side view and (c) cross section

### 3. 実験結果及び考察

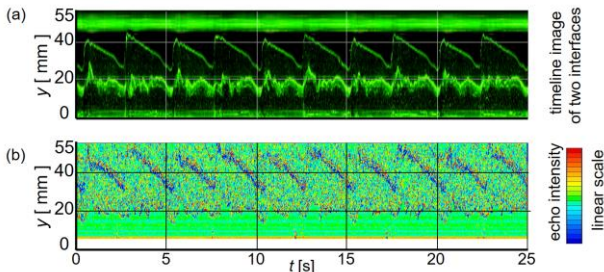


Fig. 2 Samples of two interface positions; (a) optical visualization and (b) echo intensity distribution obtained from UVP

Fig. 2(a)に HSVC によって得られた時間展開画像を示す。この画像は、超音波計測線付近の縦 1 ピクセルについて時間展開を行うことで、空気-油および油-水の 2 つ

の界面の高さを時空間分布で示している。図の縦軸は円管底面からの高さ  $y$ 、横軸は計測時間  $t$  を示している。このときのモータースライダの振動条件は振幅 10 mm, 振動周期 5 s であったため、Fig. 2 は 5 周期分の時空間分布を示している。この条件では、各流体の体積割合を等しくした。図において  $y = 20$  付近で小刻みに揺らいでいるのが油-水界面であり、 $y = 30$  から 40 前後で見られる大きな変動が空気-油界面である。Fig. 2(b)に UVP によって得られたエコー強度の時空間分布を示す。Fig. 2(a)と比較すると、ここからも小刻みに揺らいでいる油-水界面と大きく揺らぐ空気-油界面を捉えられている様子が見える。

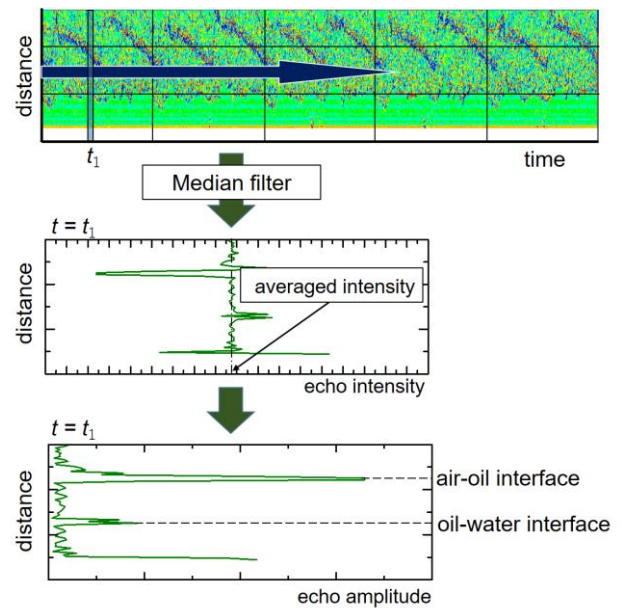


Fig. 3 Scheme of interfaces detection

このエコー強度の時空間分布に対して、Fig. 3 に示した処理を行い、各界面の高さを算出した。まず初めに、ピクセルノイズの除去を目的として、エコー分布全体に対してメディアンフィルタ処理を行った。次に、各時刻でのエコー強度に注目すると、ある値を中心にエコー強度が振動している様子がわかる。これを取り扱いやすくするために、各ピクセルについて、そのポイントのエコー強度から、全体のエコー強度の平均値を引いた値の絶対値で表されるエコー振幅を算出した。この結果、Fig. 3 の一番下に示すようにいくつかのピークが現れた。一番下のピークはトランスデューサー近傍の円管壁面によるエコーを示し、中央と上のピークがそれぞれ油-水界面と、空気-油界面を表しているものと考えられる。UVP によって検出されるエコー強度は、UVP-Duo 独自の値を用いていて、かつ、超音波の減衰を考慮してトランスデューサーから遠ざかる方向に大きなゲインをかけたため、出力される値自体に大きな意味はない。そのため今回は、各時刻のエコー振幅に関して、界面に対応する 2 つのピークを検出するために、単純に周囲との比較を行う用途でこの値を

用いた。この方法で特定した二つの界面は、トランスデューサーからの距離で示されている。円管内径を考慮したうえで、トランスデューサー設置角度である  $15^\circ$  の余弦を乗ずることで底面からの高さ  $y$  に変換した。この結果を HSVC によって得られた時間展開画像上に重ねたものを Fig. 4 に示す。エコーから特定した界面は黄色の線で示されている。この画像からも、エコー強度を用いることで大まかな界面の波形を検出できることがわかる。ところが、空気-油界面で顕著にみられるように、エコーによって得られた界面は、画像で見られる界面よりも高い位置に検出されている。これを較正するために、以下に示す Fig. 5 のように界面での超音波の屈折と各相での音速差に注目した。界面での屈折は式(1)で示されるように、各相での音速  $C$  と入射角  $\theta$  がわかれば屈折角を算出することができる。一方で、トランスデューサーからの距離  $\xi$  は、式(2)で示されるように、超音波発射から受信までの時間  $\tau$  を基に算出されている。今回の計測結果は、すべて水中での音速を用いて得られた結果であるため、アクリルやシリコンオイルに関しては、それぞれ適切な音速の値を用いて音響幾何較正を行った。

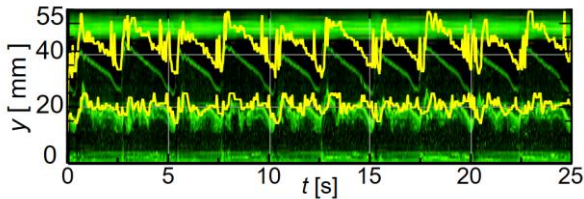


Fig. 4 Interface positions on the timeline image detected from UVP

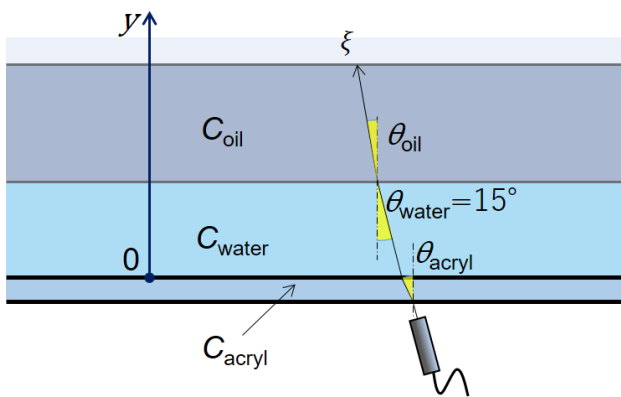


Fig. 5 Schematic image of model for correcting interface positions

$$\frac{C_1}{C_2} = \frac{\sin \theta_1}{\sin \theta_2} \quad (1)$$

$$\xi = \frac{C\tau}{2} \quad (2)$$

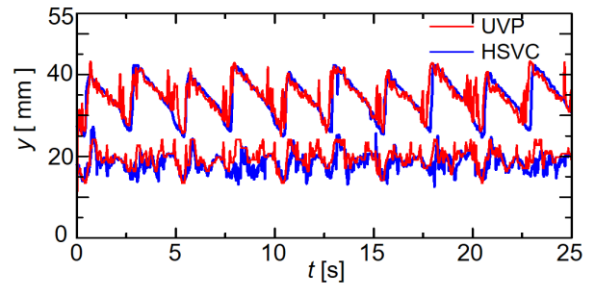


Fig. 6 Comparison of detected interfaces between echo intensity and optical visualization

以上の手法を用いて補正を行った各界面の高さを、HSVC による画像から検出した界面高さと比較したものを Fig. 6 に示す。音速差と界面での屈折についての補正を行ったことで、Fig. 4 の場合と比べて、空気-油界面の高さもよく一致していることがわかる。実際に空気-油界面高さの平均値を用いて計算してみると、補正をしなかった場合には、画像から得られた界面に比べて +22.6% の誤差を有していたにもかかわらず、補正後はその誤差が +1.89% に減少した。図をよく見ると、エコーによって検出した界面に関しては、急峻に高くなっている個所がいくつか見受けられ、エラーが含まれていることがわかる。これに関しては、より高精度の界面検出手法や較正方法を考案する必要があるが、現段階でも十分に界面の波形を捉え、較正を行うことで、これまで多く行われてきた気液界面検出<sup>(2-4)</sup>だけでなく、水と油の液液界面も同時に検出できることが確認された。

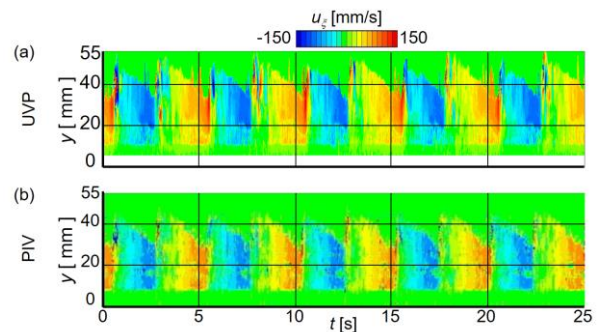


Fig. 7 Comparison of spatio-temporal velocity distributions obtained by (a) UVP and (b) PIV

次に、流速分布の妥当性について述べる。Fig. 7(a)に UVP で得られた計測線方向成分の時空間流速分布を示す。また、同図の(b)は、HSVC で撮影された画像を用いて粒子画像流速測定法<sup>(5)</sup> (PIV: Particle Image Velocimetry) を行い、UVP の計測線付近で得られた速度ベクトルの計

測線方向成分のみを時間展開した時空間流速分布である。両者を比較すると、流速分布の傾向がよく一致していることがわかる。ところが、UVP で得られた流速分布では、シリコンオイル相と思われる位置での流速が PIV による結果と比べて色濃く表示されているのがわかる。UVP で得られる流速は、トレーサーによって反射された際、超音波の周波数がドップラー効果によって  $f_D$  だけ変化した場合、式(3)を用いて算出される。そのため、ここでも各相での音速による較正が必要となる。また、既述の通り、界面での超音波の屈折が生じると考えられるため計測線の傾きも考慮する必要がある。

$$u_x = \frac{C f_D}{2 f_0} \quad (3)$$

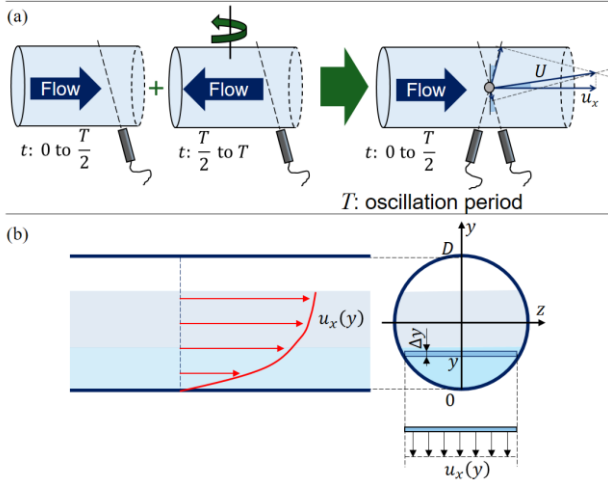


Fig. 8 Schematic image of model for calculating instantaneous volume flow rates

以下では、これらの影響を考慮し、Fig. 8 に示す仮定のもと、体積流量を算出した。この解析では、Fig. 8(a) に示すように円管の振動が左右対称であるため、作動流体の流動も再現性が取れているとの仮定を用いた。これにより、図に示したように 2 本のトランスデューサーを用いて計測したとみなすことができ、計測線上の流速ベクトルを算出できる。したがって、流速の  $x$  成分のみを抽出した。流速分布は Fig. 8(b) に示すように、高さ  $y$  のみの関数であるとして、各高さでは流速は  $z$  に依らず一様であると仮定した。各時刻での空気-油界面の高さを  $y = y_{ao}$ 、油-水界面の高さを  $y = y_{ow}$  とすると、油と水それぞれの瞬時の体積流量は次の式で与えられる。流速に乗ずる微小断面面積としては長方形を仮定している。これらを離散化して得られたのが Fig. 9 に示す瞬時体積流量分布である。この流量計測は、モータースライダーの振動条件を振幅 70 mm、振動周期 20s とし、作動流体をシリコンオイル 300 mL、水 400 mL に減らすことで、半周期ごとにすべての円管内の液体がトランスデューサーの上を通過するように設定した。

$$Q_o(t) = \int_{y_{ow}(t)}^{y_{ao}(t)} u_x(y) \cdot 2\sqrt{y(D-y)} \cdot dy, \quad (4)$$

$$Q_w(t) = \int_0^{y_{ow}(t)} u_x(y) \cdot 2\sqrt{y(D-y)} \cdot dy. \quad (5)$$

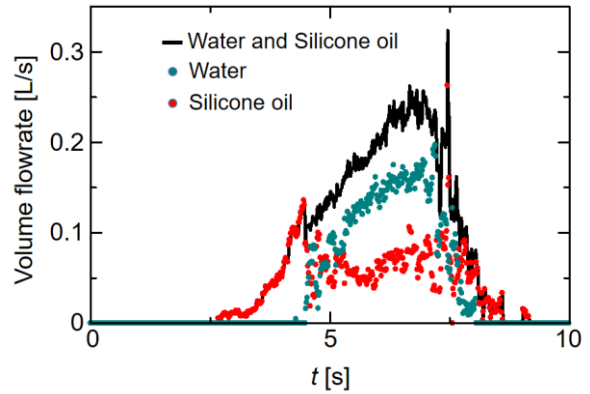


Fig. 9 Instantaneous volume flow rate

$$V(t) = \int_0^t Q(t) dt. \quad (6)$$

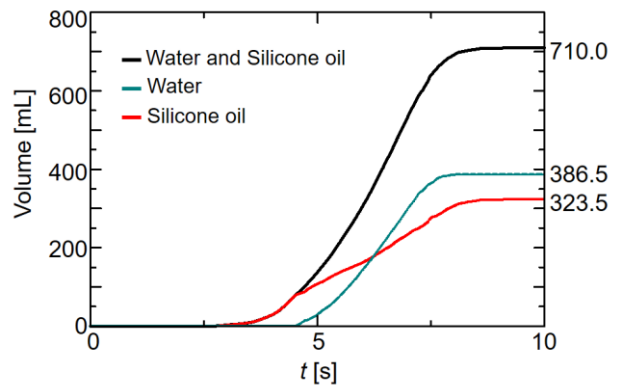


Fig. 10 Measured cumulative flow volume

この図から、最初に赤点で示されるシリコンオイルが流入し、後から緑点で示される、密度の大きい水が続く様子が見られる。妥当性評価を行うために、式(6)を用いることである時刻  $t$  までにトランスデューサー上を通過した体積を算出した。これによって算出された体積を時間ごとに示したのが Fig. 10 である。最終的に半周期である時刻 10 s のときの体積に注目すると、シリコンオイルの体積が 323.5 mL、水の体積が 386.5 mL となった。流量計測が完全に正確に行われていれば、これらの値は、円管内に流入させた体積であり、それぞれ 300 mL、400 mL になるはずである。Fig. 10 に示された計測結果ではシリコンオイルで 8%、水で 3%、さらに液体全体では 2% の誤差を有していた。しかしながら、上記で示したような単純なモデルを用いた結果でさえも、最大の体積誤差が 10% 未満であったことは、評価できる点であると考えられる。

#### 4. 結論

本研究では、空気、シリコンオイル、水の気・液・液層状流に対して UVP 計測を行い、得られたエコー強度と流速分布を用いて各相の体積流量を測定した。これらの値の妥当性評価を目的として実験を行った。

超音波エコー強度を用いることで、空気-油界面と油-水界面を同時に検出することができる。さらに、界面での超音波の屈折と各相での音速の違いを反映し、音響幾何較正を行うことで、可視化実験の結果とも良い一致を示した。また、流速分布に関しても、PIV による結果との比較からシリコンオイル相では音速の違いや計測線の傾き等によって、UVP で得られた流速が過大評価されていた。これらの計測によって得られた界面の高さと、各相で較正を行った流速分布を用いて、瞬時の瞬時体積流量を算出することができた。その瞬時流量の時間積分値で与えられる体積を、計測前に流入させた体積と比較すると、その誤差は最大でも 10%未満であった。今後は、流速分布モデリングをより忠実にを行い、トランスデューサーの複数本計測を組み合わせることにより、高確度な混相流量計測手法確立をめざす。

#### 参考文献

- 1) Y. Takeda, *Ultrasonic Doppler Velocity Profiler for Fluid Flow*, Springer, 2012.
- 2) T.T. Nguyen et al., *Int. J. Heat Mass Transfer*, 99, 159-169, 2016.
- 3) H.J. Park et al., *Meas. Sci. Technol.*, 26, 125301, 2015.
- 4) Y. Murai et al., *Flow Meas. Instrum.*, 21, 356-66, 2010.
- 5) 可視化情報学会編, PIV ハンドブック, 第 1 版, 森北出版株式会社, 68-71, 2002.

## UVP を用いた乱泥流の構造解析手法の確立

人見 純平<sup>○</sup>(北大), 野村 瞬(JAMSTEC), De Cesare Giovanni(EPFL), 武田 靖(ETHZ),  
阪口 秀(JAMSTEC), 朴 炫珍(北大), 田坂 裕司(北大), 村井 祐一(北大)

### Extensive use of UVP data from experimental turbidity currents to evaluate their flow structure

Jumpei HITOMI, Shun NOMURA, Giovanni De CESARE, Yasushi TAKEDA,  
Hide SAKAGUCHI, Hyun Jin PARK, Yuji TASAKA, Yuichi MURAI

#### ABSTRACT

Turbidity currents are gravity currents driven by density contrast between ambient fluid and sediment-laden fluid. Excellent measuring instruments and data analysis technique are required to quantitatively evaluate the inner flow structure of turbidity currents. Their motion strongly affects particle sedimentation or transportation with tremendous effect in oceans, lakes, and rivers. In this study, turbidity currents were generated by opening the lock gate to release a sediment-laden mixture to an experimental flume. Quartz powder and opalin clay whose order of mean diameters are 10  $\mu\text{m}$  were used as test particles in sediment-laden fluids. Simultaneous measurement using two ultrasonic velocity profilers (UVP) and Taylor-frozen hypothesis made it possible to obtain 2D instantaneous velocity distributions in high spatial and temporal resolutions. Using echo obtained from UVP, besides, spatio-temporal concentration distribution could be obtained. The features of the inner flow structures in turbidity currents could be discussed due to those evaluation methods.

**Keywords:** UVP, Turbidity current, Concentration, Taylor frozen hypothesis

#### 1. 序 論

乱泥流は、微細粒子を有する流体と周囲流体との密度差によって駆動される密度流である<sup>(1,2)</sup>。海底や湖、河川における粒子の堆積や運搬作用は乱泥流と関わりが強く、その内部の流れ構造を定量的に評価する手法が求められている。自然界において生じる乱泥流は、大規模かつ発生時期を予測することが難しく、直接の観測が困難である。そのため、実験結果をもとに実現象を推察することが有効である。本研究では、水槽内において粒子懸濁液と水を隔てる仕切りを開放することで単層または二層の乱泥流を発生させた<sup>(3)</sup>。二層での実験を行った理由としては、各界面での相互作用が乱泥流に及ぼす影響が非常に大きいと考え、より明確な運動性の変化をとらえることで、内部構造の解明に大きく貢献すると期待したためである。懸濁液中の固体粒子として中央粒径 10  $\mu\text{m}$  オーダーの quartz と opalin の 2 種類を用いた。粒子密度が高い部分では、懸濁液は不透明流体となるため、乱泥流内部の流速分布取得には超音波流速分布計<sup>(4)</sup> (UVP: Ultrasonic Velocity Profiler) を用いた。UVP は、超音波が伝搬する

物質中であれば流速分布の取得が可能であることに加え、超音波の反射波であるエコーを用いることで、界面検出や濃度推定への応用ができるというメリットを有する<sup>(5)</sup>。今回は 2 台の UVP を用いた同期計測を行い、テイラーの凍結仮説を用いることで、高分解能で時空間流速分布の把握できることが確認できた。併せて、エコー分布から粒子密度の推定を試みた。本稿では、これら流れ構造解析手法の確立、及びそれらを用いた乱泥流の運動性の評価を目的として実験及び考察を行った。

#### 2. 実験装置及び実験条件

Fig. 1 に実験装置の概要図を示す。試験流路として、全長 4548 mm、深さ 210 mm、奥行き 143 mm、上部は自由界面である矩形容器を用いた。この容器を 1.38°傾斜させ、下端から 2300 mm の位置にゲート A を設置した。初期条件として、ゲート A より上流側に粒子懸濁液、下流側を水で満たした。懸濁粒子は quartz (Quartz K13, Carlo Bernasconi AG, 中央粒径 12.2 $\mu\text{m}$ , 密度 2650 kg/m<sup>3</sup>) と opalin (Opalit, HANS MEYER AG, 中央粒径 19.0

μm, 密度 2740 kg/m<sup>3</sup>) を使用した. 異なる 2 つの密度を有する流体を用いて二層の乱泥流を発生させる実験では, 上流側を長さ方向に等分する位置にゲート B を追加で設け, 高密度 ρ<sub>1</sub> のものを上流側, 低密度 ρ<sub>2</sub> のものを下流側に配置した. 上流側のゲート B を開放し, 2 種類の懸濁液同士で密度流を発生させ, 高密度側の head が到達するタイミングでゲート A を開放した. Table 1 に実験を行った粒子の種類と密度の条件を示す. この表での Q, O はそれぞれ懸濁粒子として quartz, opalin を用いたことを表している.

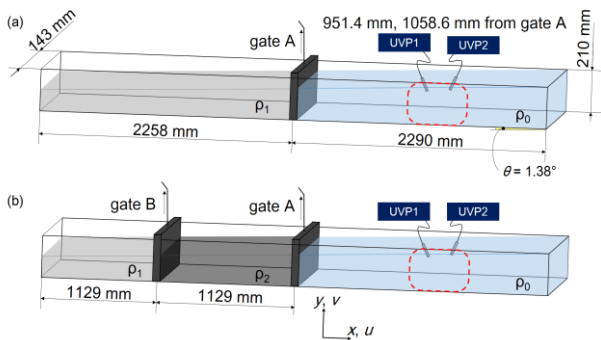


Fig. 1 Experimental setup; (a) for single-layer flows and (b) for double-layer flows

Table 1 Experimental conditions

case	number of layers	ρ <sub>1</sub> [kg/m <sup>3</sup> ]	ρ <sub>2</sub> [kg/m <sup>3</sup> ]
1	one		Q 1016
2	one		Q 1032
3	two	Q 1032	Q 1016
4	two	Q 1032	Q 1016
5	two	Q 1032	O 1016
6	two	O 1032	Q 1016
7	two	O 1032	Q 1016

基本周波数 4 MHz の超音波トランスデューサー (以下 TDX) をゲート A からそれぞれ 951.4 mm と 1058.6 mm, 底面から 130 mm の高さに 25° 傾斜させて配置することで UVP (UVP-DUO, Met-Flow) による計測を行った. 2 つの TDX による超音波計測線がゲート A から 1005 mm, 底面から 15 mm の位置で交わるよう設置した. 本実験では UVP 計測の時間分解能  $t_{UVP}$  を 50 ms, 空間分解能を 0.74 mm に設定した. すべての実験において水温は 8.0°C であった. UVP 計測位置付近である赤の破線で示された領域について, フレームレート 25 fps のビデオカメラによる撮影を行った.

### 3. 実験結果及び考察

#### 3-1. 先端速度の計測

各実験で得られた画像から front velocity (以下  $U_f$ ) の算出を試みた. あらかじめ head 部分のテンプレート画像を作成し, 各画像に関して最も輝度分布の直接相互相関

係数が大きい座標を探索するテンプレートマッチング手法を用いた. テンプレート画像は, 実験毎に縦 451 px, 横 451 px の大きさのものを作成した. テンプレート画像から 0.4 秒ずつ経過した画像に対して, 相関値が最も大きい部分の中心座標をプロットしたのが Fig. 2 である. 横軸はテンプレート画像を作成した時刻  $t_0$  から対象とする画像が撮影された時刻  $t$  までの時間  $T$ ; 縦軸は中心座標の移動距離  $X$  を示している. この分布より,  $X$  と  $T$  には概ね比例関係が成立している. これは, 今回の実験条件では, 粒子懸濁液と周囲流体である水の初期体積がほとんど同じであるため, 乱泥流を駆動する大きな要因の 1 つである密度差が十分に確保されることで, 流れが減衰することなく進行しているためである. このことから  $U_f$  は一定であり, 以下の(1)式により定義できる.

$$U_f = \frac{1}{N} \sum_{i=1}^N \frac{X(i)}{T(i)} \quad (1)$$

Fig. 3 は  $U_f$  を縦軸, 粒子懸濁液の平均密度  $\rho'$  を横軸としてまとめている. エラーバーは標準偏差である. 二層流に関しては上流側の初期体積  $V_1$  と下流側の初期体積  $V_2$  の違いを考慮し, (2)式を用いて  $\rho'$  を算出した.

$$\rho' = \frac{1}{V_1 + V_2} (V_1 \rho_1 + V_2 \rho_2) \quad (2)$$

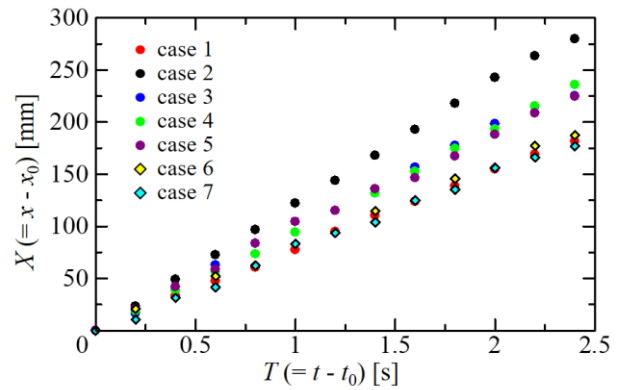


Fig. 2 Temporal distributions of moving head positions under each experimental condition

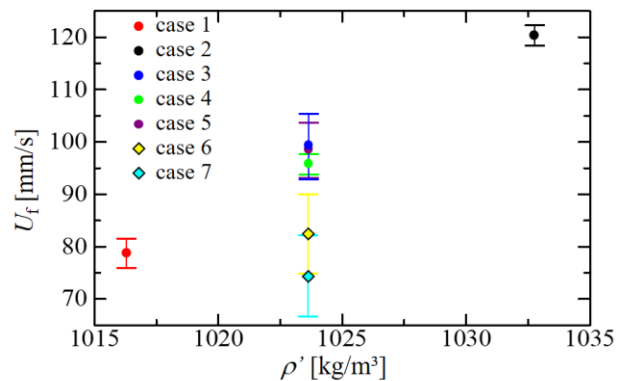


Fig. 3 Relationship between front velocity and

averaged density

Fig. 3 より, 下層に opalin を用いて行った case 6 及び case 7 の実験結果を除いては, 丸いシンボルで表されるように平均密度が大きくなるに従い  $U_f$  の値も比例して大きくなることを確認できる. このことから  $U_f$  を決定づける大きな要因は粒子懸濁液の密度と, 下層を流れる粒子の種類であるということが確認できる.

3-2. 流れ構造の解析

以下の議論では, 乱泥流の内部構造を超音波計測によって評価する手法論に焦点を当てるため, 基本的なケースである case 1 に関する計測結果について述べる. 2 台の UVP から得られた流速分布とテイラーの凍結仮説を用いることで, 超音波計測線上の二次元流速成分の算出を試みた. 上記の先端速度の議論より, 乱泥流全体の流れ構造は,  $U_f$  を一定に保ったまま移流すると仮定できる. ここで TDX は  $25^\circ$  傾斜して配置されているため, 計測線が交わる高さ以外では 2 つの UVP によって得られた流速分布には時間的な差異が生じる. この影響を考慮するため, 以下の Fig. 4 に示すように,  $U_f$  により計測時間差の較正を行った. 例えば TDX 1 によって計測されるのは, 超音波計測線の交点 P を基準に考えると, 上流側ではマイナスの時刻, 下流側ではプラスの時刻となる. その時間差  $\Delta t$  を,  $U_f$  を用いることで以下の(3)式によって較正した. 計測点と超音波の交点 P の距離  $\eta$  は TDX からの距離  $r$  の関数で幾何学的に算出することができる.

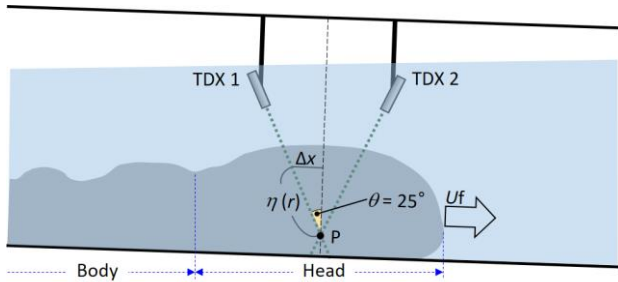


Fig. 4 Schematic image of the method of time correction by front velocity

$$|\Delta t| = \frac{|\Delta x|}{U_f} = \frac{|\eta(r)| \sin \theta}{U_f} \quad (3)$$

2 台の UVP から得られた流速をそれぞれ  $u_1, u_2$  とすると, (4)(5)式により計測線上での  $u$  成分と  $v$  成分の計算が可能である. この手法によって得られた  $u, v$  成分の時空間分布と, 可視化画像から得られた 2 つの超音波計測線の交点の位置での時間展開画像を Fig. 5 に示す. 流れの方向に合わせ時間軸を反転させており, 上の横軸は 50 秒間の計測において  $U_f$  が一定であると仮定した場合の換算距離を示している. すなわち, この換算距離は  $U_f \cdot (50 \cdot t)$  で算出している. 画像において, ゲートの開放後 10 から 25 秒付近で上に凸となっているのが乱泥流の head と呼

ばれる部分であり, それに続く比較的定常な分布を示すのが body である. これらの時空間分布から, 乱泥流後方から連続的に供給される流量に対して, 先端では周囲流体である水の存在によって進行方向への流れが抑制されるため, 一部が上方へ舞い上がり head を形成する様子が確認できる. また body の上部では, わずかながら正の  $v$  の分布が見られる. この領域では, 逆方向に移流する水との剪断によって, 比較的密度の小さい流体が引き剥がされている様子をとらえているものと考えられる.

$$u(y, t) = \frac{u_1(y, t) - u_2(y, t)}{2 \sin \theta} \quad (4)$$

$$v(y, t) = -\frac{u_1(y, t) + u_2(y, t)}{2 \cos \theta} \quad (5)$$

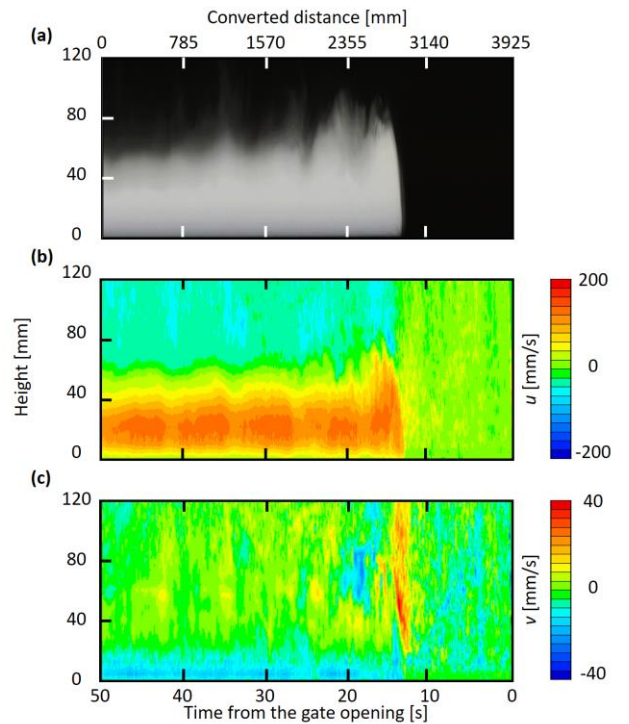


Fig. 5 Spatio-temporal distribution of turbidity current; (a) timeline image at the cross point of two ultrasonic waves, (b) and (c) show  $u$  and  $v$  component of velocity obtained by UVP respectively

上記のように得られた  $u$  成分と  $v$  成分を空間微分することで得られた渦度分布を Fig. 6 に示す. 空間微分を行う際の  $\Delta x$  に関して,  $U_f = 78.5 \text{ mm/s}$  であるためテイラーの凍結仮説より  $\Delta x = U_f \cdot t_{UVP} = 3.93 \text{ mm}$  を用いた. また  $\Delta y$  に関しては, 超音波パルスの幅が  $0.74 \text{ mm}$  であったため, 6 チャンネルの平均値を用いることで  $\Delta y = 0.74 \cos(25^\circ) \cdot 6 = 4.02 \text{ mm}$  となり,  $\Delta x$  に近い値での評価を行った. 渦度分布から head の上部では, 水との相互作用により渦度

の値が最も大きく示されている。この分布からも巻き上げられた流体の一部は渦を巻きながら下流へと移流する様子がうかがえる。また、body では流速の  $u$  成分が最大となる高さ 20 mm 周辺で、正負の対をなす渦度が表れており鉛直方向の流れ構造の変化の様子が伺える。

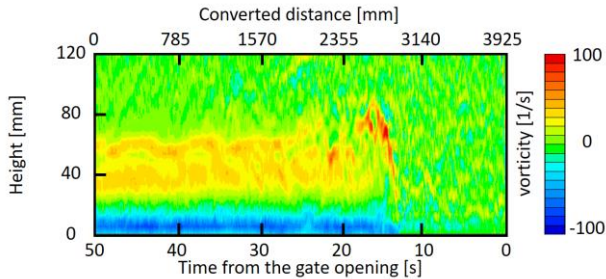


Fig. 6 Vorticity distribution calculated by using Taylor frozen hypothesis

次に超音波の反射強度であるエコーを用いた濃度分布の推定を試みた。quartzは中央粒径  $d$ が 12.2  $\mu\text{m}$  であり、実験条件である 8 $^{\circ}\text{C}$  の水中での波長  $\lambda$  を用いて計算される散乱に関する無次元値  $\pi d/\lambda = 0.107$  であり、1.0 よりも十分小さい値であるため、レイリー散乱を仮定することができる。粒子径が均一であり、多数の粒子がランダムに超音波の検査体積内に含まれていると仮定すると、検査体積内に存在する粒子質量  $M[\text{kg}/\text{m}^3]$  は、超音波エコー強度の二乗平均である  $\langle V^2 \rangle$  との関係は以下の (6) 式で示されている<sup>(6)</sup>。

$$M = \langle V^2 \rangle \left( \frac{\psi r}{K_s K_t} \right)^2 e^{4\alpha r} \quad (6)$$

ここで、 $K_t$  と  $K_s$  はそれぞれ懸濁粒子の散乱特性を示す関数、超音波計測装置特有の定数を示している。 $\Psi$  は超音波による後方散乱の信号の様子を表している。また、 $\alpha$  は水中と粒子懸濁液中での超音波減衰率の和である。この式において  $M$ 、 $\langle V^2 \rangle$ 、 $\alpha$  が TDX からの距離  $r$  の関数であるため、Lee と Hanes は両辺の自然対数を取り、再構成することで以下の関係式(7)を得ている<sup>(7)</sup>。

$$M_n = \frac{r^2 \langle V^2 \rangle e^{4\alpha_w r}}{\frac{1}{M_1} r_1^2 \langle V^2 \rangle_1 e^{4\alpha_w r_1} - 4\xi \int_{r_1}^r \langle V^2 \rangle r^2 e^{4\alpha_w r} dr} \quad (7)$$

ここで  $I$  は各値の初期値であり、最も TDX に近い位置で計測される値であることを示す添え字である。UVP-Duo によって得られるエコーは、1) 数十回の超音波パルスによって得られた値の平均値であり、2) ゲインによって拡張された値が得られるため取り扱いが困難である。後者に関しては、今回は Pedocchi と Garcia によって示された Time Variable Gain 値を用いてその影響を取り除くことができる<sup>(8)</sup>。前者の問題に関しては、 $\langle V^2 \rangle$  に関して対象とする時空間での計測点の周囲  $5 \times 5$  計 25 点でのエコー情報を用いて二乗平均を計算し、再度統計処理を行うこ

とによって影響緩和を試みた。本解析で二乗平均を算出する際に用いた式を(8)式に示す。(8)式において平均値  $\bar{V}$  は、TDX からの各距離でのエコー強度の平均値を用いた。

$$\langle V^2 \rangle_{y,t} = \frac{1}{25} \sum_{i=-2}^2 \sum_{j=-2}^2 (V_{y+i,t+j} - \bar{V}_{y+i})^2 \quad (8)$$

上記の手法で得られた case1 の時空間密度分布をベクトル分布とともに Fig. 7 に示す。ここでベクトル分布に関しては、見やすさの観点から  $6 \times 6$  の計測データの平均値で示しており、実際にはこの 36 倍の時空間でのベクトルが得られている。Fig.7 から、全体的な密度分布の傾向として深度方向に密度が単調に増加していることが分かる。また、body での密度分布に比べて head の先端では、上部まで大きな値が分布している様子が特徴的である。水との界面での剪断力だけで高密度の流体が上部まで巻き上げられることは考えにくく、この head 先端付近で後方から供給される流体と、その前方に存在する水が相対的に押し合った結果として、このような密度分布が生じると考えられる。Fig. 7 に、乱泥流の body が通過している 30 から 50 秒の間で時間平均された密度と流速の  $u$ 、 $v$  成分、渦度の分布を示す。各計測値は、この範囲での絶対値が最大となる値で除すことで、-1 から 1 の範囲で分布する無次元量となっている。縦軸は水槽の深さ  $H = 210$  mm で無次元化された底面からの高さを示している。密度と  $u$  成分の比較より、密度が最大になる高さは流速分布が最大となる高さに比べ、低い位置に存在することが確認できる。また、密度分布では、無次元高さ 0.2 付近で第二のピークが存在している。これは、概ね  $v$  成分が正の分布を示す領域に一致しており、body のメインとなる流れから剪断によって引き剥がされたものによる影響ではないかと考えられる。これらの関係性は粒子の運搬もしくは堆積作用に大きく関係していることを示唆しており、今後はそれらに関して定量的な評価を行う予定である。

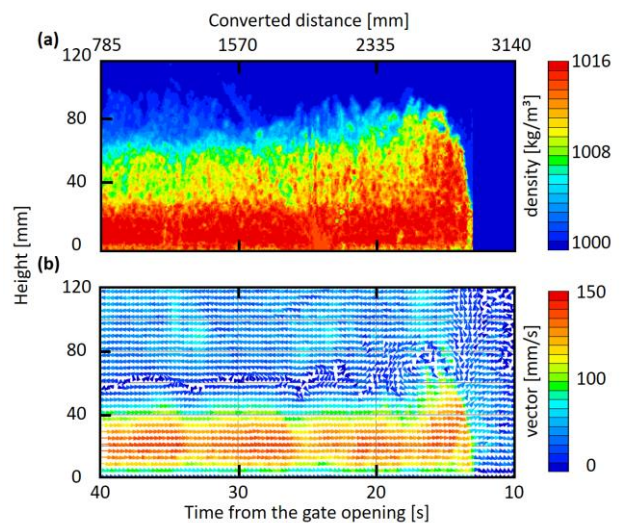


Fig. 7 (a) Spatio-temporal density distribution and (c) vector field

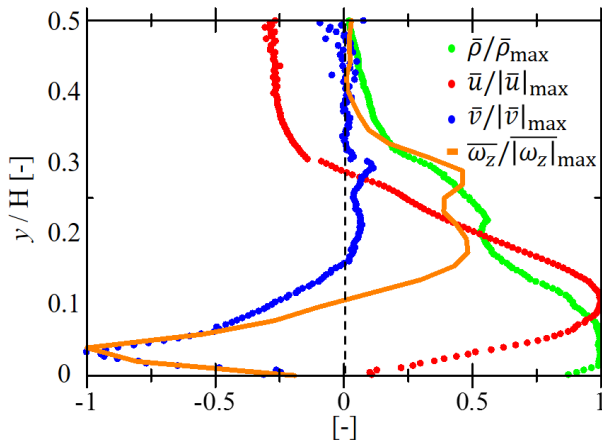


Fig. 8 Normalized values of density, horizontal and vertical components of velocity, and vorticity which are averaged by the time from 30 to 50 s

#### 4. 結論

本研究では、水槽内に設置したゲートを開放することで密度差によって駆動される乱泥流を発生させ、密度、層構造が乱泥流の先端速度に及ぼす影響を評価した。併せて、単層の典型的な乱泥流を例にとり、内部構造の定量的評価手法の開発および運動性の整理を行った。得られた主な結果3点を以下にまとめる。

1) テンプレートマッチング手法を用いることで、各時刻での head の位置を検出した。本実験では、粒子懸濁液の初期体積が十分に大きかったため、各実験条件での先端速度は等速であると仮定できることが分かった。単層または二層の場合にかかわらず、下部を流れる懸濁粒子の種類が等しい場合に関しては、その速度は平均濃度と比例関係にあることが分かった。すなわち、先端速度を決定する大きな要因は、密度と底部を流れる懸濁液の種類であると考えられる。

2) 2 台の UVP の同期計測を行い、先端速度を用いてプロファイルの時間差を較正することで、超音波計測線上での時空間流速分布の取得を行った。テイラーの凍結仮説を用いることで、渦度を算出した結果、head の先端部分では強い巻き上げを示す大きな値が観測された。また、body の外側では周囲流体である水との相互作用による剪断の様子が観察され、内部では流れ方向の流速成分  $u$  が最大となる高さの上下で正負対をなす渦度が分布する様子が観察された。

3) UVP によって得られるエコーを用いることで濃度分布の算出を行った。今回使用した quartz は中央粒径が  $12.2\mu\text{m}$  であったため、レイリー散乱の関係式を用いることで、超音波エコーと粒子密度の関係性を確認することができた。

今後の研究計画としては、今回得られた評価手法を用

いて更なる物理量を考察することで、乱泥流の内部構造の定量化や各実験条件で運動性の整理を目指す。また、エコーを用いた濃度分布の推定に関しては、より高分解能かつ普遍的な評価手法確立を目指して、新たな実験系での研究を行う予定である。

#### 参考文献

- 1) Altinaker, M. S. *et al.*: Flow structure in turbidity currents, *Journal of Hydraulic Research*, vol.34 (1996), pp. 713-718.
- 2) Simpson, J. E.: *In the Environment and the Laboratory*. Cambridge University Press, London, (1997).
- 3) Theiler, Q., Franca M. J.: Contained density currents with high volume of release, *Sedimentology*, vol.63 (2016) pp.1820-1842.
- 4) Takeda, Y.: *Ultrasonic Doppler velocity profiler for fluid flow*, Springer, (2012).
- 5) Murai, Y. *et al.*: Development of an ultrasonic void fraction profiler, *Measurement Science and Technology*, 20(11): 114003 (2009)
- 6) Thorne, P. D., Hanes, D. M.: A review of acoustic measurement of small-scale sediment processes, *Continental Shelf Research*, vol.22 (2002) pp. 603-632.
- 7) Lee, T. H., Hanes, D. M.: Direct inversion method to measure the concentration profile of suspended particles using backscattered sound, *Journal of Geophysical Research* 100 (C2) (1995) pp.2649-2657
- 8) Pedocchi, F., Garcia, M. H.: Acoustic measurement of suspended sediment concentration profiles in an oscillatory boundary layer, *Continental Shelf Research*, Vol.46, (2012) pp.87-95.

## 乱泥流内粒子群運動の超音波による定量計測

Quantitative ultrasonic measurement of particle assemblage dynamics in experimental turbidity currents

人見純平 (北大院), 野村瞬 (JAMSTEC), De Cesare Giovanni (EPFL), 武田靖 (ETHZ),

朴炫珍 (北大院), 田坂裕司 (北大院), 村井祐一 (北大院)

HITOMI Jumpei, NOMURA Shun, DE CESARE Giovanni, TAKEDA Yasushi, PARK Hyun Jin, TASAKA Yuji, MURAI Yuichi

Turbidity currents are observed under seas and rivers. They are driven by the density difference between particle-laden fluids and ambient fluids. The purpose of this study is to reveal the reason why turbidity currents can propagate long distance. In this study, a turbidity current was generated by the lock-exchange method in a rectangular container with about 4.5 m with length and 210 mm with height. Quartz particles which center diameter is  $13.5 \mu\text{m}$  and density is  $2650 \text{ kg/m}^3$  were used as sediment particles. To measure the velocity distributions, ultrasonic velocity profiler (UVP) was applied to this flow. Two-UVP measurement and Taylor's frozen hypothesis made it possible to obtain horizontal and vertical velocity components. In addition, a distribution of particle volume fraction could be obtained using echo information. From these results, "head" which is front parts of turbidity current has high particle volume fraction and shows a huge change of velocity  $v$  components. In the "body" which is subsequent parts of the current, velocity fluctuation components  $u'$  and  $v'$  were calculated. To reveal the turbulence behavior of the turbidity current was tried using these  $u'$ ,  $v'$  and Reynolds stress.

**Keywords:** Turbidity current, Ultrasonic measurement, Echo analysis, Solid-liquid two-phase flow

### 1. 序論

乱泥流[1, 2]は、微粒子を含む流体と周囲流体との密度差によって駆動される流れである。河川では 100 km, 海中では 1000 km 以上もの距離を伝搬した例も報告されている。しかしながら、このように長距離を伝搬する理由は未だ明確にされておらず、多くの注目を集めている。自然界において実際に生じる乱泥流は、大規模かつ発生時期の予測が難しく、直接観測が困難である。さらに、微粒子や乱流の相互作用によって数値計算の適用も難しい。そのため、我々の研究グループは、実験的に乱泥流を発生させ、計測結果をもとに実現現象を推察することが有効であると考えている。本研究では、水槽内において、粒子懸濁液と周囲流体としての水を隔てる仕切りを開放することで乱泥流を発生させた。懸濁液中の固体微粒子として中央粒径  $13.5 \mu\text{m}$  の quartz を用いた。粒子濃度が高い部分では、懸濁液は不透明流体となるため、超音波流速分布計 (UVP: Ultrasonic Velocity Profiler) [3]を用いることで、乱泥流内部の流速計測を行った。UVP は超音波が伝搬する物質中であれば流速分布の計測が可能であることに加え、超音波の反射強度であるエコーを用いることで、界面検出や濃度推定への応用ができるというメリットを有する。今回は二台の UVP を用いた同期計測を行うことで、流速二成分の時空間分布を得た。さらに、エコー情報を併用することで、粒子濃度分布の推定を試みた。本稿では、UVP によって得られた定量計測の結果を基に、乱泥流の長距離伝搬メカニズムの解明を目的として実験及び考察を行った。

### 2. 実験装置及び条件

Fig. 1 に実験装置の概要図を示す。試験流路として、全長 4548 mm, 深さ 210 mm, 奥行き 143 mm, 上部は自由界面である矩形容器を用いた。この容器を  $1.38^\circ$  傾斜させ、容器のおおよそ中央の位置にゲート A を設置した。初期条件として、ゲート A より上流側を粒子懸濁液、下流側を水で

満たした。懸濁粒子は体積割合 1.0% の quartz (Quartz K13, Carlo Bernasconi AG, 中央粒径  $13.5 \mu\text{m}$ , 密度  $2650 \text{ kg/m}^3$ ) を使用した。この流体の平均密度は  $1016 \text{ kg/m}^3$  であった。

基本周波数 4 MHz の超音波トランスデューサー (以下 TDX) をゲート A からそれぞれ 951.4 mm と 1058.6 mm, 底面から 130 mm の高さに  $25^\circ$  傾斜させて配置することで UVP (UVP-DUO, Met-Flow) による計測を行った。二つの TDX による超音波計測線が  $x = 1005 \text{ mm}$ ,  $y = 15 \text{ mm}$ ,  $z = 71.5 \text{ mm}$  の点 P で交わるよう設置した。本実験での UVP 計測の時間分解能  $\Delta t$  は 50 ms, 空間分解能は 0.74 mm に設定した。水温は  $8.0^\circ\text{C}$  であった。

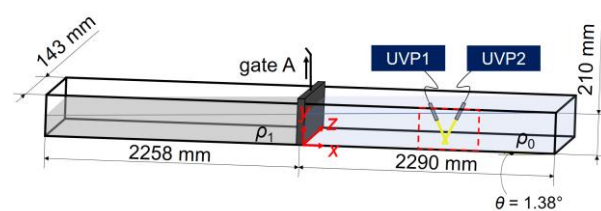


Fig. 1 Schematic diagram of experimental setup

### 3. 実験結果及び考察

超音波の反射強度であるエコー信号を解析することによって、粒子濃度分布の算出を試みた。今回用いた粒子は、超音波波長に対して十分の一以下の直径であるため、レイリー散乱が生じると考えられる。Pedocchi らは、UVP によって得られたエコー情報から、微粒子濃度分布を算出する方法を提案した[4]。UVP により出力されるエコーと、実測される音圧信号を関連付け、レイリー散乱をモデル化した式によって濃度を算出している。この手法を用いることで得られた乱泥流の粒子濃度分布を Fig. 2 に示す。縦軸は底面からの高さ  $y$ , 横軸はゲート A を開放してからの経過時間  $t$  を示している。そのため、視覚的な流れの方向と、示

されている結果が逆向きに見えることに注意が必要である。この分布から、乱泥流の下部と、head と呼ばれる先端部分に多くの粒子が含まれていることがわかる。

濃度分布に加えて、二つの TDX によって得られた計測線方向の流速成分を用いて、幾何学的なベクトル処理を行うことで、二成分  $u(y, t)$ ,  $v(y, t)$  の時空間分布を算出した。この際、実際に計測線が交わっているのは P 点のみであるが、テイラーの凍結仮説を用いることで、交差点以外でも線上の分布を得た。Fig. 3(a)(b) に上記の方法で得られた  $u$  と  $v$  の流速分布を示す。両者はカラーバーで示される速さの範囲が異なっており、 $u$  が卓越した流れであることが分かる。一方、 $v$  の分布に注目すると先端部分である head で強い巻き上げが生じている。その後方では、巻き上げられた比較的密度の高い流体が、再び乱泥流本体に吸収される動きが見られる。この動きによって、密度の高い流体が上から再侵入するため、更なる駆動力が供給されることが予想される。head が大きな巻き上げを示す部分、それらが再び本体に戻る部分、後続部分である body の三つの領域に関して、それぞれ時間平均した  $u$  と  $v$  の分布を Fig. 3(c) に示す。 $v$  の分布に関しては既述のとおりである。一方で、 $u$  の分布に関しては、どのケースでも  $y = 20$  mm 付近で最大値となることが分かる。さらに乱泥流の先端から後方に向かうにつれて、徐々にその最大値が大きくなり、分布形状が急峻になっていく様子が確認できる。このことから、乱泥流は密度差によって駆動され、先端部分が後方から押し進められることによって巻き上げが生じると考えられる。

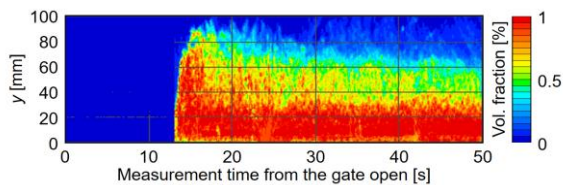


Fig. 2 Spatio-temporal distribution of particle volume fraction

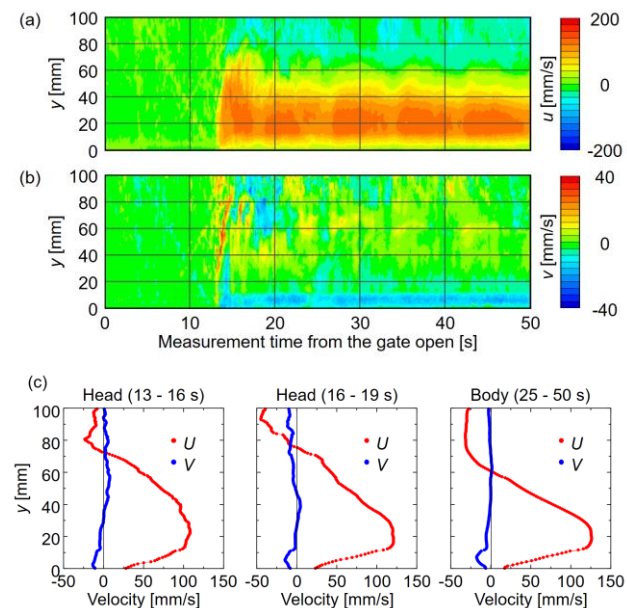


Fig. 3 Velocity distributions calculated from two UVP results: (a) and (b) show spatio-temporal distributions of  $U$  and  $V$  component respectively, and (c) indicates time-averaged distributions of turbidity current head and body.

既述の通り、乱泥流の head は先端のごく一部である。そのため、長距離伝搬の仕組みを明らかにするためには、body の構造に注目すべきであると考えた。Fig. 4 において、乱泥流の body である  $25 < t < 50$  s の流速分布の変動成分を示す。この際、二つの TDX によって計測される統計量は保存されるという仮説を用いた[5]。Fig. 4(a) は変動成分である  $u'$  及び  $v'$  の RMS 値の分布を示している。特に  $u'$  の分布に注目すると、粒子濃度が高い  $y = 30$  mm の高さ付近までは、流れの乱れが比較的小さいことを示している。さらに

Fig. 4(b) はレイノルズせん断応力  $-\overline{u'v'}$  の分布を示している。この分布において、 $y = 60$  mm 付近で大きな値が示されている。これは、乱泥流と周囲流体間の長周期の揺らぎによる影響であると考えられる。一方で、 $u$  が最大値となる上下の約  $10 < y < 40$  mm の範囲では、これらの値の  $y$  方向に対する勾配がおおよそ 0 になっていることが確認された。このことから、大きな流速成分  $u$  及び粒子濃度を有するこの領域では、 $x$  方向にスムーズに流れている様子が観察された。

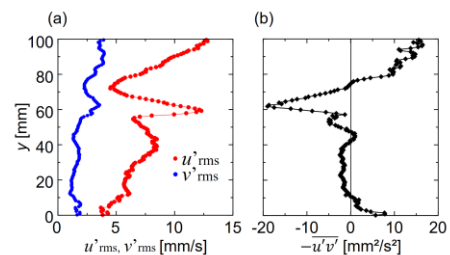


Fig. 4 (a) RMS value distributions of velocity fluctuation components from 25 to 50 s, and (b) Reynolds stress distribution.

#### 4. 結論

UVP によって得られた流速分布を基に、乱泥流の長距離伝搬の仕組みを解明することを目的として実験を行った。乱泥流の head および body に関して  $u$ ,  $v$  の流速分布の時間平均値を比較した。その結果、乱泥流の head では  $v$  の分布に特徴的な動きが見られた。ここから、比較的密度の高い流体が巻き上げられた後に、再び乱泥流内に巻き込まれることで、更なる駆動力として作用することが予想される。 $u$  の分布に注目すると、先端から後方に向かって、 $y = 20$  mm 付近での最大速度が増加しており、分布の形状は急峻になることが分かった。ここから、密度差によって駆動される body が head 部分を後方から押し進めることで、乱泥流が移流していく様子が観察された。さらに、body 部分の流速の変動成分に着目した結果、大きな流速  $u$  及び粒子濃度を有する高さでは、 $x$  方向にスムーズに流れている様子が確認された。今後は、渦スケールごとの解析を行い、乱泥流の長距離伝搬のメカニズムの詳細な解明に努める。

#### 参考文献

- [1] Keller, B. and Buckee, C., Sedimentology, Vol. 47, 62–94 (2000).
- [2] Baas, J. H. et al., Geophys. Res., Vol. 110, C11015 (2005).
- [3] Takeda Y., Springer, (2012).
- [4] Pedocchi, F. and García, M. H., Cont. Shelf. Res., Vol. 46, 87–95 (2012).
- [5] Taishi, T. et al., Exp. Fluids., Vol. 32, 188–196, (2002).